

UNCLASSIFIED

AD 405 481

DEFENSE DOCUMENTATION CENTER

FOR

SCIENTIFIC AND TECHNICAL INFORMATION

CAMERON STATION, ALEXANDRIA, VIRGINIA



UNCLASSIFIED

NOTICE: When government or other drawings, specifications or other data are used for any purpose other than in connection with a definitely related government procurement operation, the U. S. Government thereby incurs no responsibility, nor any obligation whatsoever; and the fact that the Government may have formulated, furnished, or in any way supplied the said drawings, specifications, or other data is not to be regarded by implication or otherwise as in any manner licensing the holder or any other person or corporation, or conveying any rights or permission to manufacture, use or sell any patented invention that may in any way be related thereto.

63-35

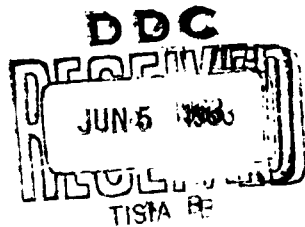
**First Quarterly Technical Progress Report
on Research and Development of an
Advanced Laboratory Liquid Metal
Regenerative Fuel Cell for the Period
1 March - 18 May 1963**

Allison EDR 3344

28 May 1963

**Air Force Aero-Propulsion Laboratory
Aeronautical Systems Division
Air Force Systems Command
Wright-Patterson Air Force Base, Ohio**


Project No. 8173; Task No. 817303



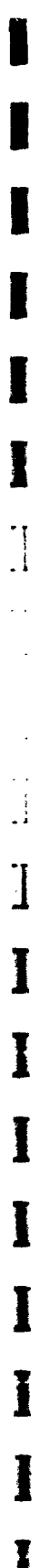
(Prepared under Contract No. AF33(657)-11032
by Allison Division, General Motors Corporation,
Indianapolis, Indiana

Authors: H. R. Karas and J. D. Mangus)

405 481



The work covered by this report was accomplished under Air Force Contract AF33(657)-11032, but this report is being published and distributed prior to Air Force review. The publication of this report, therefore, does not constitute approval by the Air Force of the findings or conclusions contained herein. It is published for the exchange and stimulation of ideas.



FOREWORD

This report was prepared by the Research Group of the Allison Division of General Motors Corporation on Air Force Contract AF33(657)-11032, Task No. 817303, Project No. 8173. The work was administered under the direction of the Air Force Aero-Propulsion Laboratory, Aeronautical Systems Division. Captain G. E. Starkey is the task supervisor for ASD.

The work began on 1 March 1963 on a basic contract to continue the work carried out under Contract AF33(657)-7847*, with the objective of operating a three-cell unit for 50 hours at a power density of 50 watts/ft² of electrode area. Storage characteristics will be determined and specifications for a finalized 5-kw space operational fuel cell will be prepared. This report is being written to fulfill part of the contract commitment.

The Liquid Metal Cell Project is managed by H. R. Karas, Senior Experimental Chemist, Applied Sciences. Mr. Karas is responsible for electrochemical investigations. J. D. Mangus, Senior Research Engineer, has the responsibility for mechanical design. Management direction at Allison includes Mr. T. F. Nagey, Director of Research, Dr. R. E. Henderson, Chief of Applied Sciences, and Dr. B. Agruss, Section Head, Applied Sciences.

*B. Agruss, H. R. Karas, and V. L. Decker, Design and Development of a Liquid Metal Fuel Cell, ASD-TDR-62-1045 (December 1962).

ABSTRACT

Work is under way to design a laboratory-type cell for operation with a matrix. Tests are in progress to determine matrix compatibility with electrolyte; optimization of mechanical and electrical properties of the matrix are progressing. A successful 96-hour seal was produced, although insulators were cracked and electrolyte seepage occurred. A preliminary check of electrochemical properties yielded encouraging results, predicting performance in the 50- to 100-watt/ft² range.

TABLE OF CONTENTS

<u>Section</u>	<u>Title</u>	<u>Page</u>
I	Introduction.	1
II	Materials.	5
	Ceramics for Matrices and Insulators	5
	Pure Ceramics (Chemical Properties).	6
	Pure Sintered Ceramics (Physical Properties)	7
	Porous Ceramics	9
	Metals	10
	Electrolyte.	10
III	Apparatus.	13
	Liquid Metal Cells.	13
	Sealing Test Cells	13
	Model III LMC	14
	Model IV LMC	15
	Matrix Design—Burst Test Samples	15
	Conductivity Cell	27
IV	Experimental Results	29
	NASA Matrix Program (Tasks 1, 2, and 3).	29
	General Motors Matrix Program	29
	Task 4—Seal Development.	29
	Task 5—Conductivity Study	30
	Task 6—Cell Tests.	30
	Air Force Program	30
	Task 8—Preliminary Materials Studies of Porous Ceramic Materials, Compressive Tests	30
	Task 9—Preliminary Design Studies, Matrix Burst Test.	39
	Task 10—Development of a Single Cell Seal.	46
	Task 11—Instrumentation	51
	Task 60—Theoretical Studies	51
	Performance Check.	55

<u>Section</u>	<u>Title</u>	<u>Page</u>
V	Technical Position	59
VI	Work Planned for Next Report Period	61
VII	References	63

Appendix. First Quarterly Technical Progress Report on
Development and Testing of Electrolyte Matrix
Combinations for Mercury-Potassium Fuel Cell
(12 December 1962—12 March 1963)

LIST OF ILLUSTRATIONS

<u>Figure</u>	<u>Title</u>	<u>Page</u>
1	Differential Density Cell	4
2	Sealing Test Cell	13
3	Detail of Cell Half—Model III	16
4	Detail of Electrolyte Feed Ring—Model III	17
5	Detail of Matrix Half—Models III and IV	18
6	Detail of Upper Cell Half—Model IV	19
7	Detail of Lower Cell Half—Model IV	20
8	Detail of Insulators—Model IV	21
9	Detail of Electrolyte Feed Ring—Model IV	22
10	Exploded View of Model IV LMC	23
11	Detail of Star Design Matrix	24
12	Detail of Radius Design Matrix	25
13	Detail of Rib Design Matrix	25
14	Detail of Conductivity Cell	26
15	Fabricated Conductivity Cell	27
16	Time-Phased Chart	31
17	Dense Ceramic-Metal Seal Test	33
18	Ceramic Insulators from Seal Test	33
19	Ceramic Insulators from Seal Test	33
20	Dense Ceramic-Porous Ceramic-Metal Seal Test—High Unit Load Insulator	34
21	Dense Ceramic-Porous Ceramic-Metal Seal Test—Lower Unit Load Insulator	34
22	Dense Ceramic-Porous Ceramic-Metal Seal Test—Upper Cell Half	34
23	Dense Ceramic-Porous Ceramic-Metal Seal Test—Lower Cell Half	35
24	Dense Ceramic-Insulator and Matrix Half	35
25	Dense Ceramic-Insulator and Matrix Half	36
26	Dense Ceramic-Matrix Halves	36
27	Compressive Testing Equipment	37
28	Thickness vs Ultimate Compressive Strength for LM-833 Magnesia	38



<u>Figure</u>	<u>Title</u>	<u>Page</u>
29	Top Side of Ruptured Star Matrix	41
30	Bottom Side of Ruptured Star Matrix	42
31	Break Pattern of 7.62-cm Radius Matrix	42
32	Five-Rib Matrix Break.	43
33	Eight-Rib Matrix Break	43
34	Matrix Impact Rupture Strength vs Electrical Cross Section.	44
35	Rupture Pressure vs Square of Average Thickness.	46
36	Test 1, Model III—Mercury Chamber.	48
37	Test 1, Model III—Mercury Chamber with Insulator.	48
38	Test 1, Model III—Matrix and Feed Ring, Potassium Side.	49
39	Test 1, Model III—Matrix and Feed Ring, Mercury Side.	49
40	Test 1, Model III—Potassium Chamber.	50
41	Test 1, Model III—Broken Insulator	50
42	Test 1, Model III—Broken Insulator	50
43	Test 2, Model III—Test Setup.	52
44	Test 2, Model III—Cell After Test	52
45	Test 2, Model III—Mercury Chamber.	53
46	Test 2, Model III—Potassium Chamber.	53
47	Test 2, Model III—Matrix and Feed Ring, Potassium Side.	54
48	Test 2, Model III—Matrix and Feed Ring, Mercury Side.	54
49	Heat Balance Flowmeter	55

LIST OF TABLES

<u>Table</u>	<u>Title</u>	<u>Page</u>
I	Cell Performance to Date	2
II	Important Physical Properties of Pure Sintered Ceramics Useful in Liquid Metal Cell Construction	7
III	Important Thermal and Electrical Properties of Pure Sintered Ceramics Useful in Liquid Metal Cell Construction	8
IV	Physical Characteristics of A-402 Impervious Alumina	8
V	Physical Characteristics of LM-833 Porous Magnesia	9
VI	Physical Characteristics of M Porous Magnesia	9
VII	Important Properties of Kovar Alloy	11
VIII	Compressive Strengths of Porous Ceramics vs Time in Electrolyte	39
IX	Bursting Strengths of Matrix Designs	40
X	Performance of Model III Cell	56

GLOSSARY OF TERMS

A, LA, LM, M, and RR---Terms used in conjunction with some number to refer to a manufacturer's product designation

Anolyte---The fluid contained within the anode compartment of an electrochemical device

Catholyte---The fluid contained within the cathode compartment of an electrochemical device

Cell---A Single cell consisting of an anode chamber, electrolyte or electrolyte-matrix, and a cathode chamber

Cell Unit---A number of cells in electrical series to provide a basic package of given operating voltage

Cell Stack---A group of cell units arranged in such a manner as to provide a package of given wattage

Kovar---A nickel-cobalt-iron alloy known for its low thermal expansion

Matrix---A porous structure which forms the foundation and physical limits of a liquid impregnant

Spinel---A ceramic compound of the formula $MgO \cdot Al_2O_3$

Silicone Rubber---A synthetic elastomer consisting of cross-linked chains of a basic-O-SiR₂-bonding (capable of higher temperature regimes than most rubbers)

Weir---A dam-like device used to maintain a liquid at some fixed level

LIST OF SYMBOLS AND DEFINITIONS

<u>Symbol</u>	<u>Description</u>
A	Area (or representation of a liquid metal, where appropriate)
B	Representation of a liquid metal
D	Diameter
E	Reversible electrical potential
F	Faraday
(F)	Formation Factor
$\Delta G, \Delta \bar{G}$	Free energy, partial molar free energy
ΔH	Enthalpy
I	Current
I_k	Constant current
K	Cell constant
$^{\circ}K$	Degrees Kelvin
K_e	Equilibrium constant
L_e	Length of tortuous path
M	Mass
N	Mole fraction
P	Actual porosity
P_m	Load
P_e	Effective porosity
R	Gas constant
R_m	Radius
R_e	Electrical resistance
ΔS	Entropy
T	Absolute temperature
V	Voltage
V_o	Open circuit voltage
V_c	Cell or operating voltage
Vol	Volume
W	Power
a	Activity
cal	Calorie
cm	Centimeter
d	Density



<u>Symbol</u>	<u>Description</u>
d_m	Density of porous body
d_B	Bulk density
g, gm	Grams
k	Conductivity
\ln	Natural logarithm
mv	Millivolts
n	Electron charge
p	Pressure
(s)	Solid
sec	Second
t	Time
t_e	Length of straight path
x	Concentration of stoichiometric ratio
y	Stoichiometric ratio
z	Flow rate
a	Activity coefficient
η_c	Voltage efficiency, V_c/V_o
θ	Wetting angle
μ	Microns
$\mu\mu f$	Micromicrofarads
ρ	Electrical resistivity
ρ_e	Electrical resistivity of pure electrolyte
σ	Surface tension
τ	Tortuosity
ϕ	Actual porosity
Ω	Ohms

I. INTRODUCTION

In the late 1950's a comprehensive survey was made of the fuel cell literature.^{1*} From this survey it was noticed that very little work was being done on regenerative systems—a surprising observation considering the preponderance of thermal energy available from both solar and nuclear sources. It was then suggested that thermal and electrochemical regenerative systems should be studied.² Pursuing these leads further, it was decided to determine the problems associated with such systems and what inorganic compounds would lend themselves to thermal regeneration. A survey of the literature for thermally decomposable inorganic compounds³ revealed only about 20 compounds suitable for thermally regenerative systems based on more or less practical criteria, while another evaluation⁴ based on thermodynamic and kinetic data produced only two suitable reactions for inorganic compounds. A general systems analysis⁵ revealed that the greatest improvement in efficiency of regenerative systems could be accomplished by reductions in polarization and electrolyte resistance losses. It is known that the kinetics of liquid metal electrodes in contact with fused salts is extremely rapid.⁶ Also, the conductivity of fused salts is possible two to five times greater than the conductivity of the best aqueous electrolytes.⁷ With these improvements as a goal, work was initiated at Allison to develop the liquid metal cell (LMC).

The liquid metal cell is a thermally regenerative static power converter in which heat is converted directly into electrical energy. No reaction mass is consumed in the generation of the electrical energy. The LMC power converter system contains no moving parts and allows complete control over output electrical energy to be accomplished by external electrical devices. These features make the LMC attractive for use with nuclear reactor or radioisotope thermal sources necessary for missions of long duration.

Application of the LMC power converter is attractive for such space missions as Voyager, Mariner, orbiting space stations, or any mission where electrical energy is required over long time periods at a high reliability confidence level. In particular, missions which utilize the SNAP II reactor are adaptable to the LMC power converter because electrical output, reactor temperature level, and converter system size, weight, and volume are compatible with the proposed SNAP II power converter system requirements. The LMC can provide significant reductions in system weight due to the dual capability of the LMC to provide electrical power and, at the same time, particle gamma shielding. As a consequence, the long-

*Superscripts refer to references in Section VII.



range program has been directed toward the following system goals:

- Capable of one year reliable space operation with a power output of 5 kw at 28 volts
- Capable of remote, unattended start-up and shutdown in space operation
- Capable of withstanding the vibration, shock, and acceleration experienced during prelaunch, launch, and orbit of a space vehicle
- High power-to-mass values
- Shelf life of six months

During the first year's contract, 22 liquid metal cells were operated—establishing the electrochemical feasibility of the potassium-mercury couple, and demonstrating the ability to operate at constant output voltage when mercury was flowing through the cell. Difficulties were encountered when the ceramic matrices being used revealed chemical incompatibilities with the ternary electrolyte, so that most cells run were of the differential density (matrixless) type (Figure 1). In this type of cell, the densities of the metals and electrolyte made possible the floating of potassium (0.7 gm/cm^3) on electrolyte (2.4 gm/cm^3) and electrolyte on mercury (12.9 gm/cm^3).

Table I lists maximum performances obtained on the first year's tests.

TABLE I
Cell Performance to Date^a

CURRENT DENSITIES

Differential Density Cells (Pure Electrochemical System)

Static— 227 ma/cm^2 Flow— 109 ma/cm^2

Extrapolated to Maximum Power

Static— 225 ma/cm^2 Flow— 247 ma/cm^2

Matrix-Type Cells

Static— 150 ma/cm^2 Flow— 77 ma/cm^2

Extrapolated to Maximum Power

Static— 207 ma/cm^2 Flow— 78 ma/cm^2

TABLE I (Cont)

POWER DENSITIES

Differential Density Cells (Pure Electrochemical System)

Static--87 mw/cm² Flow--57 mw/cm²

Extrapolated to Maximum Power

Static--111 mw/cm² Flow--128 mw/cm²

Matrix-Type Cells

Static--91 mw/cm² Flow--41 mw/cm²

Extrapolated to Maximum Power

Static--107 mw/cm² Flow--41 mw/cm²

A flowing differential density cell was run for six continuous hours at 50 mw/cm², and a total of 35 hours of running time was accumulated for this type of cell.

Under the present contract, major emphasis will be placed on achieving: (1) desired performance from cells with matrices; (2) a reliable cell seal; and (3) power from an integrated module of three cells connected in series electrically.

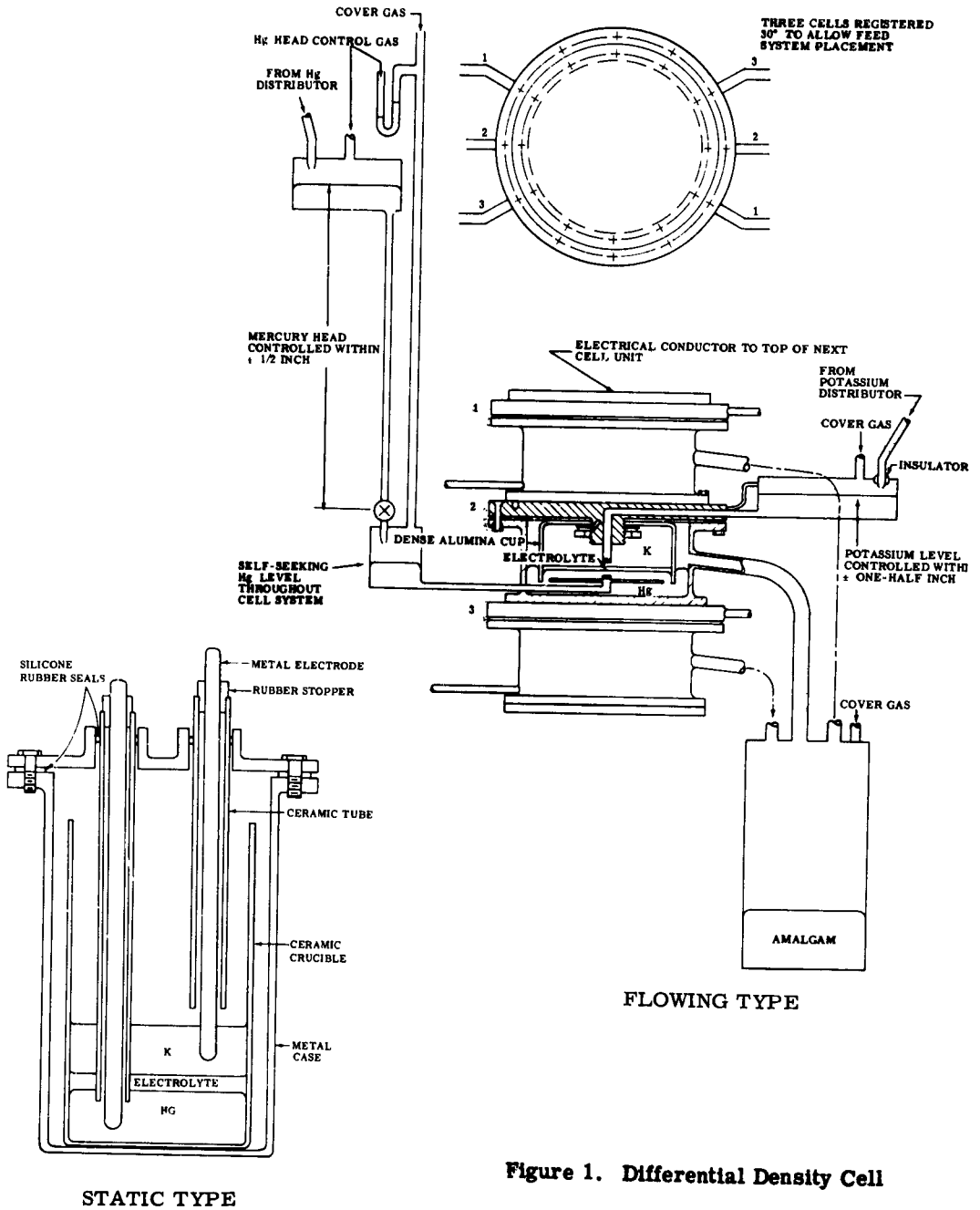


Figure 1. Differential Density Cell

II. MATERIALS

CERAMICS FOR MATRICES AND INSULATORS

The main criteria in the choice of ceramic materials are:

1. Compatibility with the mercury-potassium amalgam and electrolyte systems.
2. (For matrices) Apparent porosity, pore size, and distribution of the pores among the three possible types--pores open on both ends, pores open on one end, and pores closed on both ends. The maximum porosity attainable would be desirable because this would lend itself to absorption of the greatest amount of electrolyte in the pores open on both ends. However, a retention of the electrolyte under a differential head is important, and, for this reason, it would be critical to control the pore size so that maximum electrolyte retention can be attained.
3. Availability.
4. Stability against thermal shock.
5. Cost.

Any characterization of the properties of oxide ceramics is an extremely difficult task. Chemical, physical, or mechanical properties are highly dependent on the nature of preparation of the finished material, the extent of sintering, the presence of impurities, the type of binder used to hold the particles together, the porosity (as reflected in the surface area), and the degree of wetness or dryness. In the interests of clarity, tabulation of properties will be made on three bases:

1. Expected behavior of the basic, pure ceramic material (this would involve the chemical behavior of the pure powder, or of a dense, sintered solid in which no binder is used)
2. Physical properties of highly dense, sintered bodies (this would give a reasonable comparison in a standard condition between the various materials considered)



3. Available information on porous ceramics, which may or may not incorporate a binding material (this would summarize some of the materials tested for compatibility and offer a means by which the change in properties of the material, as it takes on porosity, may be determined)

Pure Ceramics (Chemical Properties)

Present indication is that an oxide-type ceramic will be required for durability as a matrix material in the liquid metal cell. Among the many oxide ceramics in existence, the following are deemed the best for consideration in the present cell configuration:

- Magnesia—MgO
- Spinel—Al₂O₃. MgO
- Thoria—ThO₂

A detailed discussion of the oxide ceramics under consideration is given in the following:

- Magnesia—Compatibility with mercury is good up to 873°K.⁹

Compatibility with alkali metals is good up to 473°K⁹ with the area above that unknown, although Ryskewitch¹⁰ states "The chemical behavior of magnesia is determined by the position of magnesium in the periodic table. The element is a weak representative of the earth alkali metals. Accordingly, magnesia is a weak base, particularly at high temperatures. Therefore, a sintered magnesia body is not, or almost not attacked by basic substances, such as alkalis, and alkali carbonates, even in prolonged action in the molten state."

Smith¹¹ mentions the testing of magnesia in fused alkali hydroxides at "substantial temperatures" with no evidence of reaction.

Magnesia may react at elevated temperatures with free halogens which might be released by the thermal decomposition of the electrolyte according to Equation (1).¹⁰



In the presence of carbon, magnesia chlorination begins at 473°K.

Magnesia is more sensitive to thermal shock than is alumina.

- Spinel—Magnesium meta-aluminate, $MgO \cdot Al_2O_3$, offers some potential as a ceramic material that would combine the best features of magnesia and alumina—the corrosion resistance approaching that of magnesia and the thermal shock resistance better than that of magnesia.
- Thoria—Compatibility with mercury should present no problem. Compatibility data for reactions with alkali metals are scarce. Thoria is known to react with alkalis at temperatures of 1673°K in a closed, pressurized vessel.¹⁰

Thoria should be the least reactive of all the materials mentioned with molten alkali salts.

Of the three oxide ceramics—magnesia, spinel, and thoria—thoria is the most subject to thermal shock and great care would be needed in its preparation to remove residual firing stresses.

Pure Sintered Ceramics (Physical Properties)

Densified ceramics will be needed for use as gaskets or other structural members in a liquid metal cell. Some design information should be available for this purpose. Use of oxide ceramics as matrices requires some means for estimating relative properties of these ceramics as porous bodies—even though it is acknowledged that the properties will be strongly affected by methods of preparation. It is with this in mind that the physical properties are summarized in Tables II and III.

TABLE II
Important Physical Properties of Pure Sintered Ceramics Useful
in Liquid Metal Cell Construction¹⁰

<u>Material</u>	<u>Theoretical Specific Gravity (gm/cm³)</u>	<u>Compressive Strength (kg/cm²)</u>	<u>Tensile Strength (kg/cm²)</u>	<u>Melting Point (°K)</u>
Alumina	3.96-3.98	15,000 (673°K)	2560 (573°K)	2323
Magnesia	3.57	< Alumina	< Alumina	3078
Spinel	3.60	16,000 (573°K)	1200 (573°K)	2408
Thoria	10.05	11,000 (673°K)	1000 (298°K)	3573

Note: The tensile strength of heat treated steel is 4500 kg/cm² at 673°K



TABLE III
Important Thermal and Electrical Properties of Pure Sintered
Ceramics Useful in Liquid Metal Cell Construction¹⁰

<u>Material</u>	<u>Specific Resistivity (ohm-cm)</u>	<u>Specific Heat (cal/gm/°K)</u>	<u>Thermal Conductivity (cal/cm²/cm/sec/°K)</u>	<u>Coefficient of Thermal Expansion (cm/cm/°K)</u>
Alumina	10 ⁸ (1103°K)	0.258 (303-1173°K)	0.0538 (473°K) 0.0314 (673°K)	7.3 × 10 ⁻⁶ (298-773°K)
Magnesia	10 ⁹ (803°K)	0.277 (303-1173°K)	0.038 (573°K)	12.0 × 10 ⁻⁶ (573°K)
Spinel	10 ⁸ (673°K)	0.194 (303°K)	0.032 (573°K)	6.7 × 10 ⁻⁶ (298-1073°K)
Thoria	10 ⁹ (823°K)		0.020 (473°K) 0.014 (673°K)	9.7 × 10 ⁻⁶ (96% dense)

Only one impervious material has been used in cell construction for this program. This material is a high quality alumina and is used because of previous satisfactory performance over the time spans encountered plus an unavailability of other dense ceramics in the required configuration. For this reason the properties of pure aluminum oxide are listed in Tables II and III. Table IV contains the properties of the material actually in use for insulators.

TABLE IV
Physical Characteristics of A-402 Impervious Alumina¹²

Typical Chemical Analysis

Al ₂ O ₃	99.0%	CaO	0.3%
MgO	0.3%	SiO ₂	0.2-0.4%
Fe ₂ O ₃	0.03%	Alkali (Na ₂ O)	0.03%
TiO ₂	Trace		

Temperature of Maximum Use—2173°K
 Specific Gravity—3.80 (pure oxide, 3.97) gm/cm³
 Apparent Porosity—0%
 Specific Heat—0.27 cal/gm/°K
 Coefficient of Thermal Expansion¹³ —5.9 × 10⁻⁶ cm/cm/°K

Porous Ceramics

In the early stages of the LMC program, many porous ceramic materials were tested to determine their suitability for use.⁸ Selection was not always difficult since a great many of the materials disintegrated completely when immersed in electrolyte. For the most part, those that did not disintegrate evidenced increasing electrical resistance when used as matrices in liquid metal cells. Information gained from that testing program largely delineated acceptable and unacceptable formulations, so that today much more discriminating methods are needed to distinguish the useful materials from those that are not. A General Motors program, which is a companion to this Air Force program, is being used to select those oxide ceramics even more suitable than those available. Selection of compatible materials is based primarily on two parameters—change in compressive strength vs time, and change in electrical resistivity vs time. These two tests will lay the groundwork necessary for optimization of the potassium-mercury liquid metal cell. (See Section III, Apparatus.)

Table V¹² lists the known properties of the most readily available porous magnesia material, and Table VI¹⁴ shows the properties of another experimental porous magnesia.

TABLE V
Physical Characteristics of LM-833 Porous Magnesia

Typical Chemical Analysis

MgO	99.0% min	Fe ₂ O ₃	0.15% max
SiO ₂	0.2% max	R ₂ O ₃	0.35% max
CaO	0.2% max	B	0.003% max
TiO ₂	0.1%		

Apparent Porosity—40 to 45%

Pore Size LM-833 20 μ

TABLE VI
Physical Characteristics of M Porous Magnesia

Typical Chemical Analysis

MgO	97.0% min	Fe ₂ O ₃	0.07%
SiO ₂	2.07%	PO ₄ ⁼	0.01%
CaO	0.03%	SO ₄ ⁼	0.01%

Bulk Density—2.06%

Apparent Porosity—40 to 45%



A 36% porous material (L Spinel) is now under test, and several new materials are awaiting the start of testing—R Spinel, NB Thoria, L Thoria, and NB Magnesia. At present, no information is available on the properties of these materials.

The apparent porosity is determined by dividing the actual density of the material by the density (Table II) of the pure oxide. The apparent porosity represents the three possible types of pores—those open on both ends, open on one end, and totally enclosed. The pores open on both ends or on one end can be determined by an absorption method.¹⁵

METALS

A discussion of properties of liquid metal reactants and of metals for containment of liquid metals will be found in Reference 8. However, one new material (Kovar) has been used extensively in this year's work since its thermal expansion closely matches that of the A-402 gaskets used for insulating cells. The properties of Kovar are listed in Table VII.¹⁶

Compatibility studies to date indicate no consequential attack on Kovar by either the ternary electrolyte, potassium metal, or mercury metal.

ELECTROLYTE

The electrolyte is a molten salt mixture containing potassium as the common cation. This electrolyte was chosen initially on the criteria of proper melting point, lack of reaction with the liquid metals, matrix, or container, the absence of thermal decomposition, and good electrical conductivity. The ternary system KOH-KBr-KI has been used for cell work to date. The eutectic composition is approximately 70 mole percent KOH, 15 mole percent KBr, and 15 mole percent KI, and has a melting point, when dry, of 493°K. The electrolyte was reported⁸ to have a resistivity of 1 ohm-cm at cell temperature, but recent information suggests that the actual value may or may not be somewhat higher (see appendix)—perhaps as high as 2.5 ohm-cm. Further definition of resistivity values will be reported as information develops. Higher values of resistivity would require thinner electrolyte cross sections in order to achieve some fixed performance levels.

TABLE VII
Important Properties of Kovar Alloy¹⁶

Chemical Composition

Nickel	28% (nominal)
Cobalt	17% (nominal)
Iron	Remainder
Manganese	0.50% (maximum)
Silicon	0.20% (maximum)
Carbon	0.08% (maximum)
Aluminum	0.10% (maximum)
Magnesium	0.10% (maximum)
Zirconium	0.10% (maximum)
Titanium	0.10% (maximum)

Total of Al, Zr, and Mg not to exceed 0.20%

Density—8.37 gm/cm³

Coefficient of Thermal Expansion

Temperature Range (°K)	Average Linear Coefficient of Thermal Expansion (cm/cm/°K × 10 ⁻⁶)
303-475	5.04
303-573	4.86
303-673	4.74
303-773	6.19

Thermal Conductivity

Temperature (°K)	Thermal Conductivity (cal/cm ² /cm/°K/sec)
303	0.0395
573	0.0485

Electrical Resistivity

Temperature (°K)	Resistivity (microhm-cm)
298	49.0
373	62.8
473	80.4
673	107.3

Melting Point—1723°K

Specific Heat

Temperature (°K)	Specific Heat (cal/gm/°K)
273	0.105
703	0.155

III. APPARATUS

LIQUID METAL CELLS

The purpose of this section is to establish in detail the types of devices used in the test program, and to establish dimensions, etc, for future reference. Further discussion, results, and evaluation are given in Section IV, Experimental Results.

Sealing Test Cells

The sealing test cells (Figure 2) are very simple and are used to test seals using low (3 mole percent) potassium amalgams. Each cell half has a single filling tube, a single vent tube, and a thermocouple well and is constructed of stainless steel. Chamber diameter is 7.62 cm and chamber depth is approximately 0.32 cm.

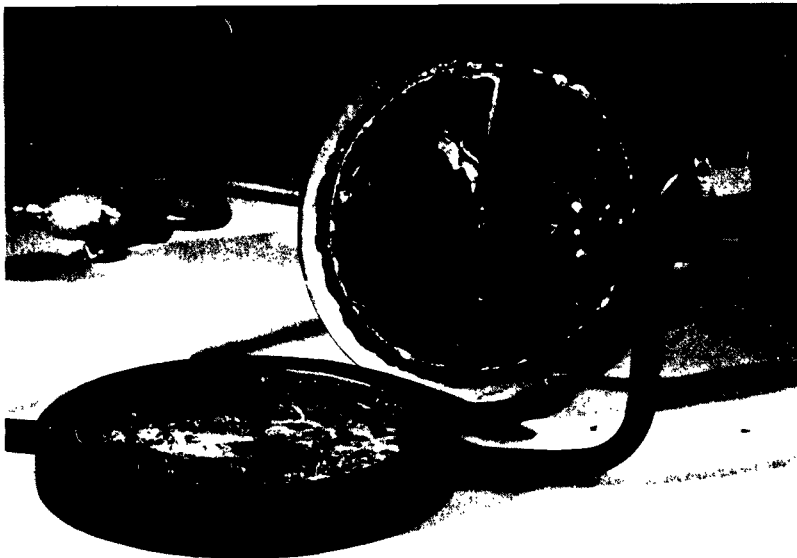


Figure 2. Sealing Test Cell



Model III LMC*

As sealing procedures were proved for low potassium amalgams, the evolution of the liquid metal cell design called for a cell capable of being sealed in its final configuration—using electrolyte and liquid metal feed. Basic design philosophy called for a layered structure, as follows (from top to bottom):

1. Upper cell half
2. Impervious alumina insulator or gasket
3. A Matrix sandwich
 - Two thin matrix pieces with a small gap between to allow for free electrolyte
 - A metal ring enclosing the matrix sandwich to provide an electrolyte feed annulus
4. Impervious alumina insulator
5. Bottom cell half

The matrix sandwich provides several advantages:

1. It allows replenishment of any electrolyte which may bleed into the liquid metal stream. (This possibility should be optimized out of the system later, when effect of pore size is better understood.)
2. It ensures 100% saturation of the matrix at all times.
3. It prevents internal short circuits through the matrix due to preferential wetting of the pores by liquid metal.
4. Electrolyte feed could provide a convenient method of heat dissipation at high current densities.

*Models I and II refer to cell designs considered in previous work.

The cell shown in Figures 3, 4, and 5 was constructed and tested (see Section IV, Experimental Results). Kovar was used for the cell halves, and the electrolyte feed ring was stainless steel for the first test run and Kovar for the second test run. The identification numbers in Figure 3 are defined as follows:

- One (1) indicates the outer or secondary sealing ledge of the cell half, separated from the inner seal ledge by the seal sampling annulus.
- Two (2) represents the feed and effluent tubes.
- Three (3) indicates the tubes used to detect mercury liquid or vapor which might have leaked beyond the inner seal.
- Four (4) indicates the thermocouple well.
- Five (5) points to the vents which allow gas to bleed from the cell to allow for complete filling. All cells were run at a 9° angle to aid in venting. (This will not be necessary in a regenerative-closed-loop system.)

Model IV LMC

Test results from the Model III cell indicated that improvements could be made in compactness, flow characteristics, and sealing. Consequently, the cell shown in Figures 5, 6, 7, 8, 9, and 10 was constructed as Model IV.

Feed apertures were changed to allow for less local deflection under load; a centering lip was added, feed tubes were changed to manifolds for compactness, and a power bus was added as an integral part of the structure. Note the concentric ribs on the ceramic insulators in Figure 10—these are used to provide locally high loads to coin the insulator into the Kovar cell half.

MATRIX DESIGN STUDIES—BURST TEST SAMPLES

Cell performance will depend in part on the IR drop through the electrolyte-matrix combination according to:

$$R = \frac{\rho t_e}{A} \quad (2)$$

where

R is the resistance in ohms

ρ is the electrolyte-matrix resistivity in ohm-cm

A is the electrode area in cm²

t_e is the electrical cross section or thickness

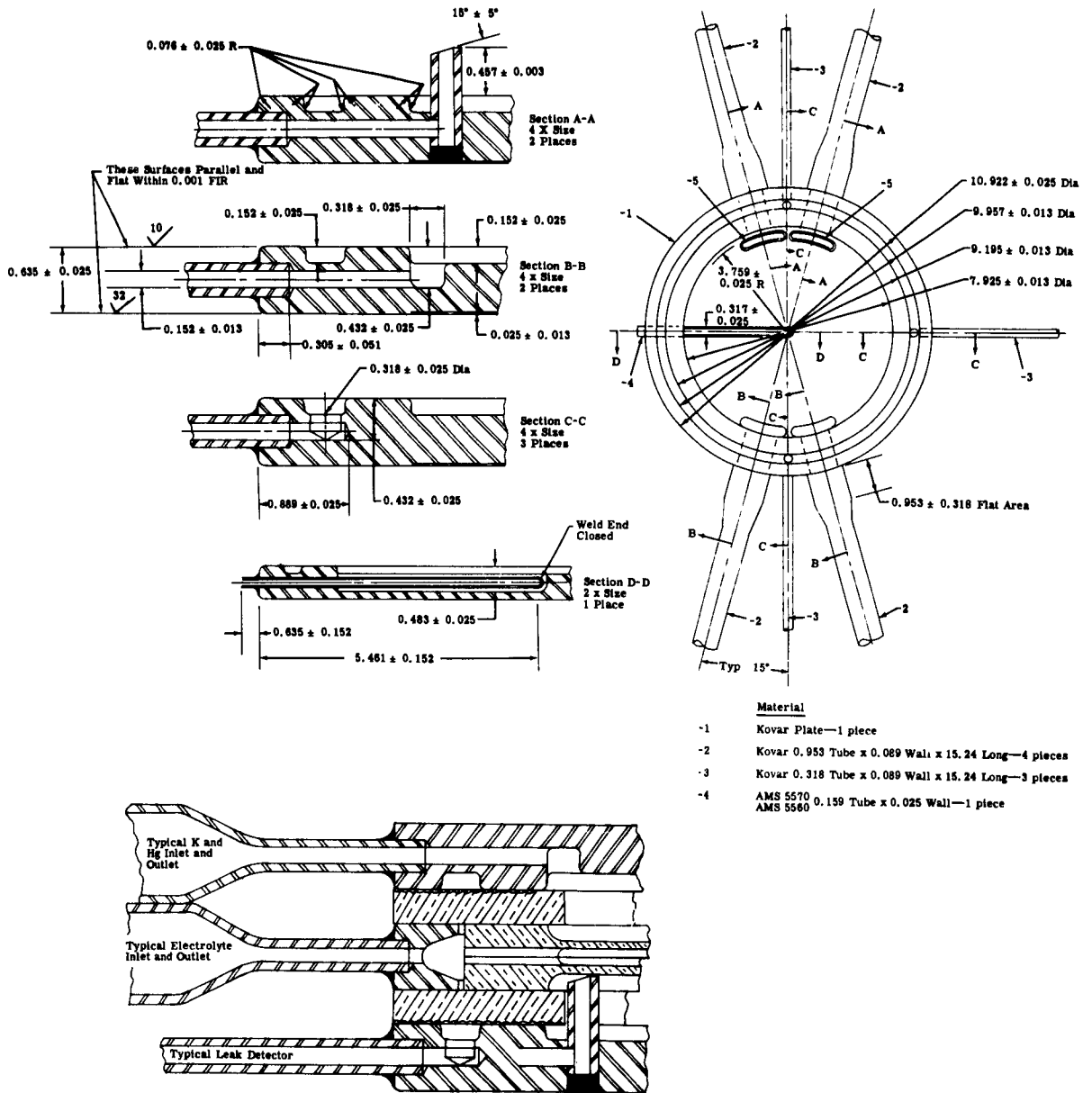


Figure 3. Detail of Cell Half—Model III

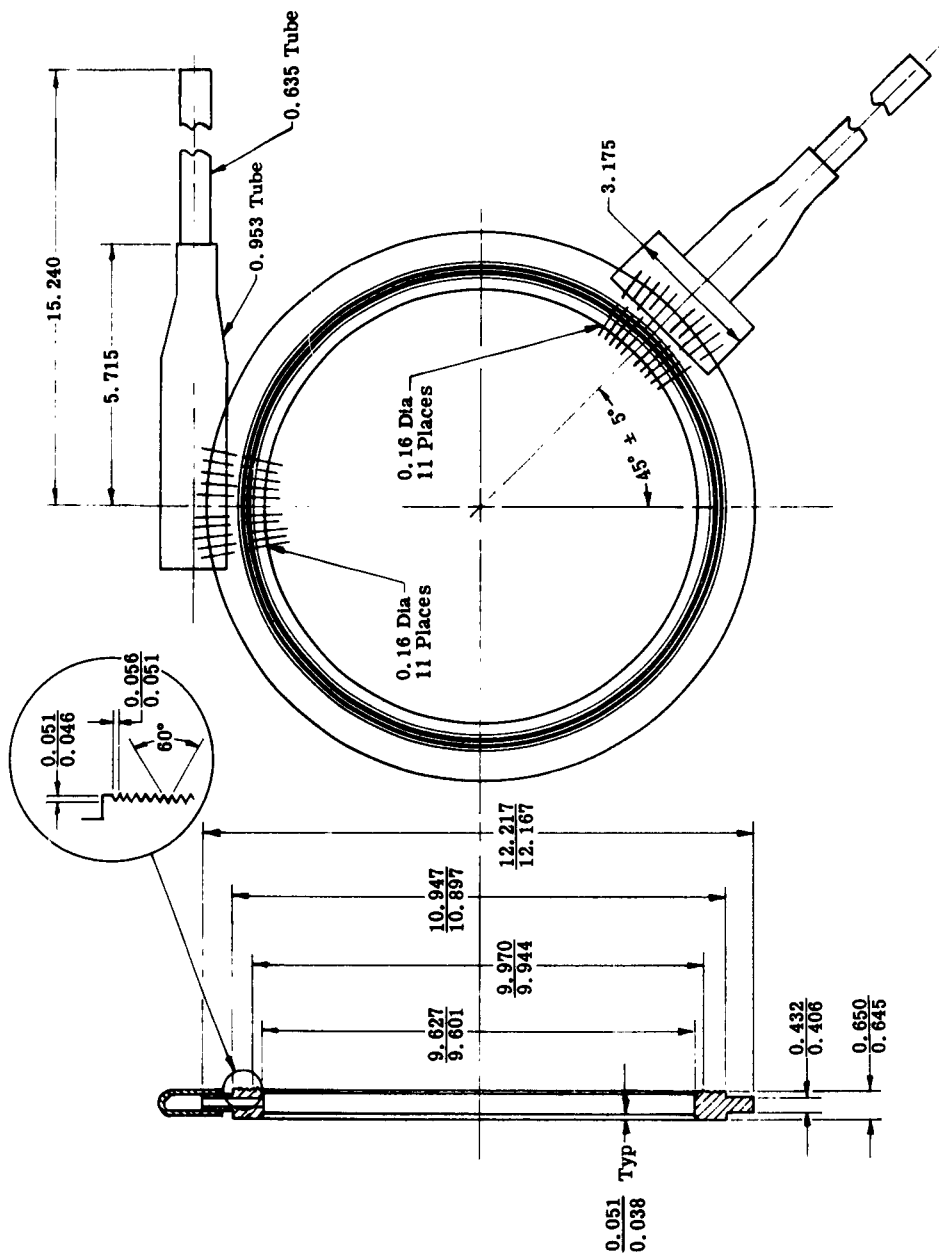
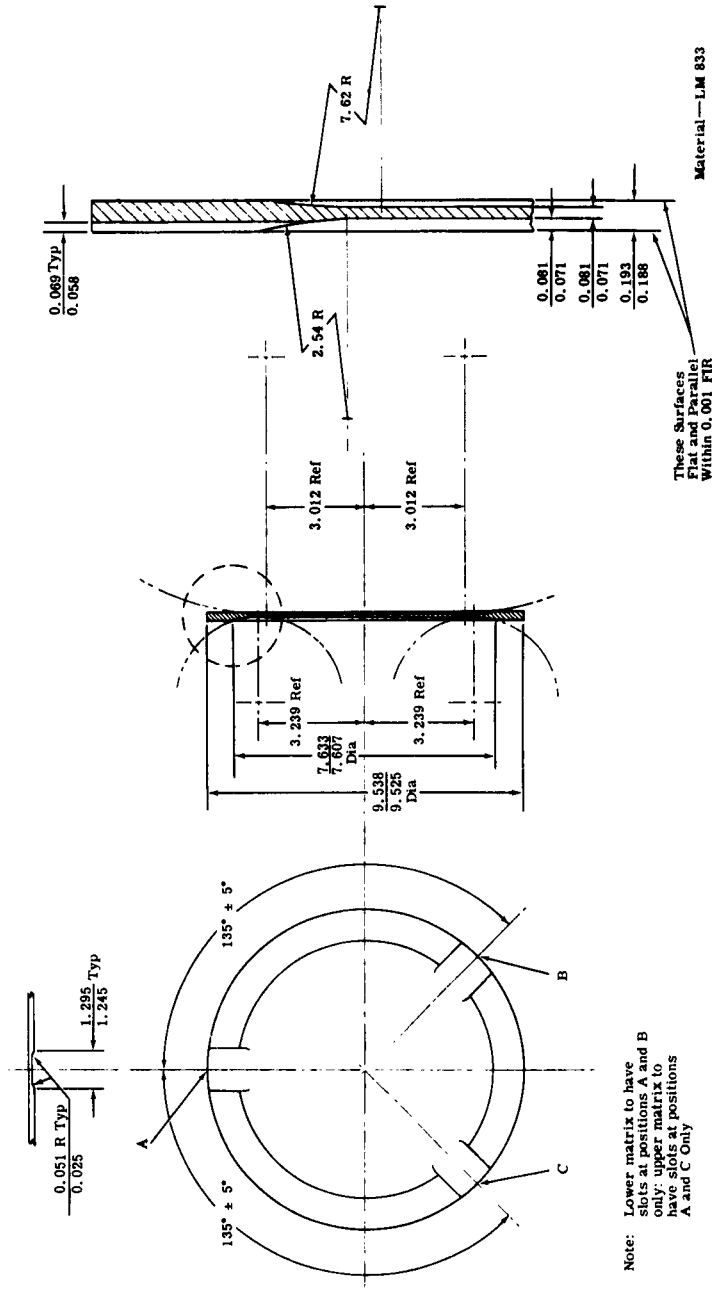


Figure 4. Detail of Electrolyte Feed Ring—Model III



Note:
 Lower matrix to have
 slots at positions A and B
 only; upper matrix to
 have slots at positions
 A and C Only

Figure 5. Detail of Matrix Half—Models III and IV

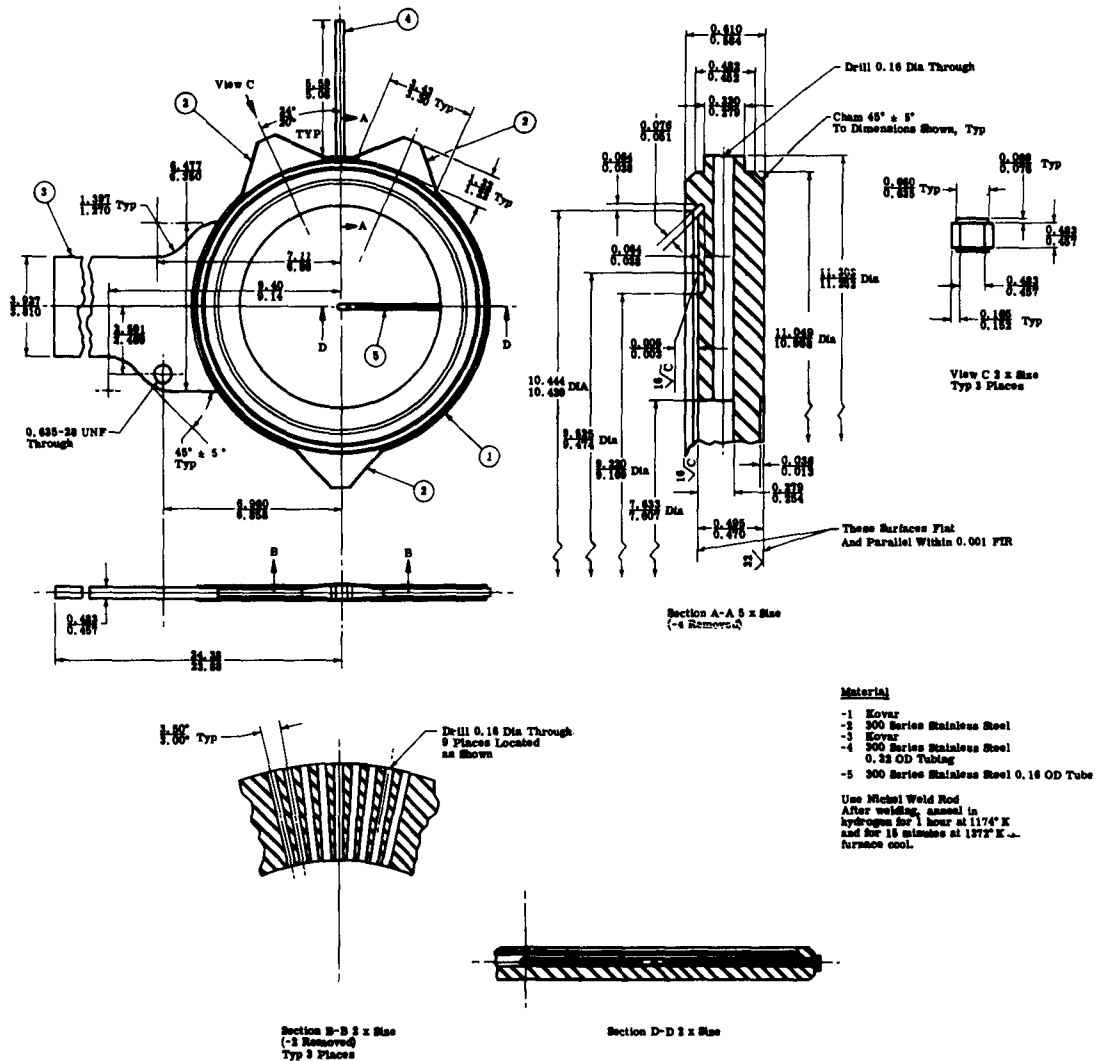


Figure 6. Detail of Upper Cell Half—Model IV

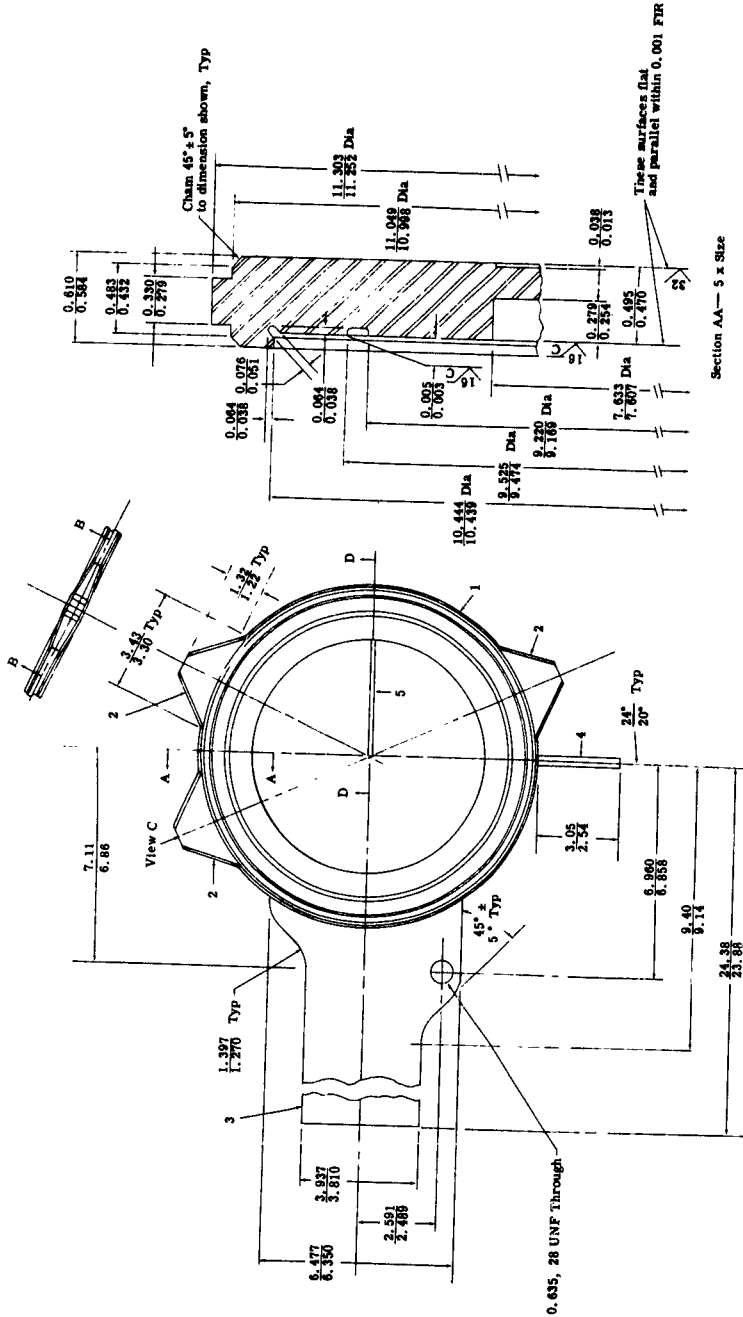


Figure 7. Detail of Lower Cell Half—Model IV

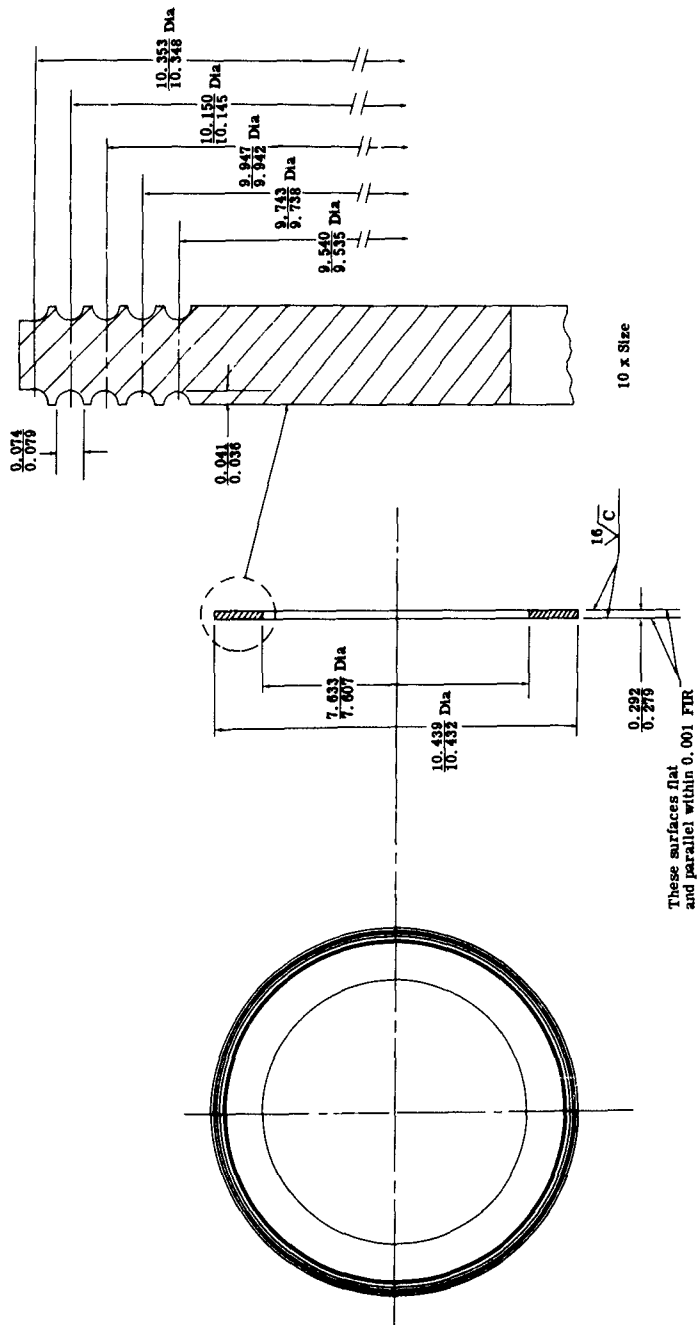


Figure 8. Detail of Insulators — Model IV

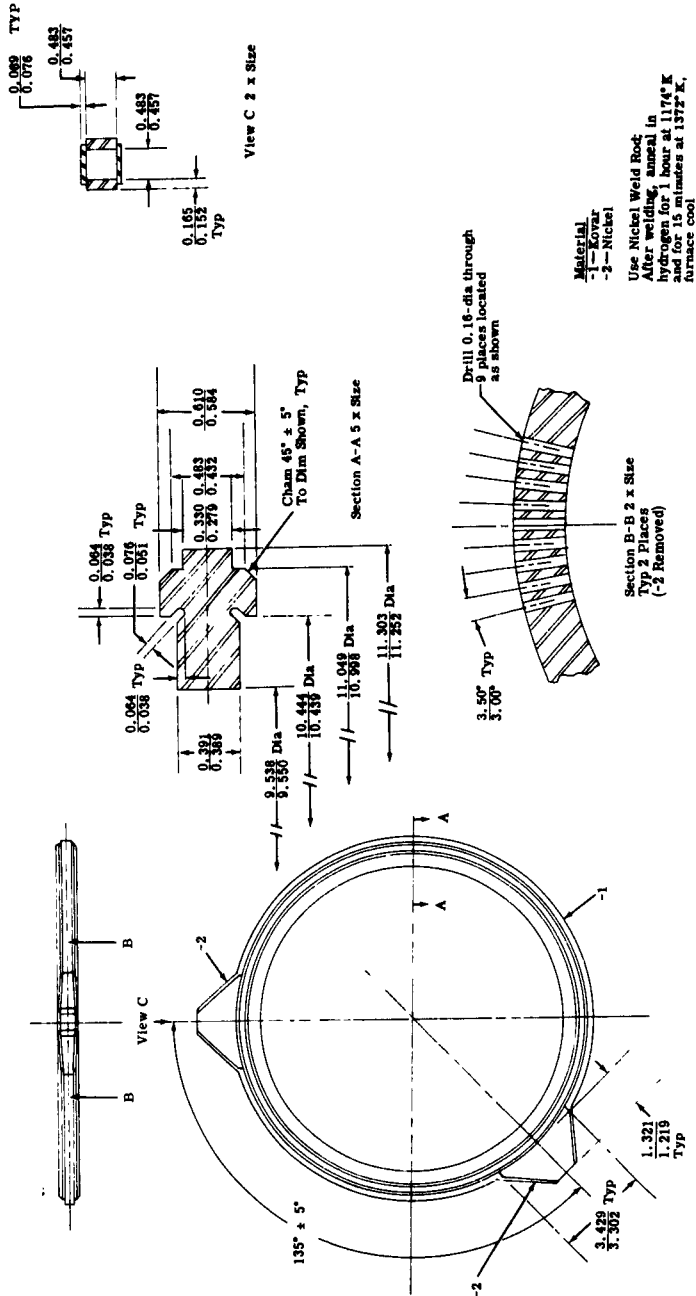


Figure 9. Detail of Electrolyte Feed Ring—Model IV

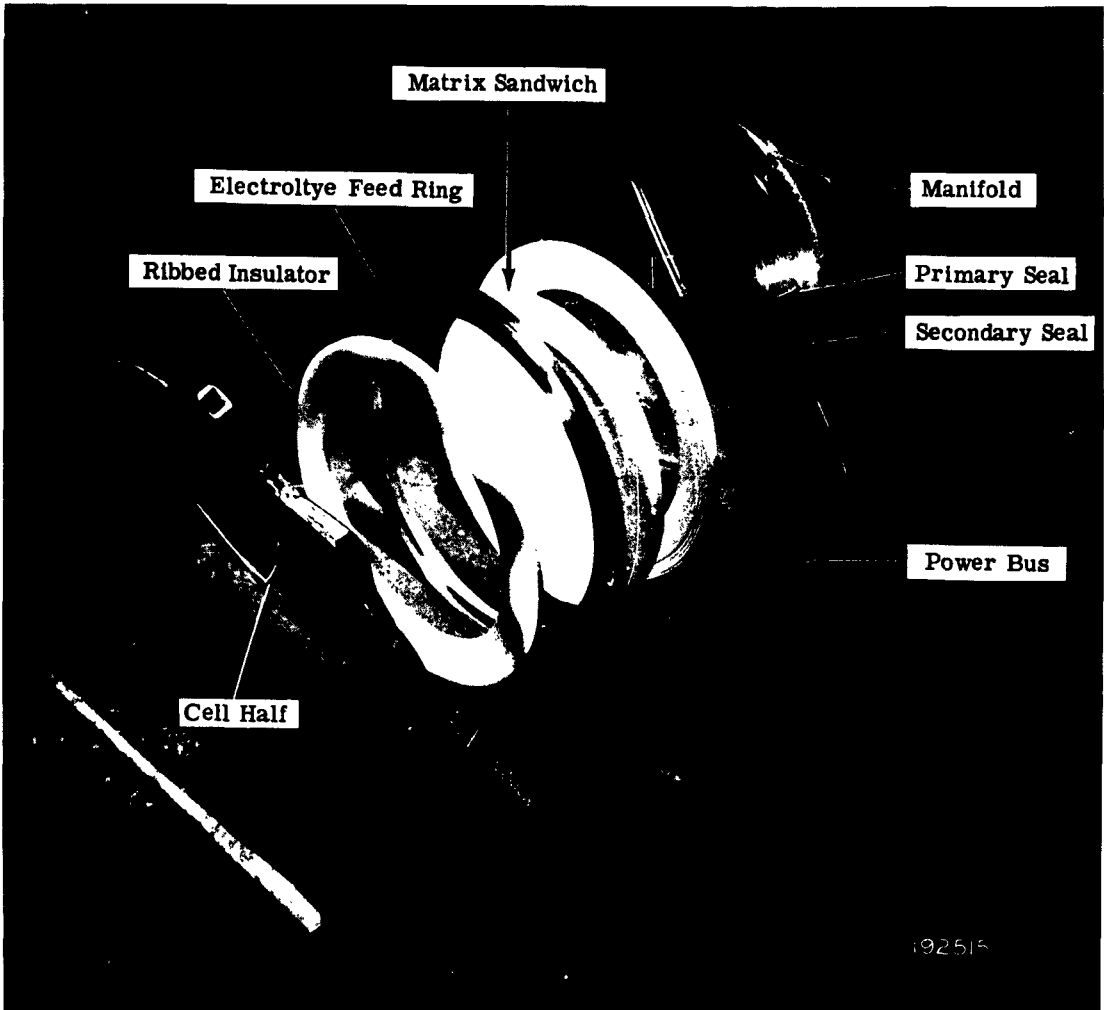


Figure 10. Exploded View of Model IV LMC



Therefore, performance-wise, it would be desirable to have the value t_e as small as possible, which means thinning down the matrix, at least over that portion covering the electrode. There are two major factors, however—one is the ability to machine the ceramics, and the other is the ability to maintain the mechanical strength required in the thinned down section.

Consequently, the best solution would be to use as thin a section as possible while leaving some thicker ribbing or supporting structure. Then, some mechanical parameter, such as bursting strength, can be optimized against an electrical parameter, such as average thickness or the electrical cross section which the electrodes would encounter. The goal would be highest strength for a given estimated voltage drop.

Figures 11, 12, and 13 show details for three different design configurations which were tested. The star design uses partial radial ribs on one side and a straight dish-out on the other. The radius design uses gentle radii to dish-out both sides, and the ribbed design uses straight ribs and a dish-out. When two such thinned down halves are placed together to form a matrix sandwich, they have a space sufficient to allow for electrolyte flow.

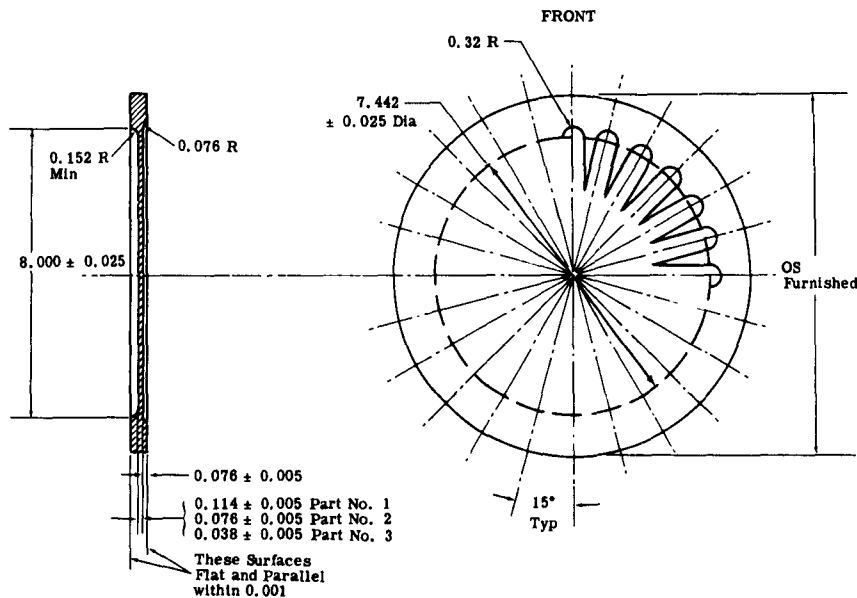


Figure 11. Detail of Star Design Matrix

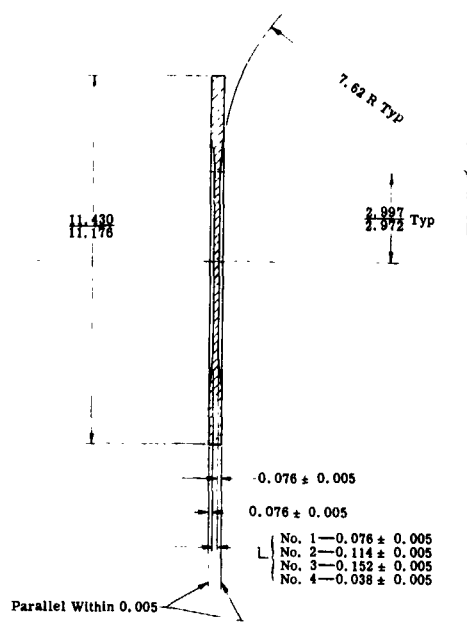


Figure 12. Detail of Radius Design Matrix

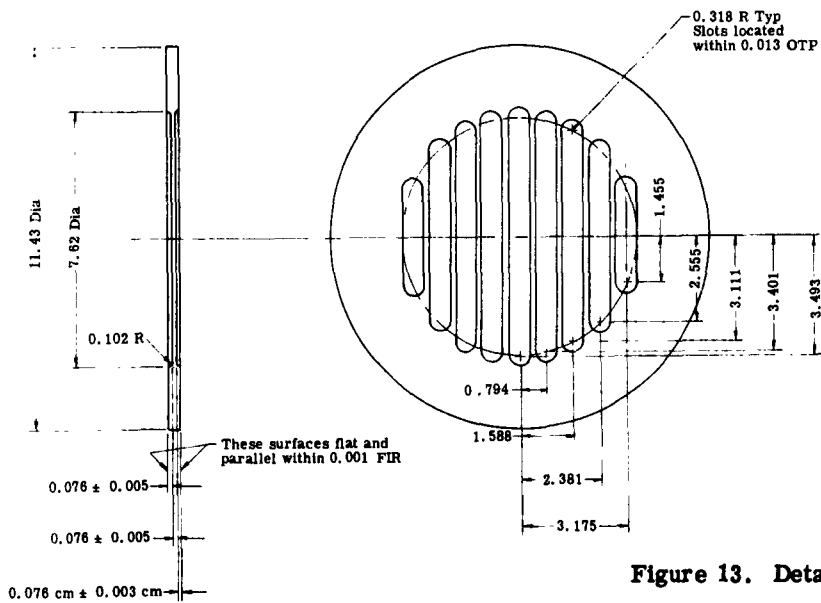


Figure 13. Detail of Rib Design Matrix

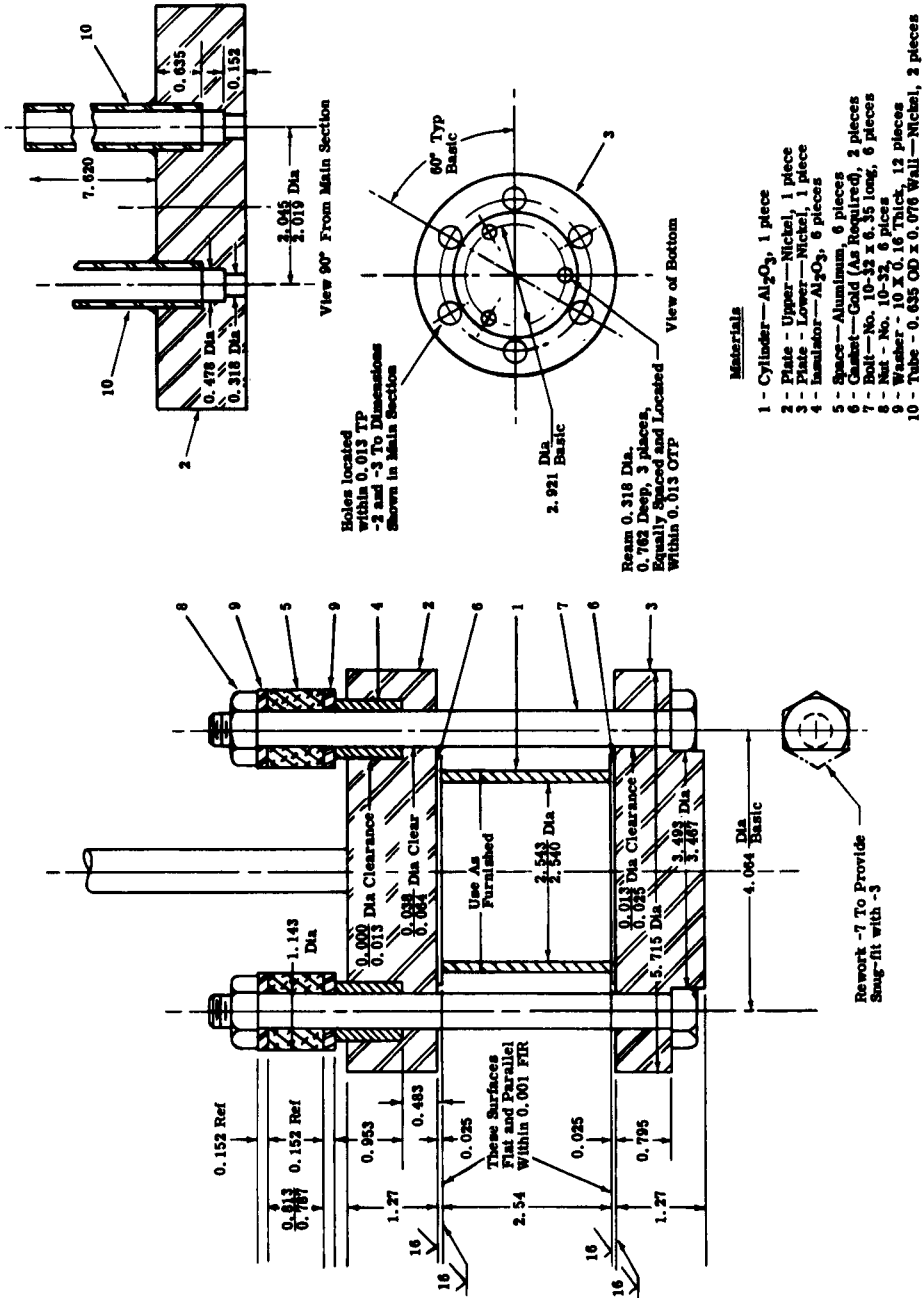


Figure 14. Detail of Conductivity Cell

CONDUCTIVITY CELL

A detail drawing of the cell is shown in Figure 14. The completed cell is shown in Figure 15. This cell was designed to determine the compatibility of ceramic samples in electrolyte as a function of time, and to determine the expected electrical performance of various matrix configurations (porosity, tortuosity, etc). Gold electrode surfaces were used—a tightly fitting sample disk is pressed into the bottom of the dense alumina cylinder. Vacuum-dried electrolyte is fed from one tube at the top, while argon flushing gas is bled out through the vent until the cell is completely filled. The seal depends on the dense cylinder coining into the soft gold electrode. A slight head of electrolyte ensures complete saturation of the disk specimen. Construction of the main cell body and tubes is of electrolyte-resistant nickel. The external circuit is connected to the nickel members, and resistances are read from gold electrode leads swaged directly into the gold electrodes. This provides a "four leads" system.

A secondary aspect of the cell design is to use aluminum shims having greater thermal expansion than the stainless steel bolts. The design is set up to keep a constant load on the sealing edges throughout cell heat-up. As modifications are indicated through future use, this type of compensating load could be adapted to eventual liquid metal cell unit design.

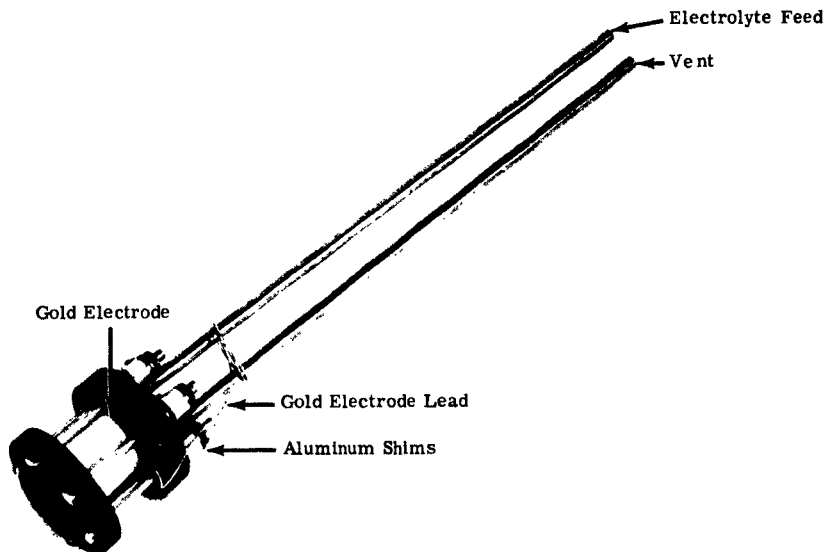


Figure 15. Fabricated Conductivity Cell

IV. EXPERIMENTAL RESULTS

Experimental results are discussed by Task Number as shown in the Time-Phased Chart, Figure 16. Following the discussion of task results is an additional paragraph on a cell performance measurement which was carried out.

NASA MATRIX PROGRAM (TASKS 1, 2, AND 3)

Seal and conductivity studies have progressed during this quarter, and cell studies are awaiting new paste formulations. Results are described in the first quarterly technical progress report on NASA Contract NASw-476 which is included as an appendix to this report.

GENERAL MOTORS MATRIX PROGRAM

Task 4--Seal Development

Any compressive-type seal for a liquid metal cell would consist of some combination of the following seal categories:

- Porous ceramic-to-metal
- Dense ceramic-to-metal
- Porous ceramic-to-dense ceramic

Porous ceramic-to-metal seal--A successful 50-hour test of a porous ceramic-to-metal seal was reported in Reference 8.

Dense ceramic-to-metal seal--An A-402 dense alumina ring was used after being ground and lapped flat and smooth to an RMS finish of 10. Maximum variation in flatness was 0.00035 cm. The sealing test cell (described in Section III, Apparatus) was loaded to 1050 kg/cm². A low (3 mol percent) potassium amalgam was added and a static head of 100 mm Hg (including inert gas cover) was maintained for a period of 50 hours. No leaks were encountered by visual observation. In addition, a leveling device was used to determine that no drop in level of amalgam within the standpipes occurred, which indicated that there was no leakage from the cell. Figure 17 shows the cell halves after test and indicates that a slight seepage (dark area on rim) of amalgam occurred but never reached the leak stage. Figures 18 and 19 show both sides of the dense ceramic insulator.



Dense ceramic-porous ceramic-metal seal—The same seal test cell was used for this experiment—only the configuration in this test was, from the bottom up, (1) lower cell half, (2) dense A-402 insulator, (3) ring, (4) matrix sandwich consisting of two pieces of porous alumina thinned out in the center portion, as shown in the photos, (5) dense ring, and (6) upper cell half. For this test one side of each dense ring was ribbed concentrically (Figures 20 and 21) to increase the unit loading on the metal cell half and, consequently, coin the dense ceramic into the metal. Two different unit loadings were tested by machining more ribs into one gasket than were designed into the second. Figure 20 derives the highest unit load, and Figure 21 yields a somewhat lower unit loading. The cell boundary is evident in both photos. Coin marks on the cell halves can be seen in Figures 22 and 23. The smooth sides of the dense gaskets were used to load against the porous matrix halves as shown in Figures 24 and 25. No leaks are evident. The sides of the porous matrix halves that faced against one another are shown in Figure 26. The 50-hour test, run as before with low potassium amalgam, was successful.

Owing to the success of these sealing measures, further work was done with a flow-type cell in its final configuration, with electrolyte flow provided. These tests are reported under Task 10.

Task 5—Conductivity Study

The completed cell (Figure 15) is being readied for initial tests.

Task 6—Cell Tests

A simple cell of approximately 10-cm² electrode area is being designed. Testing is scheduled to start in June.

AIR FORCE PROGRAM

Task 8—Preliminary Materials Studies of Porous Ceramic Materials, Compressive Tests

The goal of this task is twofold: (1) to determine the strength properties of ceramic materials—porous and dense—necessary to effect a seal, and (2) to investigate ceramic-electrolyte compatibility of new materials by determining changes in compressive strength as a function of time. The first goal has been met for the LM-833 magnesia material, which will most likely be used for a matrix for this project. However, it is emphasized that investigations of this nature will continue on new materials.



LEGEND: (X) TASK NUMBER
 ▽ MAJOR MILESTONE

FORM 2101 6/56

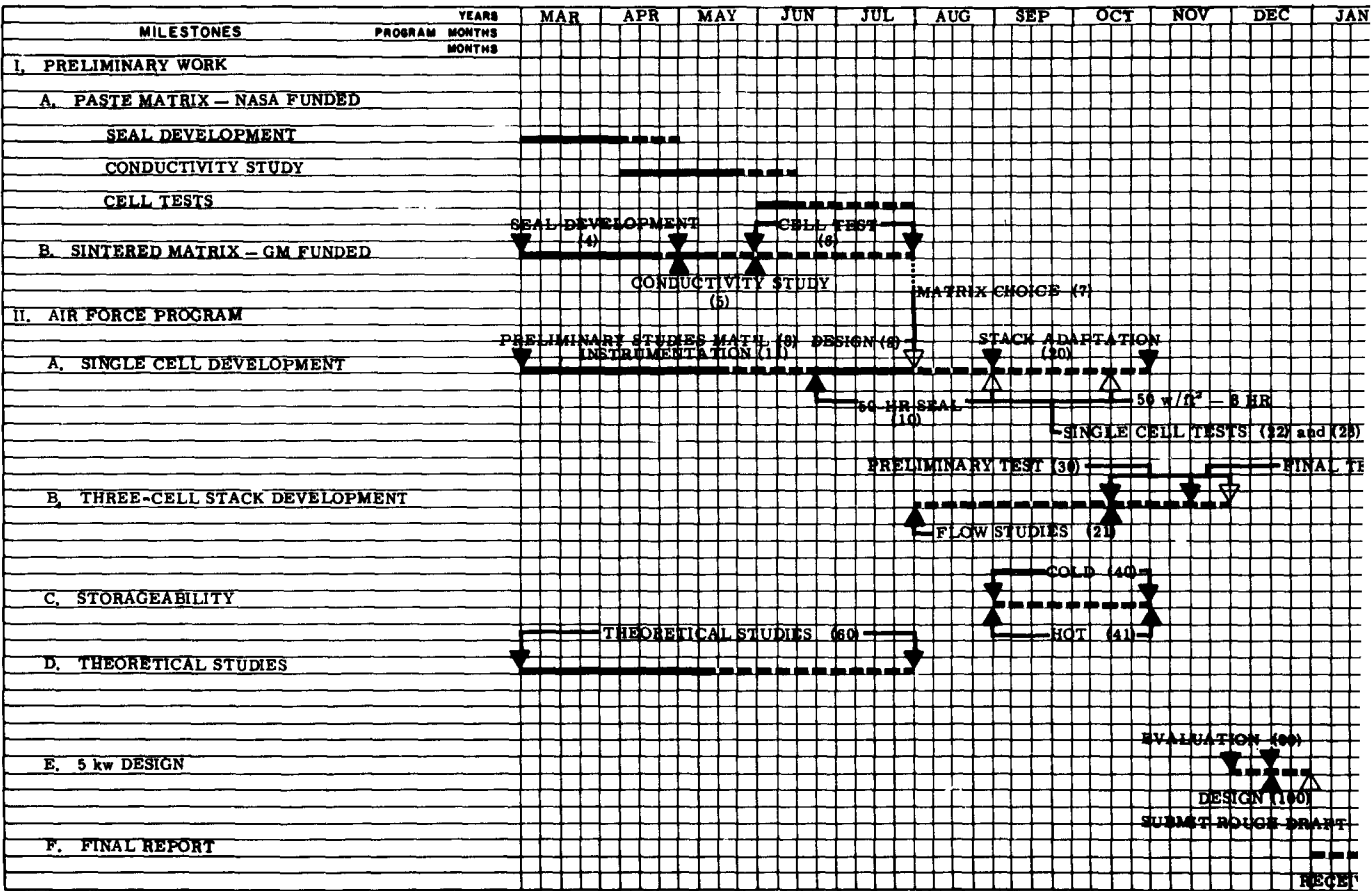


Figure 16. Time-Phased Chart



R
TONE

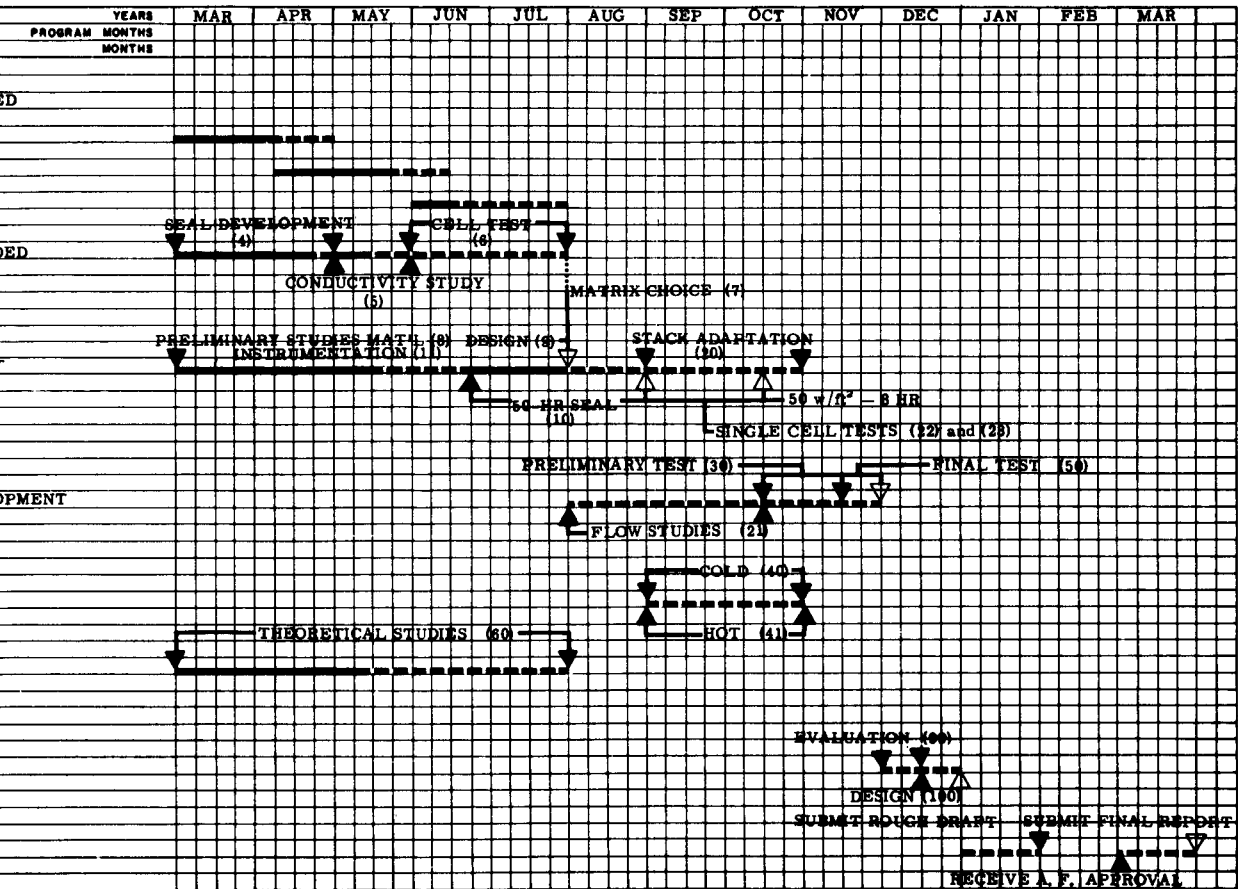


Figure 16. Time-Phased Chart

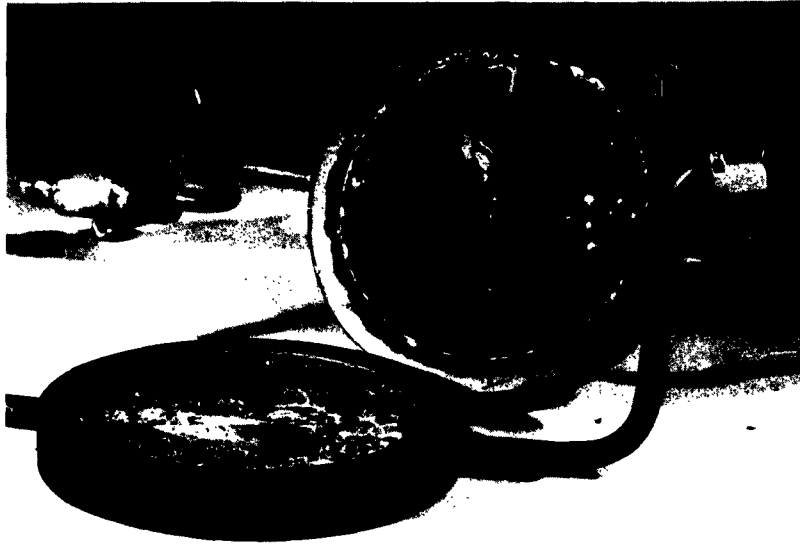


Figure 17. Dense Ceramic-Metal Seal Test

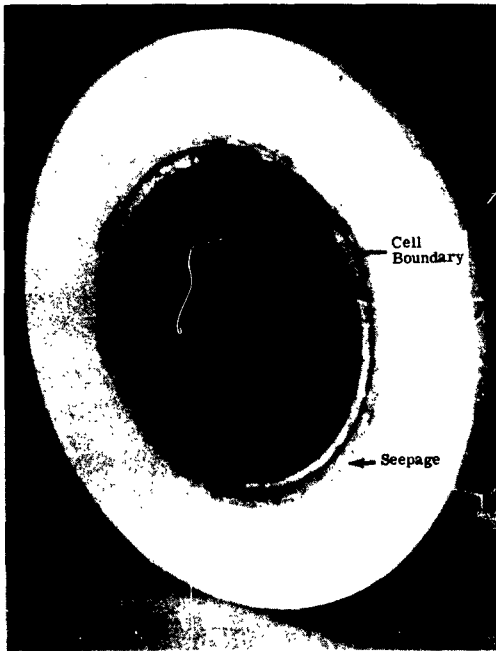


Figure 18. Ceramic Insulators from Seal Test

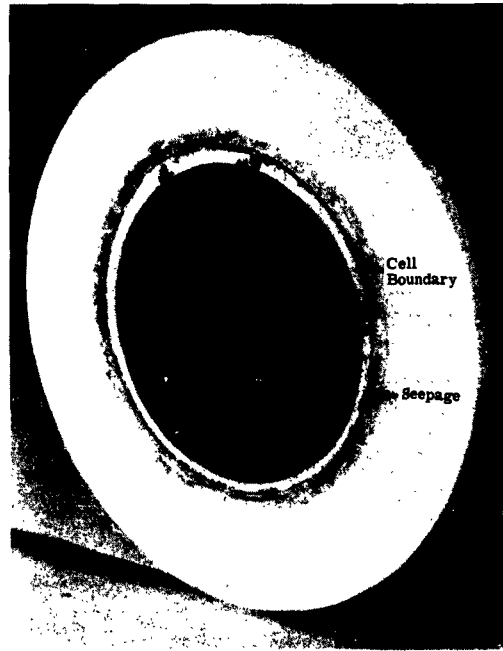


Figure 19. Ceramic Insulators from Seal Test

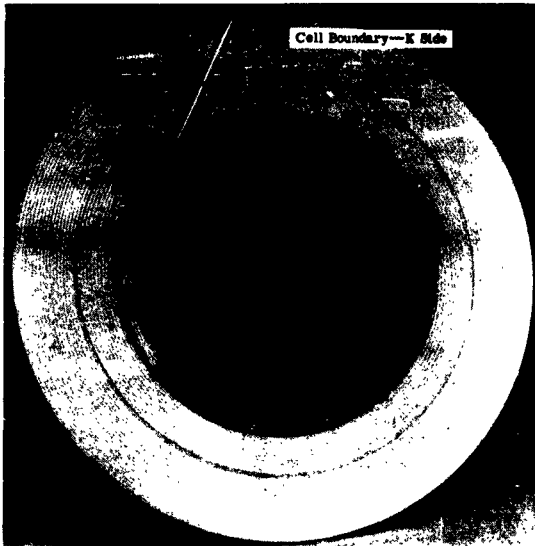


Figure 20. Dense Ceramic-Porous Ceramic-Metal Seal Test—High Unit Load Insulator

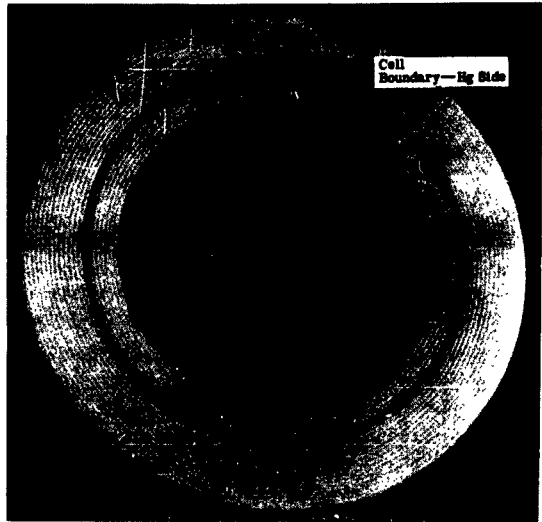


Figure 21. Dense Ceramic-Porous Ceramic-Metal Seal Test—Lower Unit Load Insulator

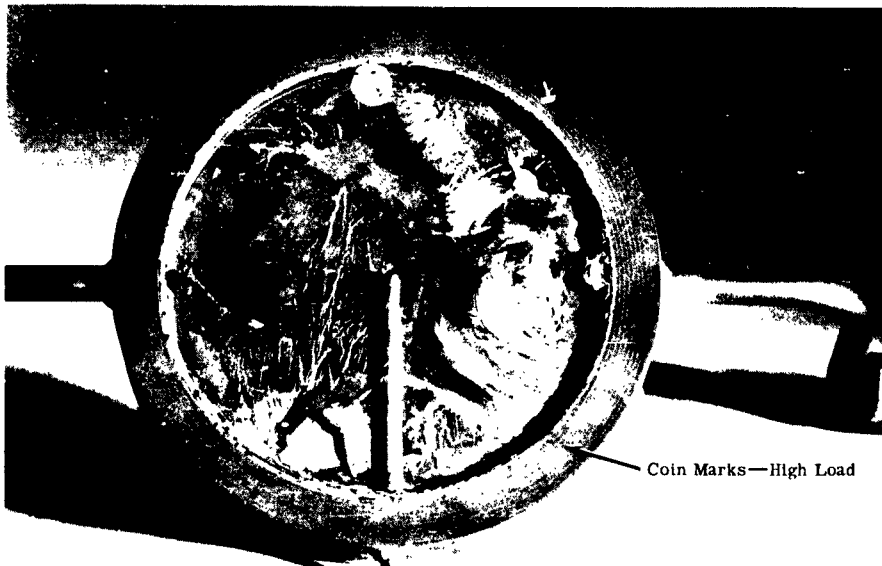


Figure 22. Dense Ceramic-Porous Ceramic-Metal Seal Test—Upper Cell Half



Figure 23. Dense Ceramic-Porous Ceramic-Metal Seal Test—Lower Cell Half

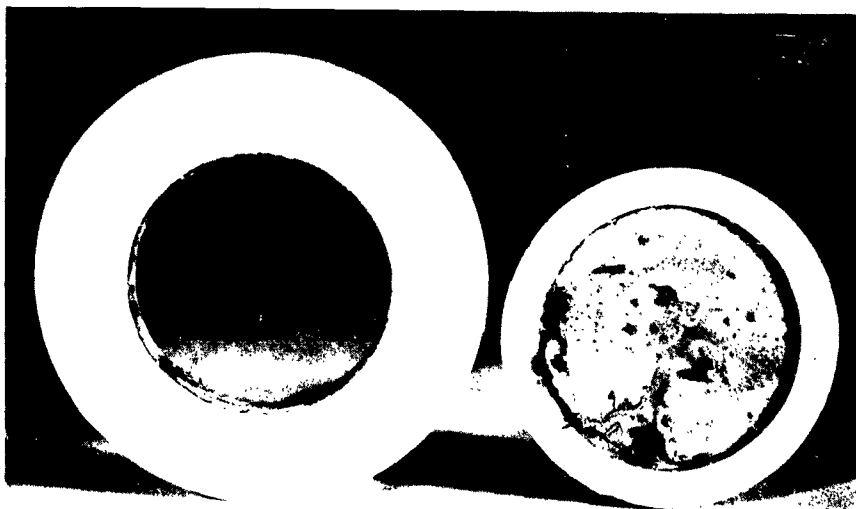


Figure 24. Dense Ceramic-Insulator and Matrix Half

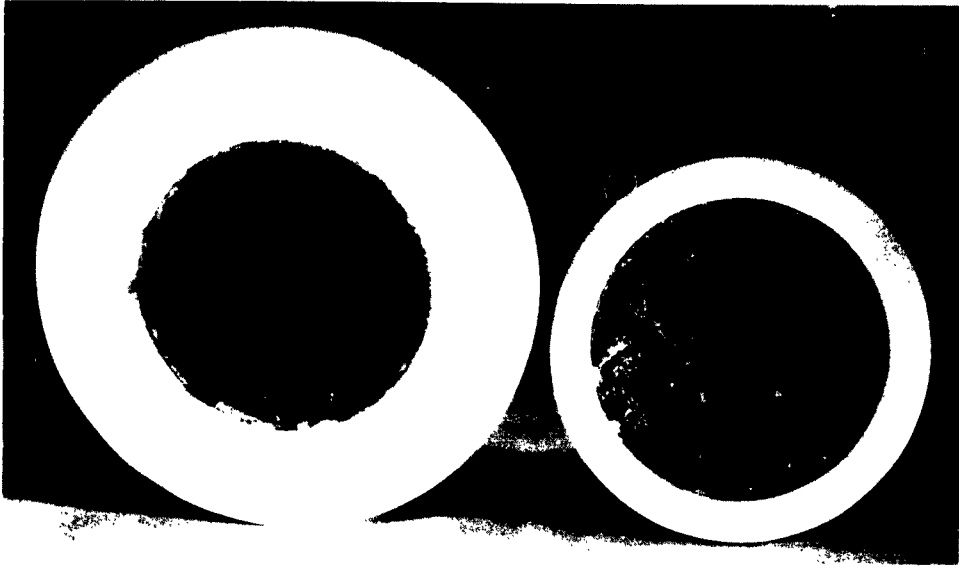


Figure 25. Dense Ceramic-Insulator and Matrix Half

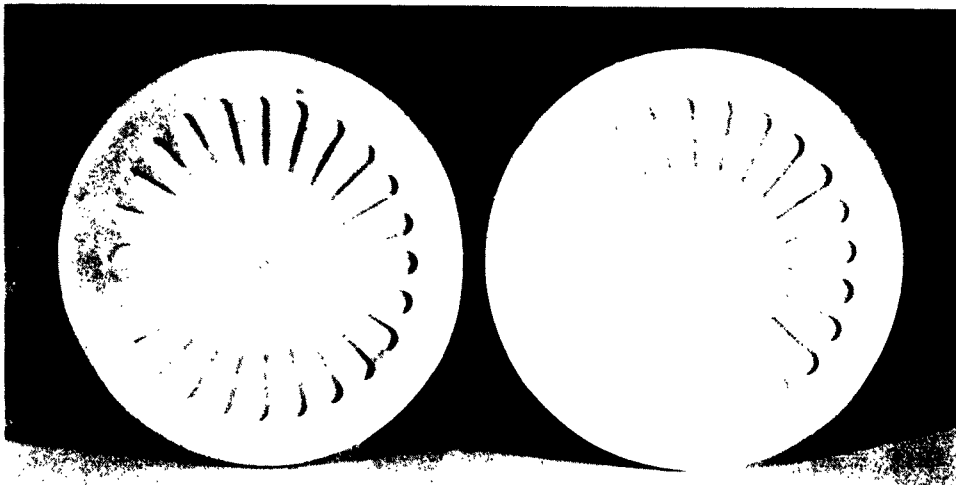


Figure 26. Dense Ceramic-Matrix Halves

The first year's program determined the stresses to which test ceramics could be loaded, and successful seals have been applied to the LM material. One further point of question was the effect of thickness on compressive strength. Accordingly, a test series was run on samples of LM-833 of varying thickness to determine any correlations. A view of the laboratory setup for measuring compressive strengths is shown in Figure 27. In the center is the hydraulic press which, acting through a hardened steel ram, exerts the load on the sample held within the furnace. The furnace contains a nickel-plated pot (with argon feed for inert atmosphere) which has a flexible nickel foil cover, thus allowing the application of force to samples which have been impregnated with electrolyte contained in the pot. A side arm (not shown) on the hydraulic ram actuates a linear potentiometer to indicate the strain of the sample. At the right of Figure 27 is an x-y recorder which indicates stress-strain relationships. A Blackhawk electric hydraulic pump was used to drive the hydraulic press. Ceramic samples were 1.9×1.9 cm square. The loading ram had an area of 1.265 cm^2 and the hydraulic press had an area

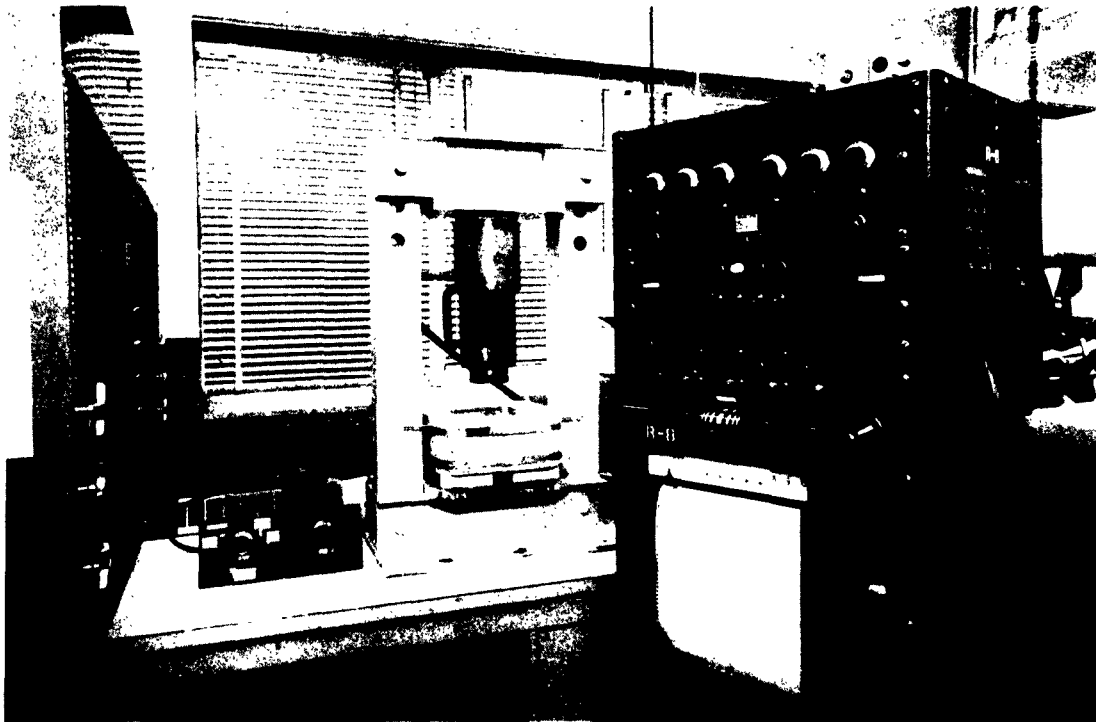


Figure 27. Compressive Testing Equipment



of 71.2 cm^2 . Thus, the sample stress was 56.3 times the pressure output of the hydraulic pump. Unimpregnated samples were brought to temperature (573°K), positioned in a hardened steel cup, and loaded to the yield point. Impregnated samples were impregnated according to standard vacuum techniques, held under the electrolyte in the closed, inerted pot for 16 hours, and then tested while still in the inert atmosphere.

Mean values of the dry samples indicated the following trend:

<u>Thickness (cm)</u>	<u>Compressive Strength (kg/cm^2)</u>
0.15	2680
0.25	2250
0.35	2130
0.47	1770

Averaging all samples of LM material run during last year's program and the present program yields the curve shown in Figure 28. It is reasonable to assume that as thickness decreases toward the presence of a monoparticulate layer, the compressive strength would rise to the value of the dense sintered magnesia.

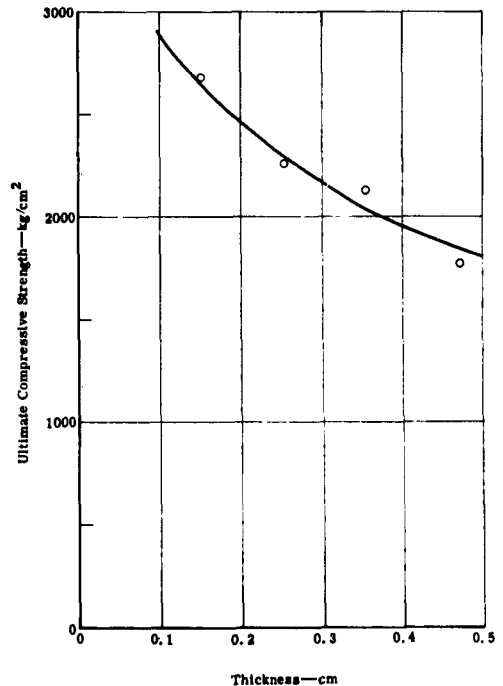


Figure 28. Thickness vs Ultimate Compressive Strength for LM-833 Magnesia

A compressive strength vs time test was conducted on the three ceramic materials at hand--- LM-833 magnesia, M magnesia, and L-Spinel. Strengths were determined unimpregnated at 573°K. Samples were then immersed in previously dried electrolyte and strengths were measured after immersion for one day and seven days. Results are given in Table VIII.

TABLE VIII
Compressive Strengths of Porous Ceramics vs Time in Electrolyte

(Sample Size: $1.9 \times 1.9 \times 0.25$ cm)

<u>Material</u>	<u>Time of Immersion (hr)</u>	<u>Average Compressive Strength (kg/cm²)</u>
LM-833 magnesia	0	2799
	22	2803
	168	2218
M magnesia	0	431
	22	309
	168	270
L-Spinel	0	1815
	22	695
	168	789

A statistical analysis showed significant effects on the M and L materials. There was no significant difference in the LM-833 material with time. Difference in initial values are not critical since the load applied to effect a seal can be adjusted to the strength of the material. However, changes within a material as a function of time indicate chemical attack.

Task 9---Preliminary Design Studies, Matrix Burst Test

The test was run in the following manner:

1. A lucite replica of a liquid metal cell of 7.62-cm electrode diameter was used as a test bed.
2. Samples of differing matrix design (described in Section III, Apparatus) were clamped into the cell, and the lower chamber was filled with mercury.



3. The filling tube was blocked off with a quick release clamp and a head of mercury was built up on the fill side.
4. The clamp was released and the matrix observed through the top of the cell to see if breakage occurred.
5. The operation was repeated at higher and higher heads of mercury until breakage occurred. The breakage pattern and bursting head were duly noted.

LA-830 alumina ceramics were used to conserve LM-833 materials because their strengths are similar.⁸ Results are presented in Table IX.

TABLE IX
Bursting Strengths of Matrix Designs

<u>Configuration</u>	<u>Electrical Cross Section (cm)</u>	<u>Impact Load (cm Hg)</u>	
		<u>No Break</u>	<u>Break</u>
Star	0.099	25	30
	0.130	30	40
	0.165	50	60
	0.168	50	60
7.62-cm Radius	0.064	7	10
	0.097	25	30
	0.140	39	45
	0.175	55	65
5 Ribs—7.62-cm Radius	0.117	35	40
8 Ribs—7.62-cm Radius	0.119	50	60

Note: "Break" and "No Break" refer to the head at which the matrix burst and the last head applied before burst occurred.

Figures 29 and 30 indicate break patterns typical of the star matrix designs. Figure 31 shows how a radiused sample ruptured, and Figures 32 and 33 are typical of ribbed designs. Figure 34 shows results plotted on rectilinear coordinates. The eight-rib sample is the only one which indicates significantly higher strength-to-thickness ratio. In order to estimate performance possibilities of the LM materials, two intersecting lines were added to Figure 34. The vertical line at 0.80-cm average thickness or electrical cross section is added to indicate the maximum thickness of half a matrix sandwich which will yield the power density required for this contract. The horizontal line at 20-cm Hg impact head represents double the maximum head which might be expected in the line surge involved in feeding reactants to the liquid metal cell. The intersection of these two lines has therefore been set as an initial goal in mechanical strength-electrical performance optimization. Present materials and design closely approach this goal.

A new series of samples is being prepared to check various designs in the 0.080-cm thickness regime.

Exact formulas for finding the bending moments of flat plates supported along their edges and subjected to stresses created by pressure on their surfaces have not been determined. The formulas given by different authorities are founded on assumptions and, therefore, are approximations only.

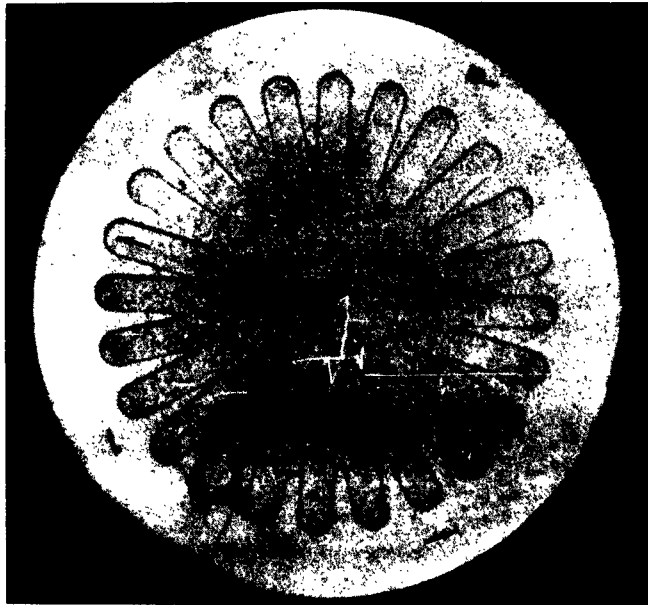


Figure 29. Top Side of Ruptured Star Matrix



Figure 30. Bottom Side of Ruptured Star Matrix



Figure 31. Break Pattern of 7.62-cm Radius Matrix



Figure 32. Five-Rib Matrix Break



Figure 33. Eight-Rib Matrix Break

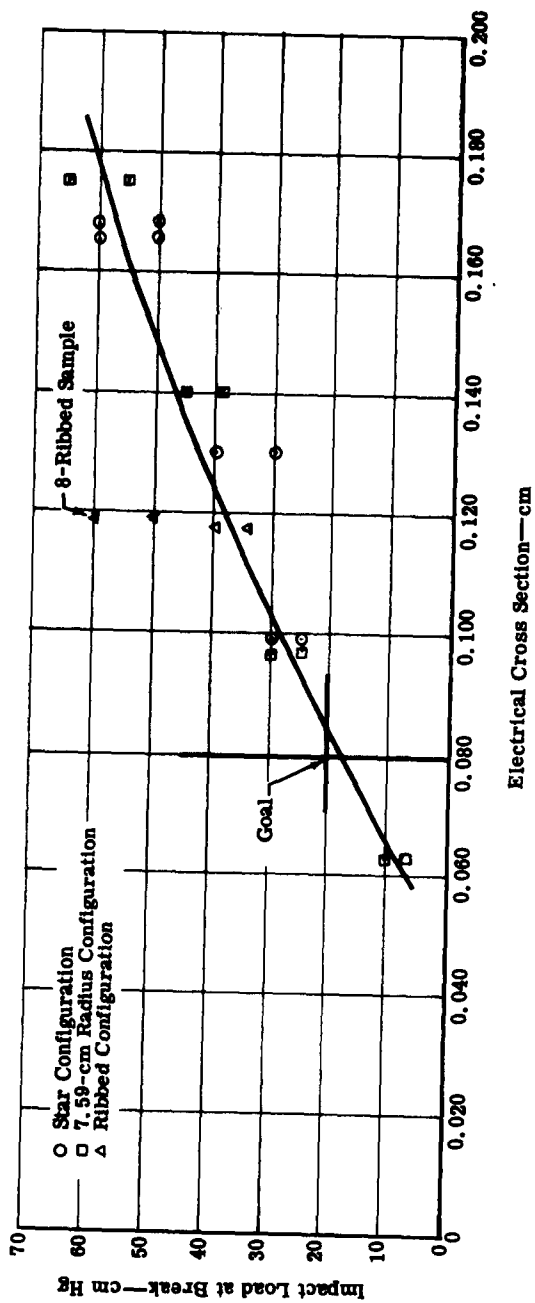


Figure 34. Matrix Impact Rupture Strength vs Electrical Cross Section

The stress on a circular flat plate, firmly secured all around the edge, with a uniformly distributed load over the unsupported area of the plate may be determined using Reuleaux's formula:

$$S = \frac{P_m R_m^2}{110 t^2} \quad (3)$$

where

- P_m = maximum pressure causing rupture (cm Hg)
- S = ultimate tensile stress (kg/cm²)
- t = thickness of plate (cm)
- R_m = radius of plate to the supporting edge (cm)

For the burst tests under consideration, the radius, R_m , was a constant at 3.81 cm. None of the samples were flat plates; however, for purposes of analysis, an average thickness of the plate has been taken. This has no basis in mechanical theory, but it does allow a calculation to be made which would be otherwise impossible, and this is the apparent thickness which must be used for electrochemical considerations.

A plot of load, P_m , vs the square of the thickness, t^2 , is shown in Figure 35. If the ultimate tensile stress were a constant with thickness, this graph would produce a straight line through the point (0,0). Previous tests of this material (LA-830) have shown that the ultimate compressive strength is not a constant with thickness as shown in Figure 28. If the ratio is taken of the ultimate tensile stress, as calculated from Equation (3) and the ultimate compressive stress from Figure 28, the following is found.

$$\text{Ultimate Tensile Stress (S)} = 0.112 \pm 0.012 \text{ Ultimate Compressive Strength}$$

This ratio compares favorably with other published data for ceramics (a comparison of tensile and compressive strength from Table II yields ratios of similar magnitude) and substantiates the validity of both the compressive strength and burst tests.

As may be seen in Figure 35, no significant difference exists for the various matrix configurations with the exception of the eight-rib configuration. It is possible that this configuration is actually stronger, or the basic material may have been stronger. It is not possible to tell from this test which is true. Additional tests will be run in an effort to produce the maximum rupture pressure for a given thickness.

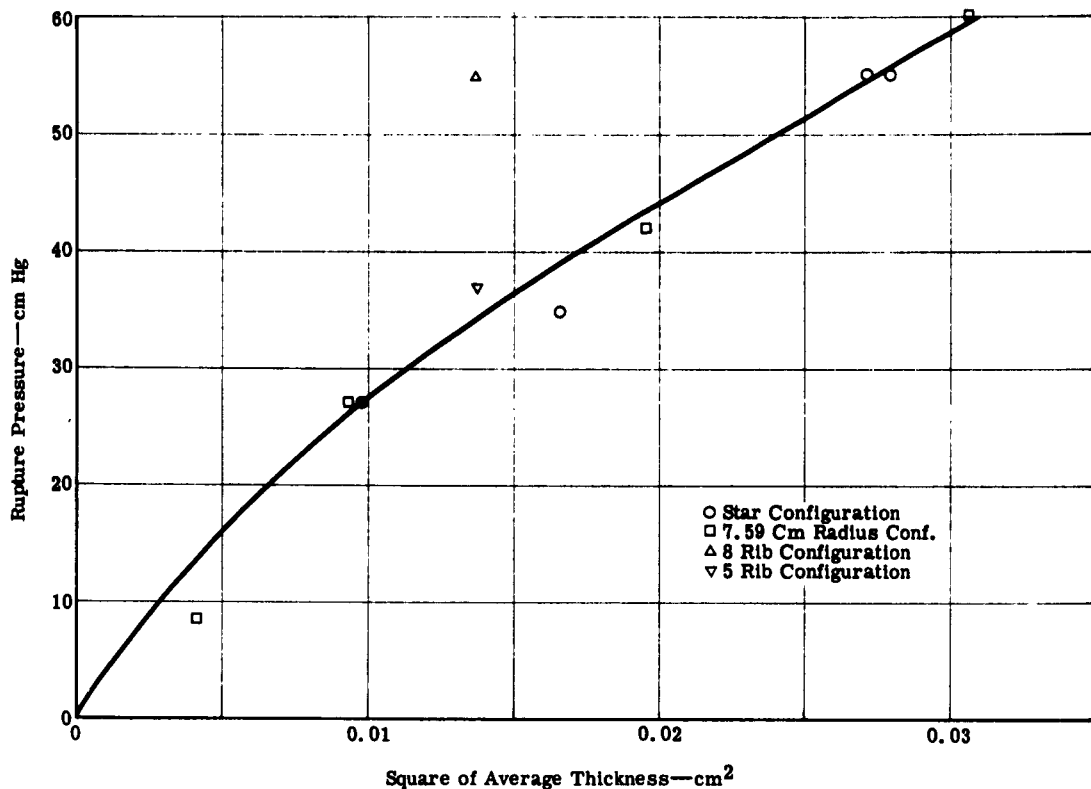


Figure 35. Rupture Pressure vs Square of Average Thickness

Task 10—Development of a Single Cell Seal

Results of seal tests carried out under Task 4 were successful; therefore, work was shifted to a seal for a flow-type cell configuration. Two tests were run to date—both using the Model III cell with potassium metal, electrolyte, and mercury.

Test 1

Test 1 conditions were as follows:

- Insulator—A-402 dense alumina (flat on matrix side, serrated on cell side)
- Matrix—LM-833 sandwich, 0.075-cm nominal thickness for each half

- Electrolyte Feed Ring—Spring wedge design (Figure 4), stainless steel

- Loading Information

 - Cell-Insulator—5,040 kg/cm² (apparent)

 - Insulator-Matrix—952 kg/cm²

 - Insulator-Electrolyte Ring—70 kg/cm²

The cell was tested at 553°K. A steady open circuit emf was established; no reactant leaks were detected by visual observation, and no change was evident in reactant levels. Cracks in the dense gaskets were discovered shortly after mechanical loading. A slight amount of electrolyte seepage occurred through the cracks, but no reactants were lost and no short circuits occurred. The open circuit emf indicates not only mechanical separation within the cell, but also matrix condition (such as internal shorts through the pores). It is believed that the cracks in the insulating gaskets were a result of the deflection induced in the metal cell halves under load. It was at this point that design of Model IV was initiated. Voltage continued steady for approximately three hours until a defective pressure regulator caused rupture of the ceramic diaphragms and shorted the cell.

Figure 36 is a view of the mercury chamber after test. Score marks of the ribbed gasket are visible at the inner and outer sealing surfaces. The three holes in the annulus between sealing surfaces represent leak detection stations. Figure 37 shows the mercury chamber with the dense insulator in place. Figures 38 and 39 are the potassium and mercury sides of the ruptured matrices, respectively, as they were held in the electrolyte feed ring—note the similarity in break pattern for similarly radiused samples in burst test. Figure 40 is the potassium chamber, and Figures 41 and 42 show the dense gaskets with induced cracks. It should be noted again that no reactant loss or short circuits resulted.

Since the redesigned cell (Model IV) could not be completed immediately, the Model III cell was set up for a rerun to develop further information.

Test 2

Redesigned insulators and electrolyte feed ring were used in this test in an attempt to alleviate insulator cracks. Test 2 conditions were as follows:

- Gaskets—A-402 alumina (flat on both sides)

- Matrix—Same as for Test 1

- Electrolyte Feed Ring—Metal labyrinth, Kovar (Figure 9)

- Loading

 - Cell Gasket—518 kg/cm²

 - Gasket-Matrix—458 kg/cm²

 - Gasket-Electrolyte Seal—3150 kg/cm² (apparent)

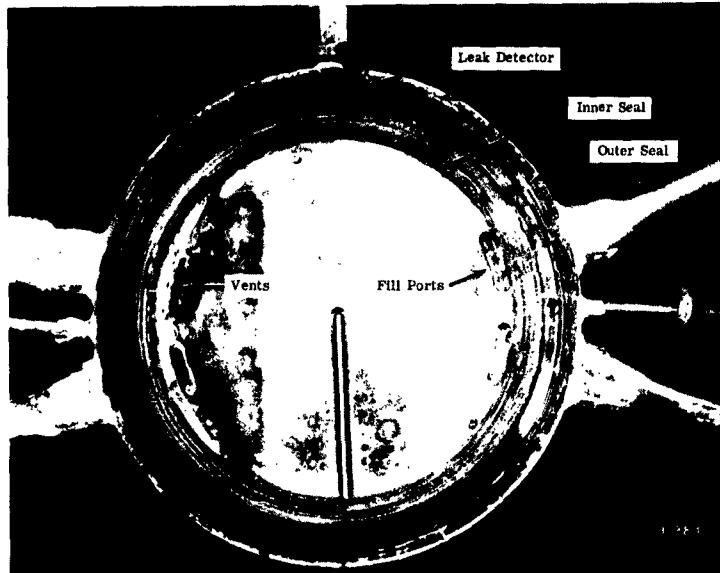


Figure 36. Test 1, Model III—Mercury Chamber

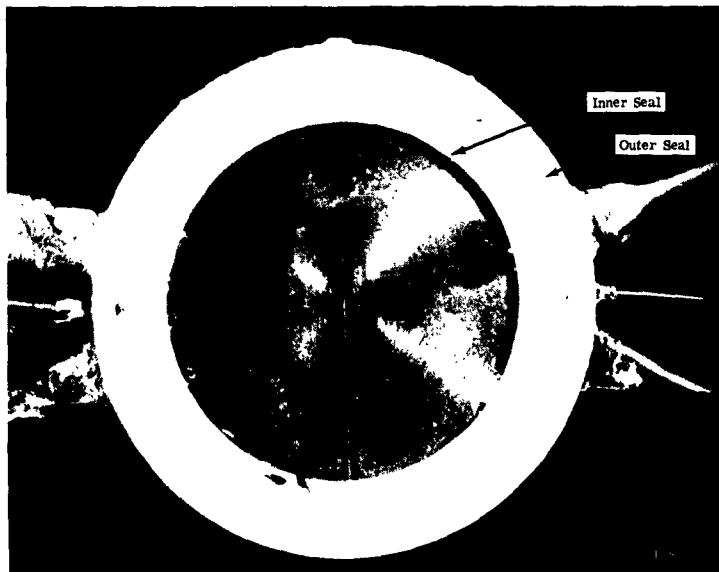


Figure 37. Test 1, Model III—Mercury Chamber with Insulator

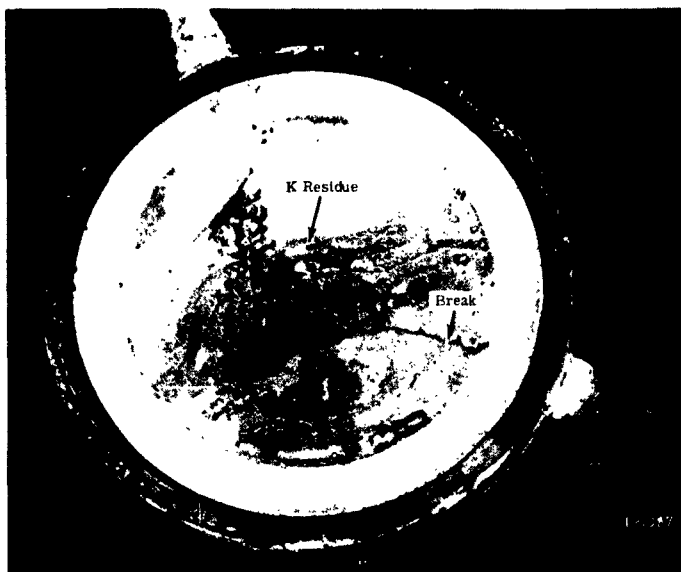


Figure 38. Test 1, Model III—Matrix and Feed Ring, Potassium Side



Figure 39. Test 1, Model III—Matrix and Feed Ring, Mercury Side

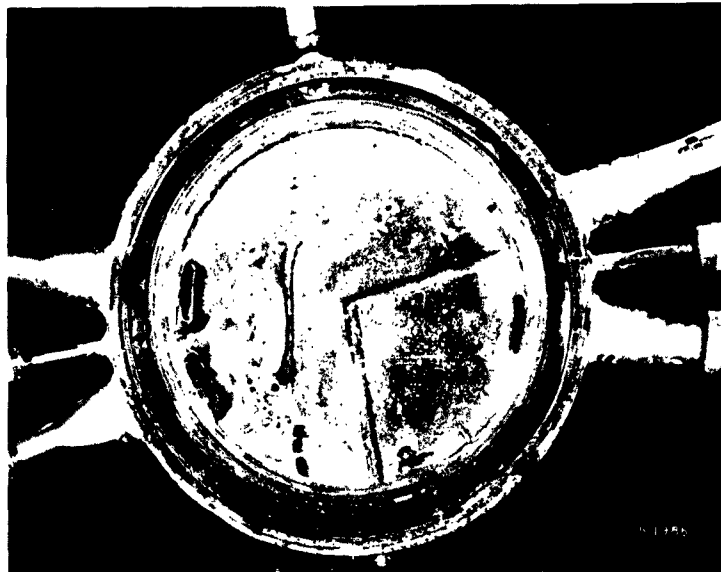


Figure 40. Test 1, Model III—Potassium Chamber

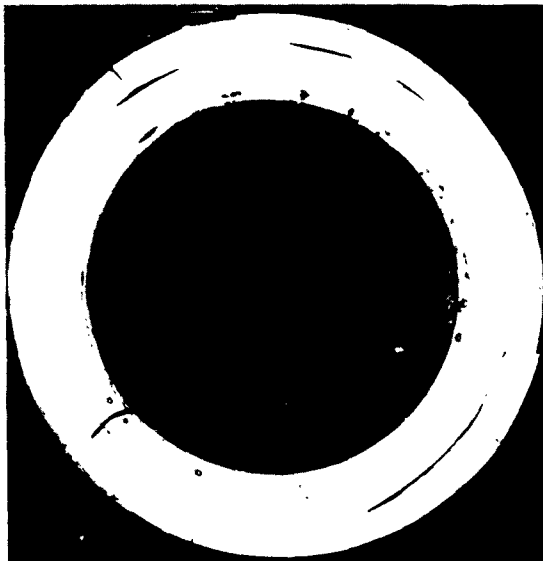


Figure 41. Test 1, Model III—Broken Insulator

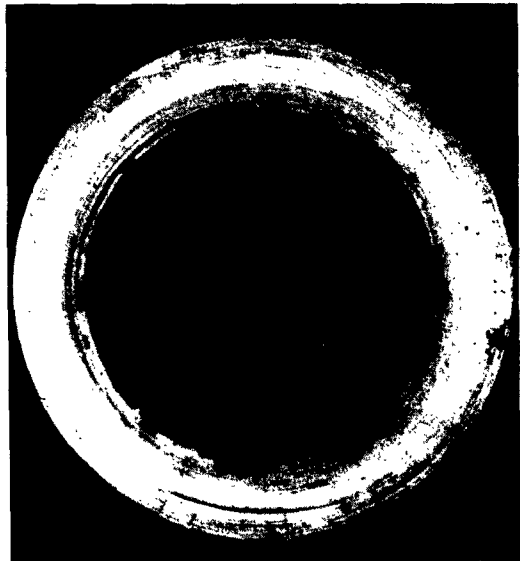


Figure 42. Test 1, Model III—Broken Insulator

Figure 43 is a view of the laboratory test setup as viewed outside the furnace. The cell was loaded with potassium, electrolyte, and mercury and was maintained at 573°K for 96 hours. Again, the ceramic insulators cracked during hydraulic loading but no reactant leaks were present. Electrolyte seepage occurred along the crack lines, as shown in Figure 44—a view of the cell within the furnace after test. The white material in the photo is electrolyte residue after seepage and cooling. A stable open circuit emf was maintained for the 96-hour period until attempts to put more mercury through the cathode led to matrix rupture. At that point, the emf was lost and the test was concluded. The test indicated that the seal was sufficient to maintain a cell for the required 50 hours but that electrolyte seepage should be eliminated. It is hoped that the Model IV cell will correct insulator cracking. Figure 45 shows the mercury chamber after test, with electrolyte filling the annulus between the inner and outer seal. Figure 46 is a view of the potassium chamber—atmospheric water is already acting on the potassium metal as evidenced by bubbles near thermocouple well. Figures 47 and 48 are views of the matrix, insulator, and electrolyte feed ring of the potassium and mercury sides, respectively. The failure points in the two matrix halves were back to back and similarly shaped. The high mark for mercury level is indicated in the photo. The mercury chamber was not completely filled because a thicker insulator had been used for this test and, consequently, overflow occurred at a relatively lower level.

Task 11—Instrumentation

The heat balance flowmeter shown in Figure 49 was tested to determine the feasibility of using a hot mercury input. Previous work with cold mercury is reported in Reference 8. Results indicated that with an input temperature of 373°K and flow rates of 5 cm³/min (measured at 273°K), a 46° rise in temperature occurred. At 363°K input and 2 cm³/min, an 80° rise occurred.

These results will pave the way for possible use of a mercury still to provide a purified metal input to the three-cell stack and to use the flowmeter, in effect, as an in-line preheater.

Task 60—Theoretical Studies

Allison has developed a mathematical model of a counterflow liquid metal fuel cell.¹⁷ This model uses the boundary condition that the output voltage along the length of the cell is constant, although the driving potential will vary. The model segments the cell into a large number of separate cells and makes possible the calculation of the various quantities of interest in the counterflow fuel cell. Average properties of the moving fluid within each small segment are used.



Figure 43. Test 2, Model III—Test Setup

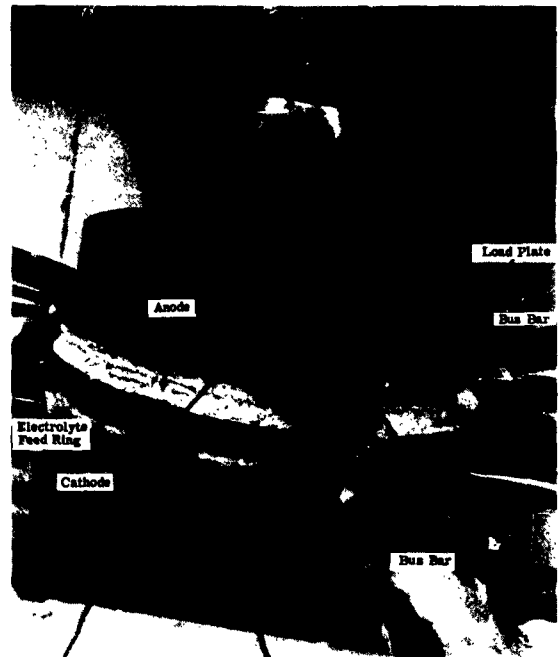


Figure 44. Test 2, Model III—Cell After Test



Figure 45. Test 2, Model III—Mercury Chambers

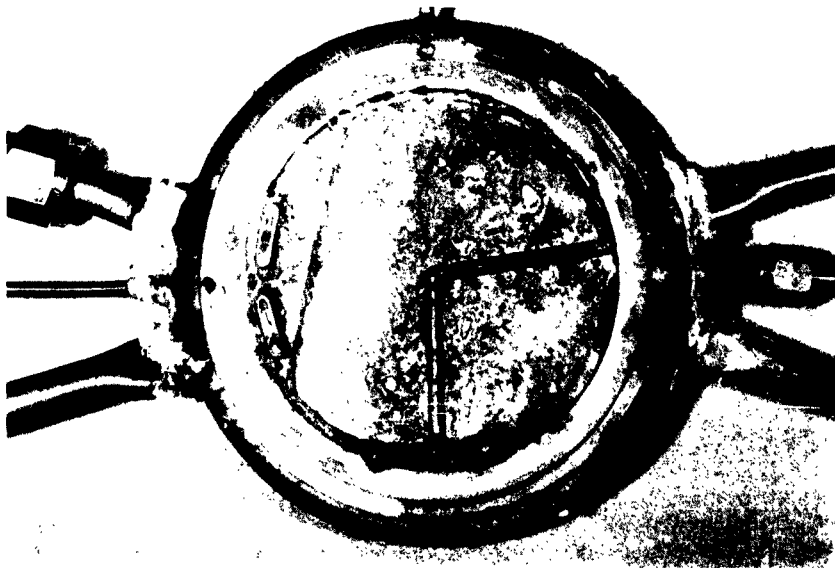


Figure 46. Test 2, Model III—Potassium Chamber

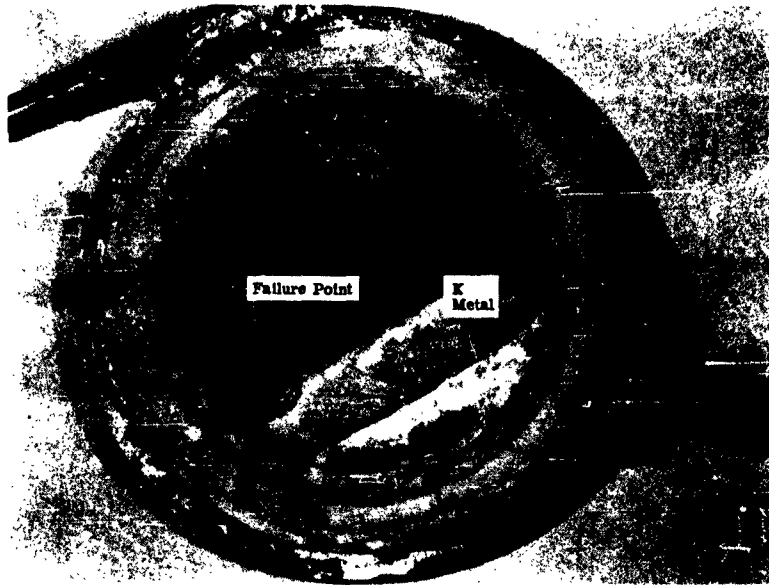


Figure 47. Test 2, Model III—Matrix and Feed Ring, Potassium Side

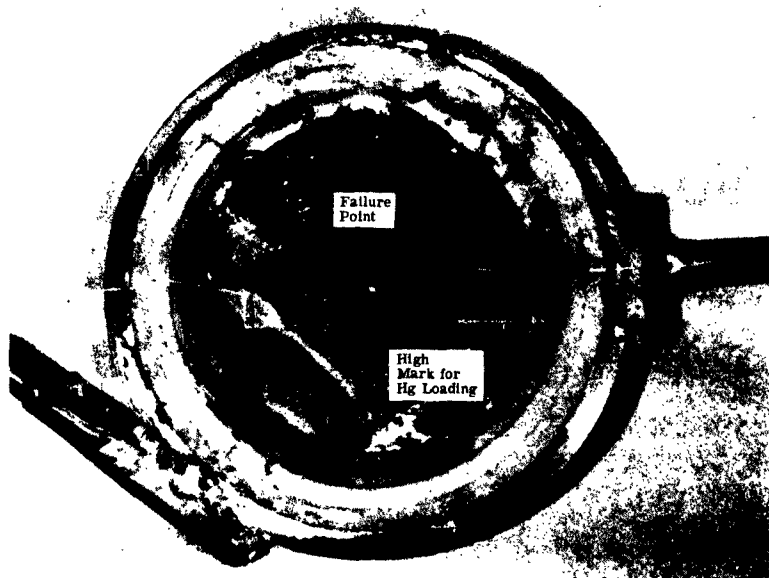


Figure 48. Test 2, Model III—Matrix and Feed Ring, Mercury Side

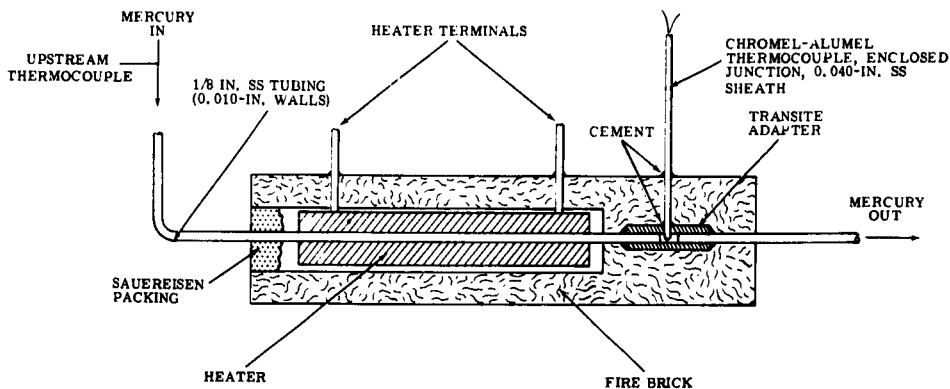


Figure 49. Heat Balance Flowmeter

Under this task requirement an advanced mathematical model will be developed to include partial differential equations for describing diffusion and laminar flow. The equations will be solved simultaneously for both anode and cathode, and parametric curves will be developed. Special emphasis will be placed on the role that low gravity fields would play in adaptation of the model.

Mathematical analogies are being drawn, and equations will be available during June.

Performance Check

During Test 2 of the Model III sealing test, it was decided to check the performance of the cell in the 70th hour of operation. The cell had no provision for continuous feed and was at that time suffering from clogged piping which prevented the entrance or exit of new reactants.



Electrical hookup yielded 7.5 amp, which for a mercury electrode area of 36 cm² was a current density of 195.8 amp/ft². Voltage of the cell was low 0.780 open circuit and 0.260 under load. This resulted in a power density of 50.91 watts/ft².

During the test period from 90 to 94 hours, cell resistance had increased somewhat but current densities of 91 to 117 amp/ft² were observed at low voltage.

The cell was then charged for a short period and voltage instability appeared. The cell was placed under load immediately, and the voltage again became stable. Cell resistance was higher from that point until failure was induced by mechanical manipulation. Results of intermittent testing are given in Table X. Since this was a static-type cell, there was no way to maintain open circuit voltage (except by recharge). The last column in Table X indicates performance which might be expected if it had been possible to maintain V_o* at 1.0 volt by reactant flow.

TABLE X
Performance of Model III Cell

Accumulated Hours	V _o Open Circuit Voltage (volt)	V _o * Recovery Voltage Immediately After Discharge (volt)	V _c Cell Voltage (volt)	I Current (amp)	R Cell Resistance (ohms)	i (amp/ft ²)	w (watts/ft ²)	w* (watts/ft ²)
70-1/4	0.780	0.680	0.260	7.5	0.056	195.8	50.91	116.6
90-3/4	0.630	0.550	0.070	4.0	0.120	104.4	7.31	54.4
91	0.620	0.550	0.060	3.8	0.129	99.2	5.95	50.6
92	0.617	0.540	0.100	4.5	0.098	117.5	11.75	66.6
	0.600	0.530	0.090	4.1	0.107	107.0	9.63	61.0
92-1/4	0.585	0.510	0.085	3.8	0.112	99.2	8.43	58.3
	0.570	0.505	0.080	3.6	0.118	94.0	7.52	55.3
92-1/2	0.560	0.495	0.080	3.5	0.1185	91.4	7.31	55.1
93-1/2	0.565	0.490	0.082	3.7	0.113	96.6	7.92	57.8
94	0.555	0.475	0.085	3.9	0.100	101.8	8.65	65.3

*For particular cell resistance if V_o = 1.0 volt and V_c = 0.5 volt

The results are fragmentary since this was a seal test. However, they do have a certain significance:

1. The performance goal of 50 watts/ft² was met in the 70th hour with lower voltage than would be present in a flowing cell.
2. The performance was achieved with a presently available matrix material and cell configuration.
3. The performance was achieved after a period of time which is beyond the contract requirement of 50 hours, which indicates no ruinous compatibility problem.
4. The watt/ft² at $\eta_c = 0.5$ (last column in Table X) indicates possible 50-watt/ft² performance through the 94th hour.

V. TECHNICAL POSITION

The time-phased chart shown in Figure 16 indicates that all tasks are on schedule with the exception of Tasks 1 through 5, which are about two weeks behind. This time will be made up during the second quarter—some conductivity results are already available from Test 2, as discussed in Section IV. Task 10 is 2-1/2 months ahead of schedule.

Test 2 yielded encouraging results pertaining to performance to be expected from future single cells, and effort must now go into repeating results with flow-type cells. Compatibility problems may not appear until well beyond the 50-hour period, if at all.

VI. WORK PLANNED FOR NEXT REPORT PERIOD

During the second quarter, it is planned to complete Tasks 1 through 11 and Task 60. Task 21 will be started during this period.

TASK 5

Conductivity vs time runs will be made on an LM-833 sample for a 30-day period. Conductivities will be monitored five times per week to evaluate that procedure. Then, concurrent samples of the various matrix materials at hand will be run. Conductivities and changes in conductivity as a result of incompatibilities will thus be determined.

TASK 6

Several small cells will be run to determine electrical properties in cell configuration. Effects of reversing the position of potassium and mercury will be investigated, as will the effect of preleaching the matrix. Based on these results, a matrix consistent with contractual requirements will be selected for the Air Force program (Task 7).

TASK 8

Compressive strengths will be measured vs time for the ceramic materials, and incompatibilities will be observed.

TASK 9

This task will be complete after checking several new designs, including the eight-rib in the 0.080-cm average thickness range.

TASK 10

Work will continue with the Model IV cell, or modifications thereof, until a 50-hour seal is obtained.

TASK 11

No further work is planned on this task until flow studies are initiated.



TASK 21

This is a study of flow problems associated with feeding streams evenly, accurately, with a good measure of control to the proposed stack for periods of 50 hours or more. A simulated stack will be run for 50 hours at cell temperature, using low potassium amalgam.

TASK 60

This task will be completed after development of parametric curves describing the performance of liquid metal cells under various operating conditions.

VII. REFERENCES

1. Weaver, R. D. and Shriver, E. L. The Fuel Cell Literature. Allison Division, General Motors Corporation, APS 10 (1959).
2. Yeager, E. in Proceedings of the 12th Annual Battery Research and Development Conference. Asbury Park, New Jersey (1958) pp 2-4.
3. Caple, W. G. and Shriver, E. L. Thermally Decomposable Inorganic Compounds. Allison Division, General Motors Corporation, ACS 1 (1960).
4. King, J. Jr., et al., in Energy Conversion for Space Power. New York, Academic Press, 1961, pp 387-410.
5. Henderson, R. E., Agruss, B., and Caple, W. G. Ibid., pp 411-423.
6. Laitinen, H. P. A., et al., in Journal of the Electro-Chemical Society. Vol 107 (1960) pp 546-555.
7. Parsons, R. Handbook of Electrochemical Constants. London, Butterworth's, 1959.
8. Agruss, B., Karas, H. R., and Decker, V. L. Design and Development of a Liquid Metal Fuel Cell. ASD-TDR 62-1045 (December 1962).
9. Liquid Metals Handbook. Atomic Energy Commission, Department of the Navy, Washington, D. C. (June 1950).
10. Ryshkewitch, E. Oxide Ceramics. New York, Academic Press, 1960.
11. Smith, T. P. Corrosion of Materials in Fused Hydroxides. Oak Ridge National Laboratories, Oak Ridge, Tennessee.
12. The Norton Company, Worcester, Massachusetts.
13. Whittemore, O. J. and Ault, N. N. in Journal of American Ceramic Society. Vol 39 (1956) p 443.
14. Morganite Incorporated, Long Island City, New York.



15. Benesi, H. A. , et al. , "Port Volumes of Solid Catalysts by Carbon Tetrachloride Absorption." Analytical Chemistry. Vol 27 (1955) p 1963.
16. The Carborundum Corporation, Refractories Division, Latrobe, Pennsylvania.
17. Systems Analysis of a Nuclear (Snap II) Liquid Metal Cell Space Power System. Allison Division, General Motors Corporation, EDR 3113 (5 December 1962) Appendix A.

APPENDIX

**First Quarterly Technical Progress Report on
Development and Testing of Electrolyte Matrix
Combinations for Mercury-Potassium Fuel Cell
(12 December 1962—12 March 1963)**

TABLE OF CONTENTS

<u>Section</u>	<u>Title</u>	<u>Page</u>
I	Introduction	A-1
II	Program Planning	A-3
III	First Quarter Progress	A-11
	Small DDC-Resistivity Cell Studies	A-11
	Conductivity Measurements of Coarse Grain Composites	A-14
	Analysis of Data	A-14
	Observations and Conclusions	A-15
	Compressive Strength Measurements of Coarse Grain Composites	A-26
	Development of a Preparation Technique for Fine Grain Composites	A-28
	Design of a Small LMC and Test Rig	A-29

LIST OF ILLUSTRATIONS

<u>Figure</u>	<u>Title</u>	<u>Page</u>
1	Symbolic Representation of Porous Media	A-3
2	Cold Press	A-4
3	Electrolyte Matrices Conductivity Apparatus	A-5
4	Conductivity Apparatus Circuit	A-6
5	Semilog Plot of Early Conductivity Data	A-6
6	Compressive Strength Data.	A-7
7	Compressive Strength Test Apparatus.	A-7
8	Theoretical Strength and Resistivity.	A-8
9	Extrapolation to Small Grain Sizes	A-8
10	Cell Resistivity Study.	A-10
11	Composite Electrolyte Study	A-10
12	Program Schedule	A-10
13	LMC Performance Characteristics	A-12
14	Schematic Diagram of DDC Used in Resistivity Studies	A-12
15	Plot of Data Obtained from Cell Resistivity Studies	A-13
16	Conductivity of 31/69 Unconsolidated Electrolyte Matrices.	A-16
17	Conductivity of 33/67 Unconsolidated Electrolyte Matrices.	A-16
18	Conductivity of 35/65 Unconsolidated Electrolyte Matrices.	A-16
19	Conductivity of 33/67 and 31/69 Unconsolidated Matrices to Show Density Effect.	A-16
20	Conductivity of 31/69, 33/67, and 34/66 Unconsolidated Matrices With 86.2% Theoretical Density.	A-23
21	Conductivity of 34/66 Unconsolidated Electrolyte Matrices.	A-24
22	Conductivity of 34/66 Unconsolidated Electrolyte Matrices.	A-24
23	Conductivity of 0.3-cm Unconsolidated Electrolyte Matrices	A-25
24	Test Equipment for First Small Unit	A-29
25	Small Cell Test Setup	A-31
26	Small Cell Assembly	A-32
27	Post Analysis of Small Cell	A-33

LIST OF TABLES

<u>Table</u>	<u>Title</u>	<u>Page</u>
I	Comparison of A-C Bridge Technique With Cell Performance (T = 300°C) . .	A-9
II	Specimen Identification	A-17
III	Specimen Data	A-18
IV	Ball Penetration Strength Test Results	A-27
V	Deformation Test Data	A-27

I. INTRODUCTION

This is the first quarterly technical progress report on development and testing of electrolyte matrix combinations for mercury-potassium fuel cell for the period 12 December 1962--12 March 1963. This work is being conducted under NASA Contract NASw-476.

Systems studies¹ of the liquid metal cell direct conversion unit have shown that cell performance must be improved in order to provide system weights lower than those of dynamic systems. Specifically, the resistivity-thickness product, γt_e , must approach 0.5 ohm-cm^2 . Tests of cells using a porous ceramic matrix of 1.5-mm thickness have shown this performance parameter to be approximately 2 ohm-cm^2 . Improvement of cell performance is expected by increasing matrix porosity and decreasing thickness to the limit of engineering development.

The approach under study in this contract is to use an unconsolidated ceramic-electrolyte composite matrix. This work was initiated previously with the successful development of a technique for the preparation of a 6μ average MgO particle size composite in the Allison Materials Research Laboratory. Early results of conductivity and strength studies are reported in EDR 3050.² It has been shown³ theoretically that the use of smaller particle sizes will bring about a considerable improvement in γt_e . Therefore, it is first necessary to devise techniques for employing small ($\sim 1\mu$) particle size composite matrices.

¹Systems Analysis of Nuclear (SNAP II) Liquid Metal Cell Space Power System, Allison Division, General Motors Corporation, Indianapolis, Indiana, EDR 3113 (5 December 1962), pp 19-23.

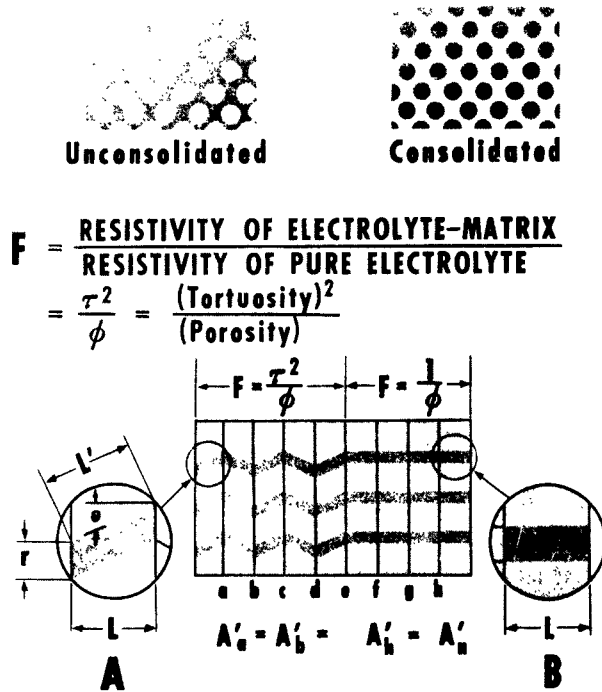
²Third Quarterly Technical Progress Report on Design and Development of a Liquid Metal Cell for Period 1 July--30 September 1962, Allison Division, General Motors Corporation, Indianapolis, Indiana, EDR 3050, Contract AF33(657)-7847 (12 October 1962), pp 8-12.

³Systems Analysis of Nuclear (SNAP II) Liquid Metal Cell Space Power System, Allison Division, General Motors Corporation, Indianapolis, Indiana, EDR 3113 (5 December 1962), Appendix G.

II. PROGRAM PLANNING

This section presents material aids devised during the initial phase of the program.

Figure 1 is a symbolic representation of porous media. The unconsolidated material is depicted by grains of solid material (light dots) in a liquid (dark background). The consolidated material is shown by a reversal of phases so that the solid material is bound together for greater strength. The liquid phase is thought to have connecting paths in the third dimension, although the picture does not show these connecting links.

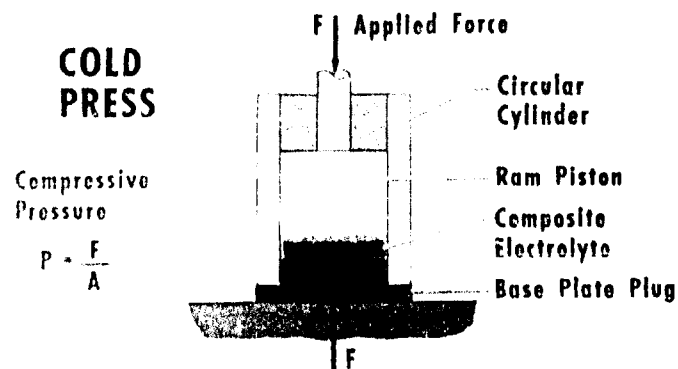


$$\tau = \text{Tortuosity} = \frac{1}{\cos \theta} = \frac{L'}{L} = 1.00 \text{ for Case B}$$

Figure 1. Symbolic Representation of Porous Media

For either the unconsolidated or the consolidated body, the liquid phase may carry an electronic or an ionic current according to some resistance which is a property of the liquid phase and the restriction caused by the configuration. Therefore, a formation factor (F) is defined as shown. Geometric considerations have shown that the formation factor may also be equated to the ratio of tortuosity squared to porosity. A two-dimensional tortuous path is shown for the practical case (A), where the path is not straight, and case (B), where the path angle, θ , is zero, tortuosity is unity, and the formation factor becomes proportional to the inverse of the porosity. Therefore, the tortuosity is an important term in the definition of a porous medium inasmuch as it measures the restrictions to flow in an otherwise highly porous body. No proposal is made to measure or test for tortuosity, but only to use the concept for a clearer understanding of the matrices mechanics.

Figure 2 shows the cold pressing technique along with a nine-step preparation technique for the 6μ (average) composite program. All steps are accomplished under an inert gas atmosphere, except the cold press operation.



Steps in the Preparation of the Composite Electrolyte

1. Mix ceramic powder with 50% Aqueous solution of electrolyte in proper ratio
2. Evaporate dry 120°C
3. Bake at 260°C for 30 Minutes
4. Vacuum dry 16 hours at 350°C
5. Cool and Grind to 20-mesh size
6. Ball Mill 2 to 3 hours
7. Sieve through a 100-mesh screen
8. Cold press to shape at 20,000 to 40,000 psi
9. Bake in vacuum at 350°C for 2 hours

Figure 2. Cold Press

To study the properties of these composites, two basic tests are performed---a conductivity test and certain strength tests. The conductivity measurements are carried out in a tube furnace as shown in Figure 3. The inset shows a composite specimen located within a ceramic retaining ring prior to heat-up and subsequent compression between the contact electrodes. Thermocouples and electrode lead wires pass from the furnace to external instruments and control equipment.

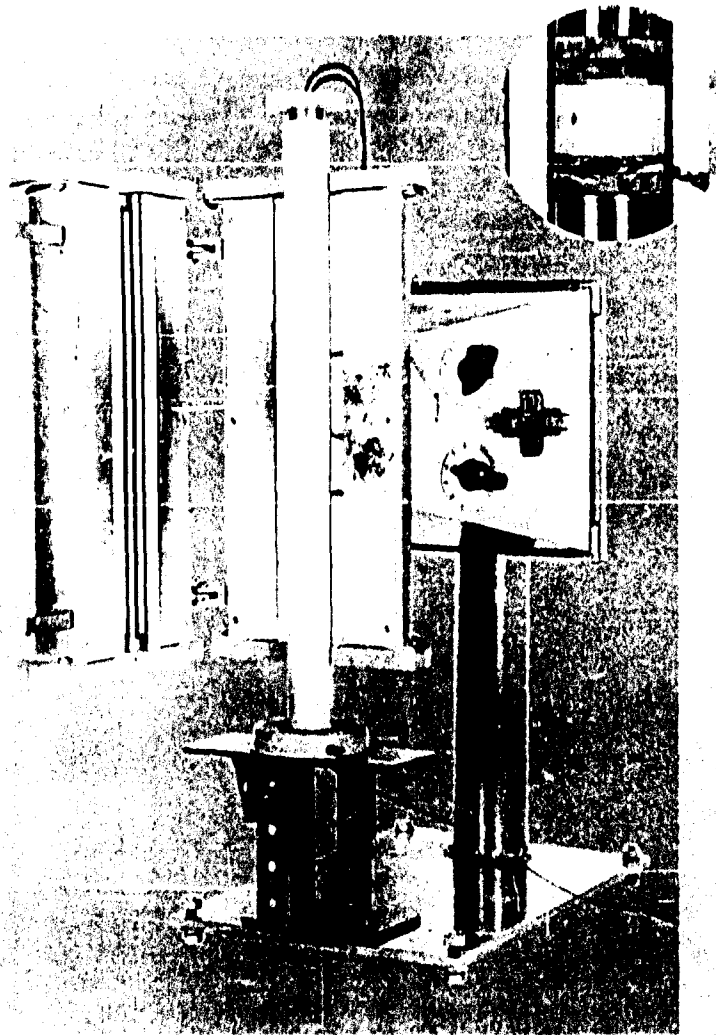


Figure 3. Electrolyte Matrices Conductivity Apparatus

Figure 4 is a schematic of the electrical measuring circuit. Salient features of this bridge are the Wagner Earth and variable capacitors for balancing the circuit prior to measurement of a specimen.

Early work with the 6μ composites, using limited data points, has been plotted on a semilog plot as Figure 5. Data from a pure electrolyte are shown to be considerably higher. This shows the effect of the formation factor (F) as mentioned in Figure 1. Percent theoretical density is shown as a variable. This reflects a preparation technique which is greatly affected by the cold press operation used in the process shown in Figure 2.

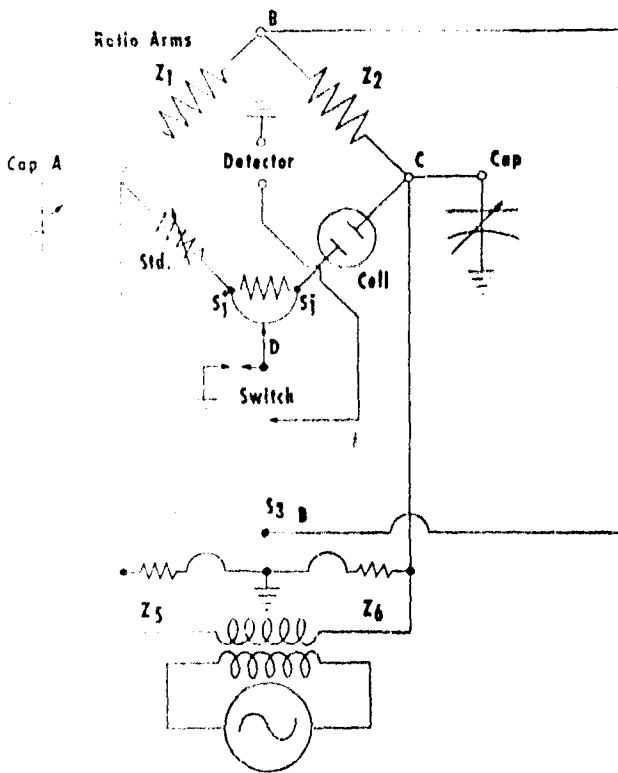


Figure 4. Conductivity Apparatus Circuit

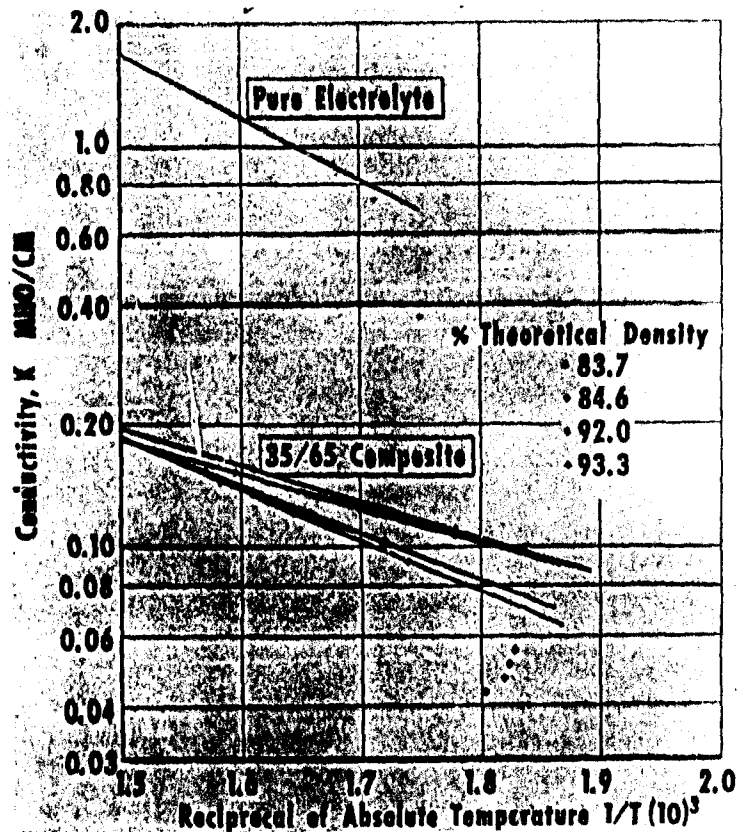
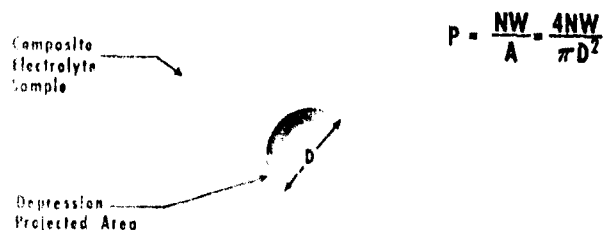


Figure 5. Semilog Plot of Early Conductivity Data

Strength data shown in Figure 6 are obtained from the apparatus shown in Figure 7. Results acquired from this technique are used to compare the relative strength of a specimen to that of another specimen. No correlation of this work is proposed to that of absolute strength measurement techniques, since the material under development is required to be quite plastic.

A theory is under development which may predict the absolute values of resistivity and strength from a knowledge of the composite composition and material properties. To date this work states that compressive strength is proportional to the ratio of the area of the nonwetting phase to the volume of the wetting phase.



$$P = \frac{NW}{A} = \frac{4NW}{\pi D^2}$$

Batch Designation	Percent Electrolyte	Percent Theoretical Density	Loading Time (Hours)	Load (Grams)	Relative Compressive Strength (PSI)
A	35	85	4	6	0.6
A	35	85	4	8	0.5
B	35	86	1	25	0.7
C	33	85	1	25	5.0
D	31	80	1	25	8.5
E	33	80	1	42	10.7
E	33	80	1	50	11.7
E	33	80	4	50	11.8

Figure 6. Compressive Strength Data

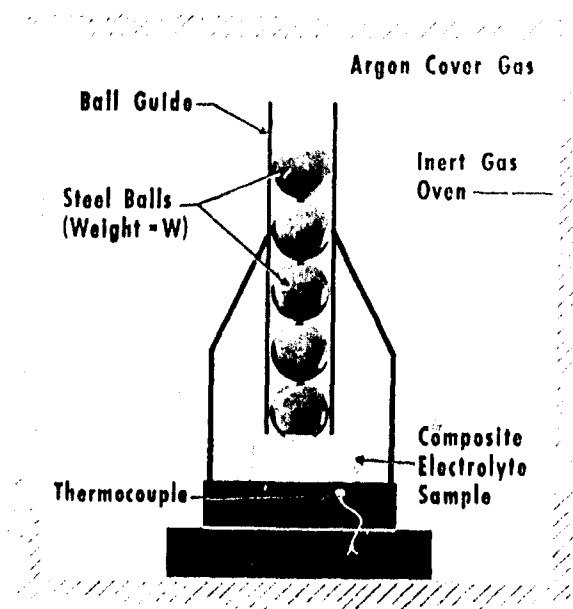
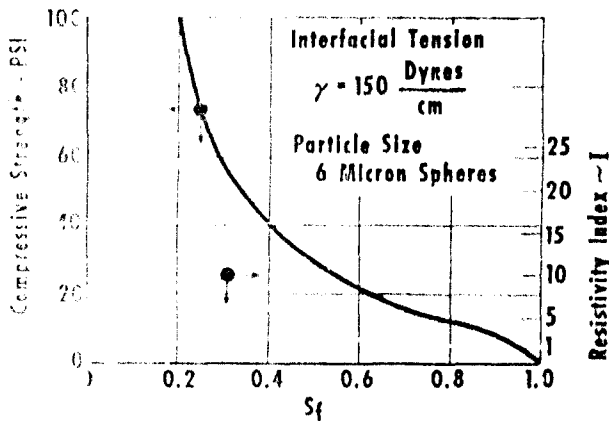


Figure 7. Compressive Strength Test Apparatus

The investigator has expanded this to the equations for compressive strength (A) and resistivity index (B) shown in Figure 8. The plot is for a composite made up of uniformly packed 6 μ spheres and an electrolyte with an average interfacial tension as found in the literature. Further progress on the development of this theory will be reported as it becomes available from Allison-funded independent research.

The primary usefulness of this work is shown in Figure 9. The compressive strength (P_c) has been compared for different grain sizes at the same saturation (S_f). Since the specific surface (S) is proportional to the inverse of a characteristic dimension (d) of the grains, the extrapolation to small grain sizes is inversely proportional to the size number (n) in micron units. The resistivity index (I) is unchanged since it is proportional to saturation. Figure 9 shows a trend to greater strengths at constant conductance for a smaller grain composite. Stated in another way, greater conductance should be gained for a given strength by the use of fine-grain ceramic composites. It is expected that grain shape, size distribution, and preparation technique will influence the final performance of any given average grain size composite.

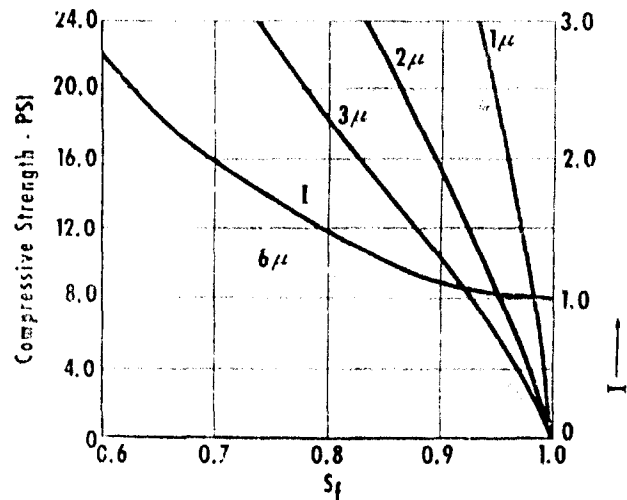


$$A \quad P_c = \gamma \cdot 1.2 \frac{S}{\phi} \frac{(1-S_f)^2}{S_f}$$

$$B \quad I = S_f^{-2}$$

FOR UNIFORMLY PACKED SPHERES

Figure 8. Theoretical Strength and Resistivity



$$P_c(n\mu) = P_c(6\mu) \frac{6}{n}$$

$$\text{from } \frac{S}{\phi} \propto \frac{1}{d}$$

Figure 9. Extrapolation to Small Grain Sizes

Conductivity measurements are made as a means toward selecting a composite. Strength tests are used for the same purpose, thereby reducing the number of electrochemical cell tests required for a program. Table I shows the comparison of a-c bridge measurements to cell performance values. The discrepancy is to be determined through a planned testing procedure.

TABLE I
Comparison of A-C Bridge Technique With Cell Performance
(T = 300°C)

<u>Configuration</u>	<u>Resistivity (ohm-cm)</u>		<u>Ratio</u> <u>Cell/Bridge</u>
	<u>A-C Bridge</u>	<u>Cell</u>	
Pure Electrolyte	1.59	3.3	2.08
Composite Electrolyte	7.1	14	1.97

Cell Resistivity Computed from Data by:

$$\gamma = R_c \left(\frac{A}{t} \right)$$

One possible linear relation which will explain the discrepancy is shown in Figure 10. The cell performance data point is shown to be displaced from that predicted by the resistivity computed from conductivity measurements. This first appears to give a higher value for electrolyte resistivity shown by the slope of the line passing through zero, but it may be displaced by an interfacial resistance which is not a function of electrolyte thickness.

Composite electrolyte studies will be carried out as depicted in Figure 11. This is considerably simplified, but it does reflect the need to establish a composite identity, such as saturation to optimize strength, conductivity, and, possibly, seal properties.

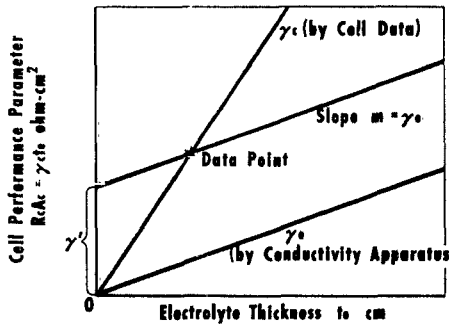
A program schedule was prepared to indicate the proposed progress of the program. Figure 12 reflects the three program phases indicated in the work statement.



Cell Resistance

$$R_{cA_c} = \gamma_c t_c = \gamma_c t_c + \gamma' l$$

where $\gamma' l$ is a Constant Interface Resistance ohm-cm²



Study will incorporate three controlled cells with electrolyte thickness, t_c as the only variable.

Figure 10. Cell Resistivity Study

- ◆ For each selected composite measurements of strength, density and conductivity will be made.
- ◆ Sealing properties will be studied to determine usefulness in an Engineering Design.
- ◆ Optimization will be made through the study of strength, conductivity, and sealing properties.

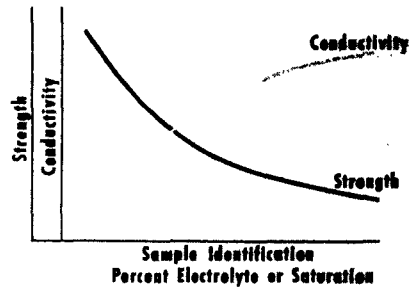


Figure 11. Composite Electrolyte Study

Activities	Program Months	D	J	F	M	A	M	J	J	A	S	O	N
Develop Paste Electrolyte Preparation Techniques													
6 μ Composite Compressive Strength Studies			█	█									
Develop 1 μ Composite Electrolyte			█	█									
Evaluate Composites													
Conductivity and Strength Testing (1 μ)			█	█	█								
Evaluate Composite in Small Cells				█	█	█							
Evaluate Test Results							█	█					
Final Cell Program													
Design Large Cells							█	█					
Fabricate Cells									█	█			
Test Cells									█	█			
Analysis and Final Report											█	█	█

Figure 12. Program Schedule

III. FIRST QUARTER PROGRESS

Progress has been made in the following areas: (1) small differential density cell (DDC)-resistivity cell studies; (2) conductivity measurements of coarse grain composites; (3) strength measurements of coarse grain composites; (4) development of a preparation technique for fine grain composites; and (5) design of a small LMC and test rig. These five specific areas of endeavor are reported in the following paragraphs.

SMALL DDC-RESISTIVITY CELL STUDIES

Early work with potassium-mercury electrochemical devices has shown the performance characteristics exhibited in Figure 13. These characteristics are typical of any concentration electrochemical device. The potential V_o (Bulk) is caused by the concentration levels of the liquid metal on each side of the electrolyte. The dashed line represents the ideal performance from no-load condition out to a short circuit current, I_{sc} . The internal resistance of this device is given by the first equation, $R_c = \frac{V_o}{I_{sc}}$. Actual data, however, will show a deviation from

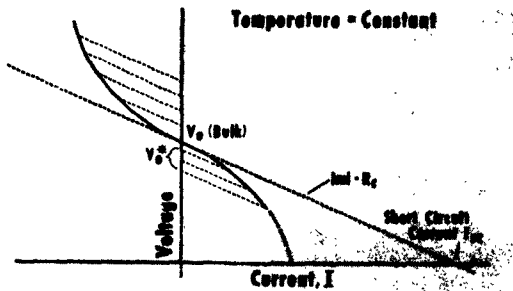
this condition due to a concentration gradient in either or both of the electrode pools. A cell resistance which is calculated from values of terminal voltage, current, and the potential based on the true bulk concentration, V_o (Bulk), will show an increase with higher current loads. If, on the otherhand, care is taken to read the cell potential, V_o^* , at the instant of open circuit switching, the flow dynamics of diffusion and ion exchange are eliminated. Therefore, it is found that the internal resistances remain constant (designated by the slope of dashed lines) and are not a function of current. The technique described in Figure 13 is that used to obtain resistivity values for comparison with those obtained from a-c bridge conductivity measurements.

Consider the relationship

$$RA = \gamma_c t_e = \gamma_e t_e + \gamma'$$

where the left hand term is measured data. This equation states that the cell resistance-area product is a function of the electrolyte resistance, $\gamma_e t_e$, plus a term, γ' , which is associated with the interfaces. Studies were made using various thickness of electrolyte to check this linear equation.

Figure 14 is a schematic of the small cells used for this study. The first five cells did not incorporate separate voltage leads and, therefore, included lead resistance.



Cell Resistance

Ideal $R_c = \frac{V_0}{I_{sc}}$

Data $R_c = \frac{V_0^* - V_c}{I} \neq f(I)$

Resistivity

$\gamma = \frac{R_c A}{l}$

$\gamma = \frac{V_0^* - V_c}{I} \left(\frac{A}{l} \right)$ Constant Geometry

or $\gamma = \frac{V_0^* - V_c}{I} \left(\frac{1}{\frac{l}{A}} \right)$ Specific Performance

ALLISON DIVISION
GENERAL MOTORS CORPORATION

Figure 13. LMC Performance Characteristics

Figure 15 is a plot of the data from the eight cells which were run. Cells 1, 2, 3, 4, and 5 show the effect of an extra resistance in the cell, not associated with the electrolyte. Cells 1A, 3A, and 4A were run with voltage leads and, therefore, show a smaller interfacial resistance, although the value of the electrolyte resistivity must be interpreted as greater than 2 ohm-cm at 300°C.

The systems study requirement of 0.5 ohm-cm² is shown as a dashed line across the bottom for reference. Interfacial resistance, γ' , would place a limit on the development of the cell. A high electrolyte resistivity, without interfacial resistance, can be used since a thickness does exist which will attain systems performance. The conductivity of the pure electrolyte is being measured (on an Allison-funded program) to determine whether the slope given by these three cells is correct.

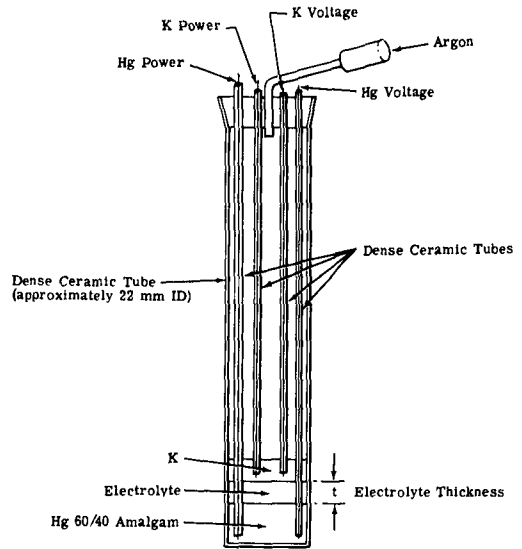


Figure 14. Schematic Diagram of DDC Used in Resistivity Studies

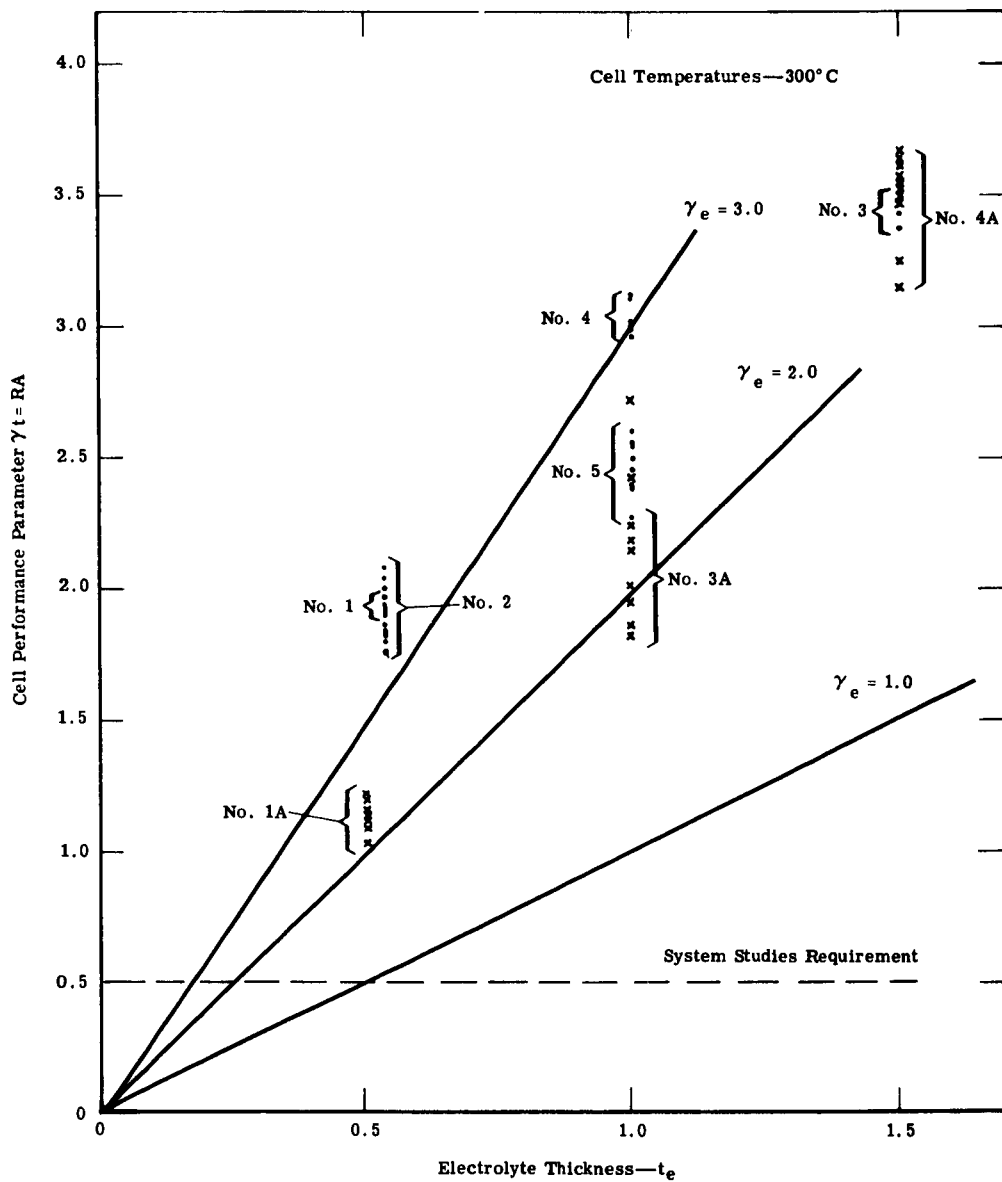


Figure 15. Plot of Data Obtained from Cell Resistivity Studies



CONDUCTIVITY MEASUREMENTS OF COARSE GRAIN COMPOSITES

The conductance measurement is obtained by observing the ohmic impedance of a conductance cell. The resistance measurement is made with an alternating current Wheatstone bridge operating at 10 kc. The polarization at the electrodes of the conductance cell is inversely proportional to the square root of the bridge frequency. Operating the bridge at 10 kc negates the polarization effect, allowing direct measurement of the true ohmic drop of the conductance cell. The ohmic drop of the conductance cell includes lead and contact resistances as well as the desired electrolytic resistance.

The conductance cell for the unconsolidated electrolyte specimens is shown in Figure 3. The cylindrical specimen which is 1.6 cm in diameter \times 1.6 cm high is compressed between two gold electrodes to a new height of 1.55 cm, determined by a ceramic (Al_2O_3) bushing containing the specimen. The furnace is, of course, necessary because of the temperature requirement for an operational fused salt electrolyte. The conductance cell is continuously flooded with argon during the test.

The cell constant is calculated from the geometry of the conductance cell. The cell constant change because of bulging of the specimen is neglected. This is now being subjected to critical review. Thus, the cell constant is defined as

$$K = \frac{L}{A}$$

where

L = compressed height of the specimen (cm)

A = electrode contact area (identical electrodes assumed) (cm^2)

K is expressed in cm^{-1}

The conductance at a specific temperature is obtained simply by dividing the cell constant by the electrolytic resistance.

Analysis of Data

The specimen "pills" are prepared from a bulk mechanical mixture of ternary electrolyte and magnesium oxide powder. The batch is identified by the weight ratio of electrolyte to magnesium oxide and by the average particle size of the MgO powder. An example would be a

6-micron, 35/65 unconsolidated electrolyte. The specimen "pills" require further identification after cold pressing and fusing because of differences in densities. The reference chosen was the maximum density theoretically possible for a given weight ratio batch---that is, the theoretical density describes a system having no interface other than that between the electrolyte and magnesium oxide. Therefore, a specimen is further identified by its percent of theoretical density which is the ratio of its actual density, obtained from its dimensions and weight, and the theoretical density for its weight ratio, times 100. Further identification is obtained by recording the actual dimensions of the specimen.

The conductance of a pure salt follows the Arrhenius relationship for conductance

$$\text{Log } K = A - B/T \quad (1)$$

where

K = conductance ($\Omega \text{ cm}$)⁻¹

A and B = constants

T = absolute temperature

Eutectic mixtures show an increasing deviation from the linear relationship of Equation (1) with decreasing temperature below the melting points of its components, particularly the low melting constituent.⁴ Presenting the data in the form log K versus the reciprocal of the absolute temperature (1/T) is useful in comparing conductance data because of Equation (1). The data obtained for various 6-micron specimens is shown in Figures 16 through 23 and Tables II and III.

Observations and Conclusions

Figures 16, 17, and 18 show plots of the conductivity data for the 31/69, 33/67, and 35/65 weight ratio, 6-micron unconsolidated electrolyte specimens. The conductivities compare favorably with previous 6-micron data reported in an Air Force final report.⁵ The effect of different percent theoretical densities on conductivity is illustrated in Figure 19. The surprising result is that the 31/69, a lower electrolyte ratio, has much greater conductance than

⁴ I. U. K. Delimarskii and B. F. Markov, Electrochemistry of Fused Salts, Sigma Press, 1961, p 28.

⁵ Design and Development of a Liquid Metal Fuel Cell, USAF, ASD Report ASD-TDR-62-1045, December 1962.

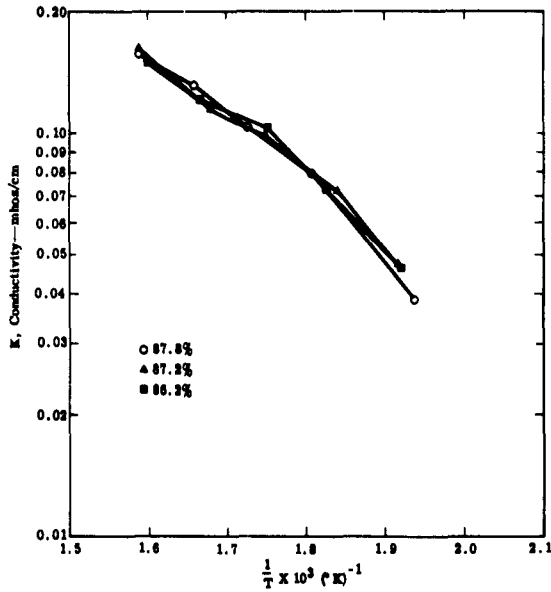


Figure 16. Conductivity of 31/69 Unconsolidated Electrolyte Matrices

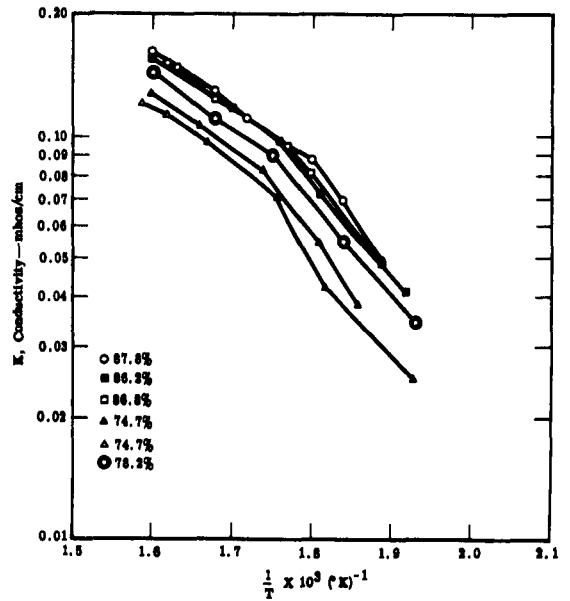


Figure 17. Conductivity of 33/67 Unconsolidated Electrolyte Matrices

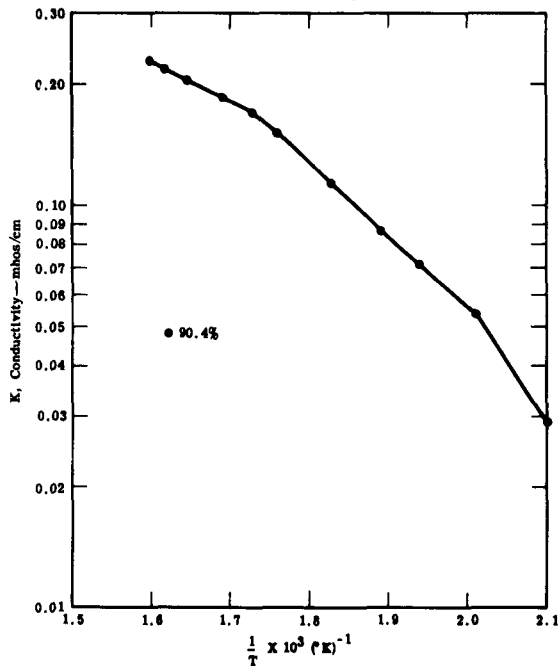


Figure 18. Conductivity of 35/65 Unconsolidated Electrolyte Matrices

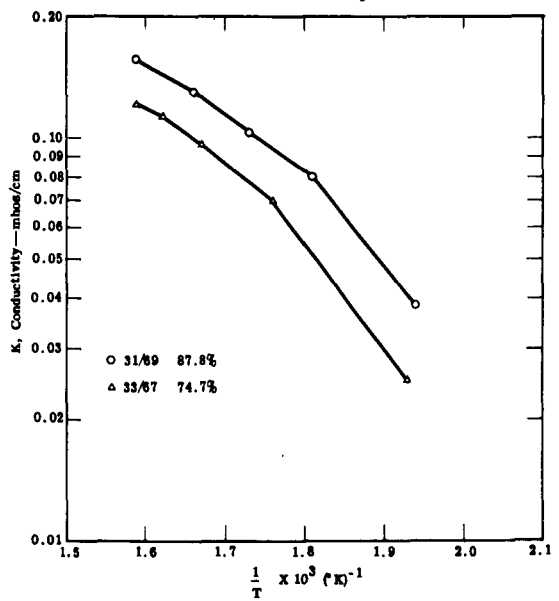


Figure 19. Conductivity of 33/67 and 31/69 Unconsolidated Matrices to Show Density Effect

the 33/67 shown. The contrasting situation occurs in Figure 20, where identical percent theoretical densities are quite similar in conductance. It would seem logical to conclude from Figures 19 and 20 that weight ratio has no effect on conductance. This conclusion would be presumptive, however, since other similar plots of identical percent theoretical densities of different values are unavailable because of the lack of data. In fact, there is strong evidence, based on analysis of the porous media, to discredit this conclusion.

TABLE II
Specimen Identification

<u>Specimen No.</u>	<u>Nominal Weight Ratio</u>	<u>% Theoretical Density</u>	<u>Diameter (in.)</u>	<u>Height (in.)</u>	<u>Test Height (in.)</u>
12	35/65	90.40	0.595	0.740	0.600
13	33/67	87.80	0.606	0.667	0.600
14	33/67	86.00	0.608	0.669	0.600
15	33/67	86.80	0.606	0.658	0.600
16	33/67	74.70	0.616	0.688	0.600
17	33/67	74.70	0.618	0.689	0.600
18	33/67	78.20	0.606	0.690	0.600
19	31/69	87.80	0.613	0.648	0.600
20	31/69	87.20	0.612	0.660	0.600
21	31/69	86.20	0.613	0.654	0.600
22	35/65	92.90	0.603	0.136	0.132
23	35/65	95.80	0.604	0.146	0.085
24	35/65	98.10	0.604	0.132	0.127
25	33/67	86.20	0.621	0.145	0.138
26	33/67	84.60	0.621	0.143	---
27	33/67	85.90	0.621	0.119	0.117
28	34/66	86.90	0.603	0.660	0.600
29	34/66	86.20	0.604	0.614	0.600
30	34/66	86.50	0.602	0.633	0.600
31	34/66	89.40	0.601	0.631	0.600
32	34/66	85.60	0.605	0.636	0.600
33	34/66	85.60	0.606	0.643	0.600
34	34/66	86.50	0.604	0.640	0.600
35	34/66	85.00	0.603	0.727	0.600



TABLE III
Specimen Data

Specimen No.	Temperature (°K)	Resistance (ohms)	Conductivity (mho/cm)	$\frac{1}{T} \times 10^3$ (°K) ⁻¹
12	590	4.65	0.183	1.69
	605	4.20	0.202	1.65
	617	3.89	0.218	1.62
	622	3.77	0.225	1.60
	569	5.76	0.148	1.76
	530	10.06	0.084	1.89
	547	7.63	0.111	1.83
	515	12.22	0.069	1.94
	497	16.20	0.052	2.01
	476	30.10	0.028	2.10
13	624	5.07	0.162	1.60
	595	6.33	0.130	1.68
	556	9.44	0.087	1.80
	580	7.40	0.111	1.72
	544	11.81	0.069	1.84
	528	16.74	0.049	1.89
	503	41.00	0.020	1.99
14	625	5.11	0.160	1.60
	588	6.94	0.117	1.70
	568	8.37	0.097	1.76
	550	11.33	0.072	1.81
	522	19.63	0.041	1.92
	499	75.00	0.011	2.00
15	595	6.55	0.125	1.68
	615	5.57	0.147	1.63
	619	5.43	0.151	1.62

TABLE III (cont)

Specimen No.	Temperature (°K)	Resistance (ohms)	Conductivity (mho/cm)	$\frac{1}{T} \times 10^3$ (°K) ⁻¹
15 (cont)	566	8.67	0.094	1.77
	573	8.06	0.102	1.75
	555	10.17	0.081	1.80
	530	17.20	0.048	1.89
16	625	6.19	0.128	1.60
	603	7.41	0.107	1.66
	576	9.62	0.082	1.74
	553	14.74	0.040	1.81
	538	24.90	0.038	1.86
17	619	6.96	0.114	1.62
	627	6.50	0.122	1.59
	598	8.25	0.096	1.67
	569	11.23	0.070	1.76
	548	18.90	0.042	1.82
	518	31.75	0.025	1.93
	536	20.54	0.038	1.87
18	626	5.70	0.144	1.60
	594	7.45	0.110	1.68
	572	9.15	0.090	1.75
	544	15.19	0.054	1.84
	519	23.94	0.034	1.93
19	629	5.08	0.157	1.59
	604	6.15	0.130	1.66
	579	7.65	0.104	1.73
	553	9.99	0.080	1.81
	515	20.54	0.039	1.94



TABLE III (cont)

Specimen No.	Temperature (°K)	Resistance (ohms)	Conductivity (mho/cm)	$\frac{1}{T} \times 10^3$ (°K) ⁻¹
20	629	5.10	0.159	1.59
	596	6.48	0.123	1.68
	570	8.17	0.098	1.75
	544	11.10	0.072	1.84
	520	16.87	0.047	1.92
21	622	5.32	0.150	1.61
	596	6.52	0.122	1.68
	572	8.16	0.098	1.75
	547	10.97	0.073	1.83
	521	17.32	0.046	1.92
22	636	1.02	0.175	1.57
	609	1.25	0.143	1.64
	581	1.56	0.115	1.72
	555	2.26	0.079	1.80
	527	3.74	0.049	1.90
23	633	0.45	0.140	1.56
	598	0.55	0.114	1.67
	570	0.70	0.090	1.75
	536	1.11	0.057	1.86
	509	1.80	0.035	1.96
24	613	0.88	0.162	1.63
	595	1.00	0.143	1.68
	561	1.34	0.107	1.78
	531	2.30	0.062	1.88
	516	3.26	0.044	1.93

TABLE III (cont)

Specimen No.	Temperature (°K)	Resistance (ohms)	Conductivity (mho/cm)	$\frac{1}{T} \times 10^3$ (°K) ⁻¹
25	630	1.43	0.126	1.58
	609	1.70	0.106	1.64
	587	2.20	0.082	1.70
	546	5.96	0.030	1.83
26	618	0.66	0.127	1.61
	613	0.70	0.120	1.62
	585	0.90	0.093	1.70
	556	1.21	0.069	1.79
	522	2.30	0.036	1.91
27	619	1.20	0.122	1.62
	605	1.42	0.104	1.65
	559	2.51	0.058	1.79
	524	5.55	0.026	1.91
28	635	4.60	0.195	1.57
	611	5.55	0.164	1.63
	592	6.53	0.139	1.68
	573	7.74	0.117	1.74
	551	10.36	0.091	1.81
	529	15.18	0.060	1.92
29	647	4.46	0.189	1.54
	628	5.16	0.163	1.59
	604	6.20	0.136	1.65
	568	8.67	0.097	1.74
	532	14.50	0.058	1.87



TABLE III (cont)

Specimen No.	Temperature (°K)	Resistance (ohms)	Conductivity (mho/cm)	$\frac{1}{T} \times 10^3$ (°K) ⁻¹
30	654	4.20	0.208	1.52
	628	5.16	0.170	1.59
	600	6.26	0.140	1.66
	573	8.04	0.109	1.79
	548	11.43	0.076	1.82
	524	17.84	0.049	1.90
31	642	4.50	0.195	1.58
	623	5.20	0.168	1.60
	591	6.84	0.128	1.69
	568	8.50	0.103	1.76
	529	15.68	0.056	1.85
32	652	4.34	0.201	1.53
	623	5.24	0.166	1.60
	592	6.67	0.130	1.68
	565	8.67	0.100	1.76
	534	14.30	0.060	1.87
33	652	5.17	0.170	1.53
	618	6.38	0.138	1.61
	594	7.80	0.112	1.68
	563	10.44	0.084	1.77
	534	16.67	0.052	1.87
34	647	4.83	0.182	1.54
	623	5.76	0.153	1.60
	592	7.47	0.118	1.68
	560	10.65	0.083	1.78
	531	17.30	0.051	1.88

TABLE III (cont)

Specimen No.	Temperature (°K)	Resistance (ohms)	Conductivity (mho/cm)	$\frac{1}{T} \times 10^3$ (°K) ⁻¹
35	647	8.40	0.118	1.54
	621	10.25	0.097	1.61
	587	13.70	0.073	1.70

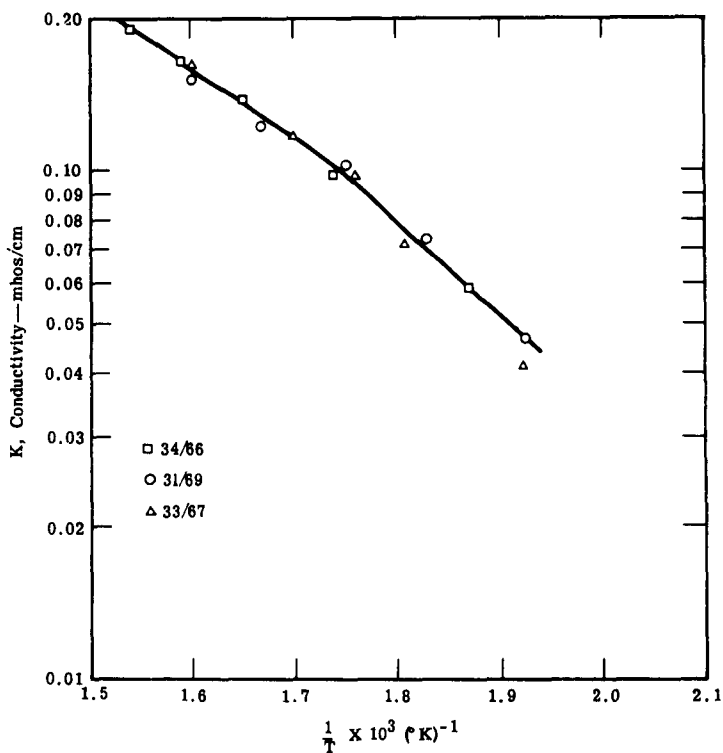


Figure 20. Conductivity of 31/69, 33/67, and 34/66 Unconsolidated Matrices With 86.2% Theoretical Density



Figures 21 and 22 show the conductivity data for the 34/66, 6-micron specimens. This batch had a different weight ratio because of difficulty in correlating strength measurements between the 33/67 and 35/65 batches. Preliminary results of strength test procedures on this batch have not been completely satisfactory. Conductance data are presented, however, because of the correlations shown in Figures 19 and 20.

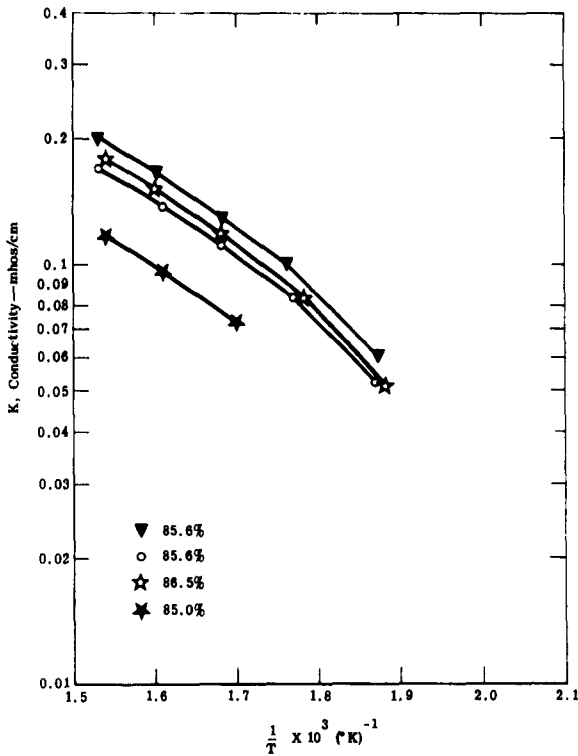


Figure 21. Conductivity of 34/66 Unconsolidated Electrolyte Matrices

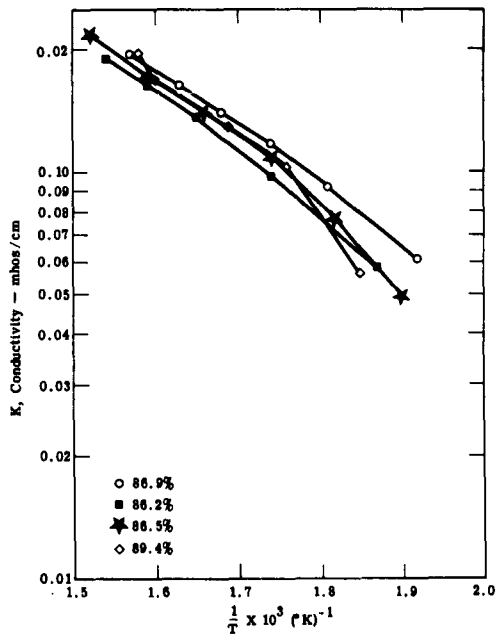


Figure 22. Conductivity of 34/66 Unconsolidated Electrolyte Matrices

Interest in contact resistance in the measurement of the ohmic impedance of the conductance cell led to the plot of conductance of 0.3-cm thick unconsolidated specimens shown in Figure 23. The plan was to plot resistivity versus thickness and observe the intercept when the thickness was extrapolated to zero. Difficulty in measuring the low resistance of 0.3-cm thick by 1.6-cm dia specimens is evidenced by the scattering of the data. The most exacting conclusion that can be drawn from these data as to contact resistance is that there appeared to be a statistical chance of having appreciable contact resistance.

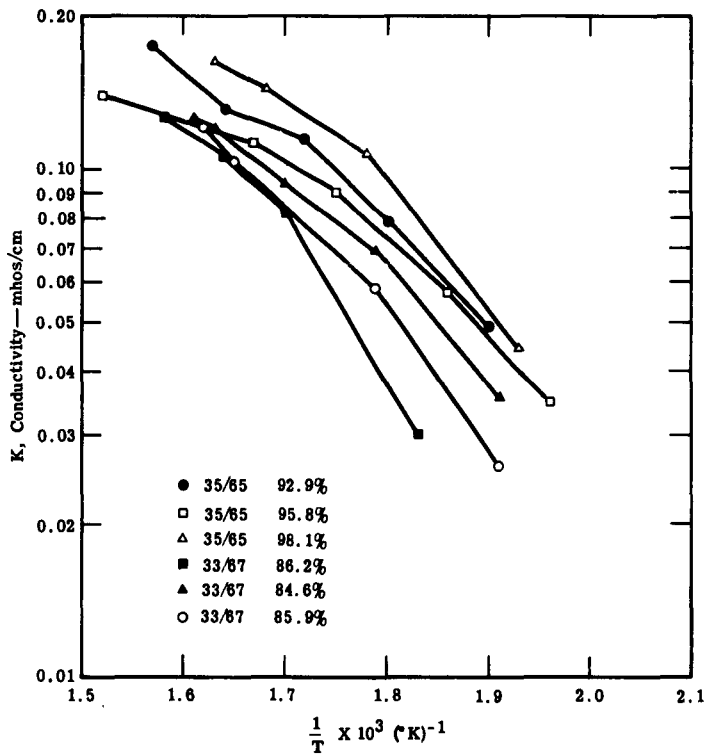


Figure 23. Conductivity of 0.3-cm Unconsolidated Electrolyte Matrices



Comparison of specimens according to change in conductance with weight ratio was originally intended to show the effect of electrolyte content on conductance. However, observation of the data shows that percent theoretical density, which was varied by varying pressing pressures, had a pronounced effect on conductivity. This is understandable from the definition of theoretical density. The original approach to the problem involved striving for a maximum percent theoretical density using necessary pressing pressures. This requirement indicated that the percent theoretical density would not vary significantly, thus reducing its effect on conductance.

As the mechanism of the capillary forces involved became further understood, it became necessary to study more significant variations in theoretical density to facilitate optimization of the strength properties. The percent theoretical density is dependent on the electrolyte content and the porous medium geometry. Thus, in the present form, the data are not truly parametric, and it is necessary to separate the electrolyte saturation effect on conductance from the porous medium geometry effect. The method for reducing the data to this form has now been finalized and involves simple geometrical relationships and certain empirical relationships drawn from literature on porous media. The previous data will be transformed to the new parameters with the aid of digital computation.

The need for the more comprehensive analysis of the data has created a possible problem with the measurement technique. The error in obtaining measurements could possibly obscure the effect of subdivision of the data into their more pertinent form. The necessary sensitivity will be approximated from anticipated results—i. e., by anticipating the effect of small changes in saturation and pore geometry. An error analysis is being conducted to define the accuracy of the measurement technique, and methods of reducing the error (if necessary) are being considered. Comparing the necessary sensitivity with the results of the error analysis will bring the conductivity study to a possible branch point, necessitating a parallel program of measurement technique improvement while maintaining contractual requirements for conductance measurements. This will be described in greater detail in the second quarterly report.

COMPRESSIVE STRENGTH MEASUREMENTS OF COARSE GRAIN COMPOSITES

Compressive strength measurements are taken at cell operating temperature and within an inert atmosphere. Figure 7 is a schematic representation of this test.

Preliminary analysis of data shows that the ball penetration strength tests are approximately as shown in Table IV.

TABLE IV
Ball Penetration Strength Test Results

<u>Percent Electrolyte</u>	<u>Percent Theoretical Density</u>	<u>Strength (psi)</u>
31	86	22
33	75	10
33	86	10-20
35	75	5
35	86	1

These data indicate a transition between the 33 and 35% composites—i. e., a change in the trend of strength variation to density for a given percent electrolyte composite.

Further work with 34% composites to fill in the data was not accomplished during this period.

Another type of test was initiated to measure deformation characteristics of the composite. Unlike the ball penetration test, a load is applied over the entire area of a specimen between two flat plates. Deformation, in terms of the reduction in thickness, is recorded at the point where rupture of the material around the circumference is observed. Preliminary data from this test are given in Table V.

TABLE V
Deformation Test Data

<u>Percent Electrolyte</u>	<u>Percent Theoretical Density</u>	<u>Approximate Deformation to Failure (%)</u>
31	---	20
33	---	30
35	low	40
35	high	50



This indicates the increase in plasticity or flowability as electrolyte saturation is increased by either (1) an addition of electrolyte or (2) a greater densification for a given percent electrolyte composite.

DEVELOPMENT OF A PREPARATION TECHNIQUE FOR FINE GRAIN COMPOSITES

The fine grain composite was successfully prepared by using a new dry mixing process. An electron micrograph showed the particle size of the fine MgO powder to be in the range 0.033 to 0.053 micron. This material is prepared in the following steps.

Dry Process for Fabrication of Fine Powder

1. MgO powder is dried at 1600°F in air for 20 hr
2. The KBr, KI, and KOH are fused in a 700°F vacuum furnace until a pressure of two microns of mercury is reached
3. The fused electrolyte is taken out hot and poured down the sides of a stainless steel beaker—this enables the electrolyte to cool into thin layers
4. The layers are broken into small pieces and sent through a grinder
5. The ground pieces are then ball milled and sieved
6. The proper amount of MgO and electrolyte is weighed out as established by batch size and electrolyte/MgO ratio
7. This weighed mixture is milled for one hour
8. The mixture is then pressed into a 4-in. dia briquet and vacuum baked until a vacuum of two microns of mercury is reached
9. The briquet is taken out of the furnace hot, broken into small granules, and put into the ball mill
10. Material is then handled in the same manner as the coarse grain as far as forming, pressing, and baking the specimens is concerned.

A 55% electrolyte composite was successfully prepared, but no further testing was accomplished during this period.

DESIGN OF A SMALL LMC AND TEST RIG

The final test of a composite matrix is to be made in an actual liquid metal cell. All preliminary work will support selection of the composite best suited for cell operation. One further property of the matrix is that condition which allows a good seal to form between the matrix and the surrounding material.

It has been proposed that the composite electrolyte matrix have a certain amount of surface liquid which will form a seal against metal or ceramic. It is further thought that a composite of this type will display a plastic creep so that a long term stress will deform the matrix. With these ideas, the design shown in Figure 24 was fabricated in the shop.

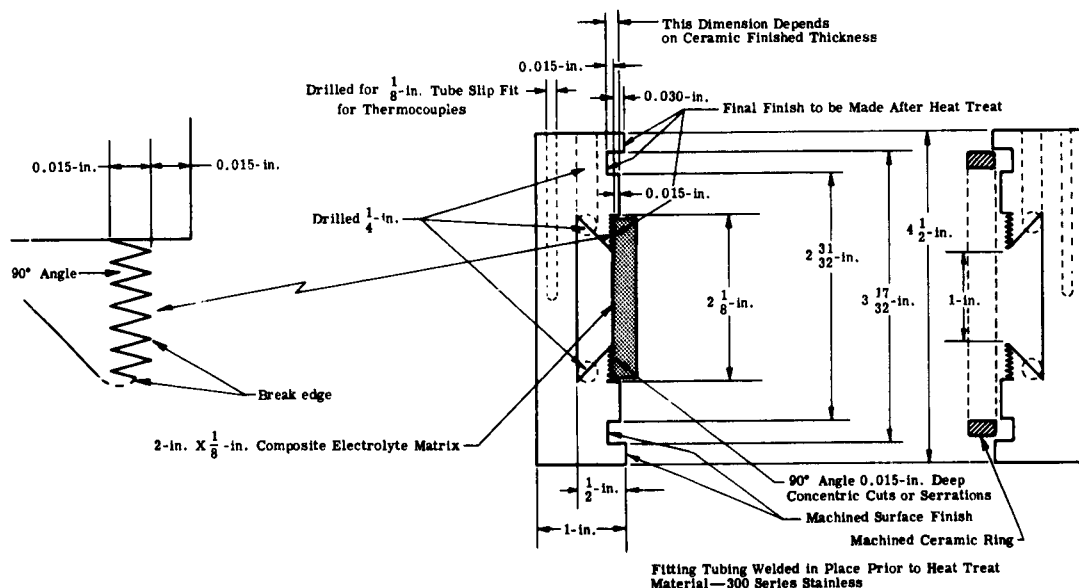


Figure 24. Test Equipment for First Small Unit



The salient features of this unit are as follows:

1. The electrode metal chambers have been designed so that rework of the machined angle will increase the cell area and decrease the seal area.
2. The serrated seal area has been designed to attain a 0.015-in. bite into the composite matrix. Early studies showed no gas leaks under a 5-psi differential gas pressure.
3. A machined ceramic ring serves as a mechanical stop to relieve deformation stress after the seal has been established.
4. A high temperature silicone rubber is incorporated at the outside of the mating surfaces to keep the cell inerted from ambient air.
5. Provision can be made to incorporate a supporting member (screen or perforated plate) to oppose differential pressure across the matrix.

The small cell unit test setup is shown in Figure 25. The cell assembly and all auxiliary components are made an integral part of a small furnace. The procedure for loading the electrolyte matrix is as follows:

1. The cell halves are placed in an inert glove box along with the matrix, ceramic ring, and silicone rubber seal.
2. The unit is assembled in the horizontal position with the oversized rubber taking the top-half load.
3. The assembly is removed from the dry box, with all lines sealed, and placed into the furnace. The furnace is positioned on the left side at this time.
4. After the clamp is applied and all line connections are made, the furnace is brought up to temperature while the cell is slowly closed. This ensures that the matrix is not damaged prior to becoming a paste.
5. The entire test rig is rotated to the position shown in Figures 25 and 26.

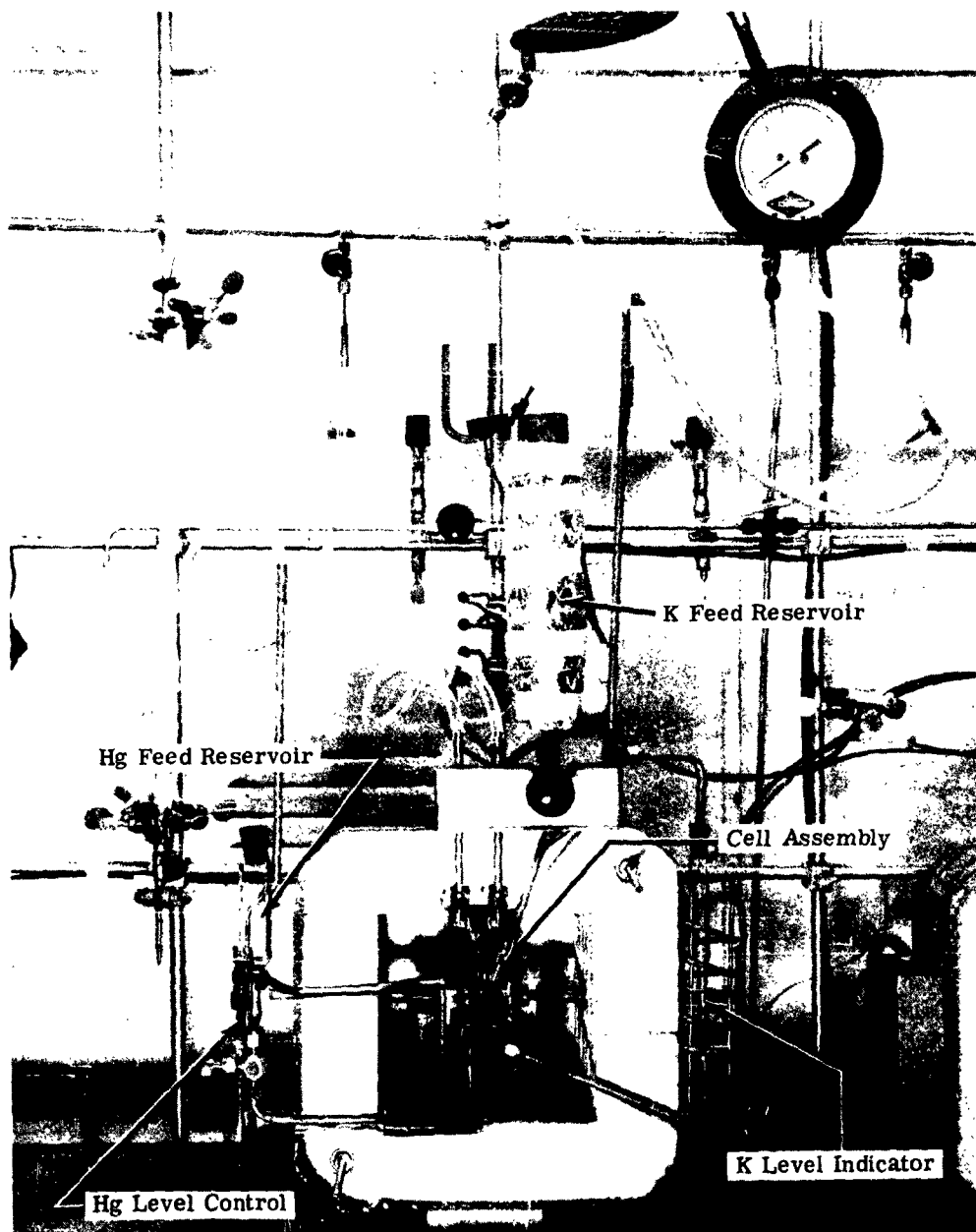


Figure 25. Small Cell Test Setup

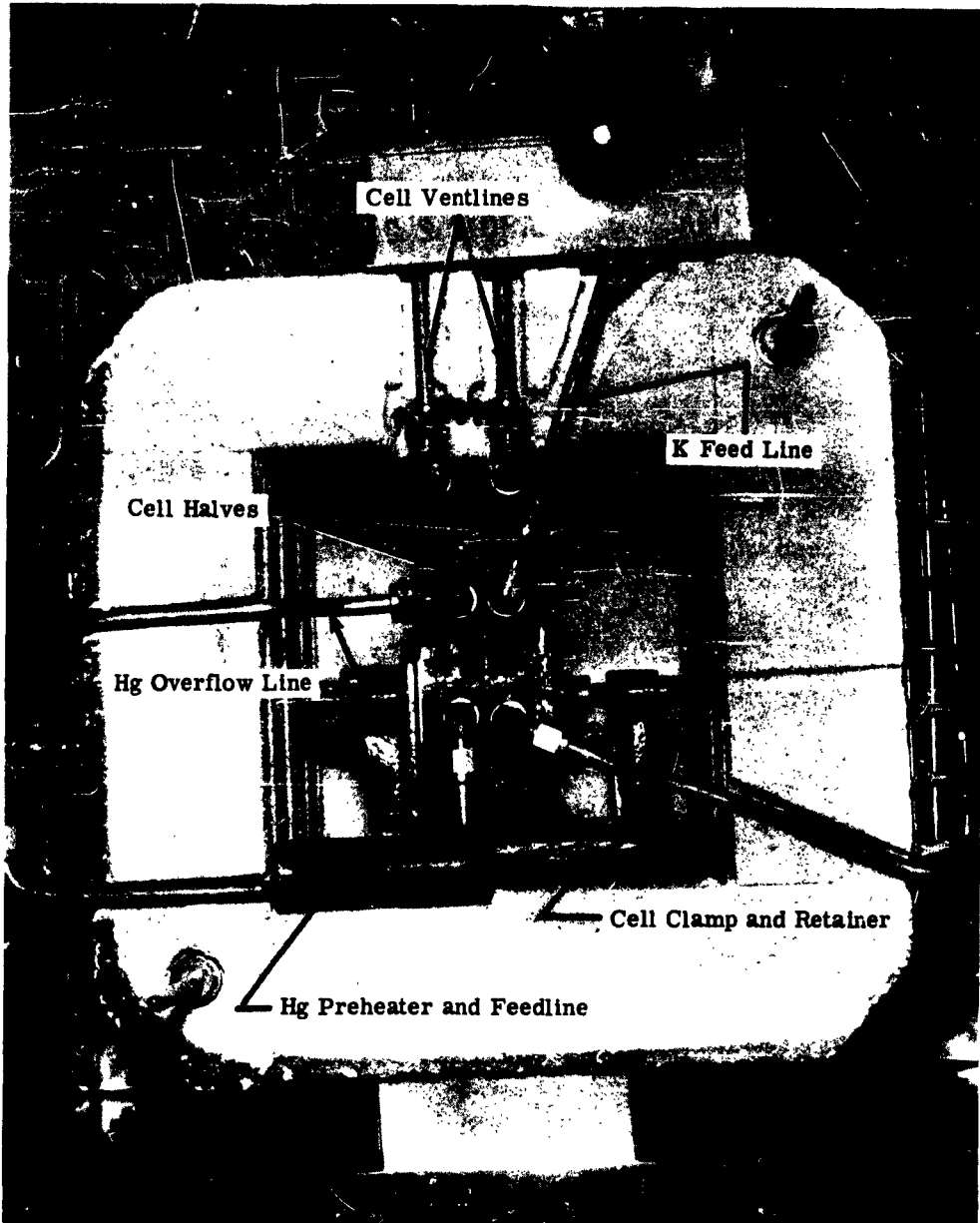


Figure 26. Small Cell Assembly

The liquid metal loading procedure is as follows:

1. Potassium is introduced to the K feed reservoir and later let down to the cell by the valve shown. The level is noted in the K-level indicator at right.
2. Mercury is loaded to the Hg feed reservoir and then let down to the Hg preheater at a rate sufficient to bring material up to near cell temperature.
3. The Hg level is controlled by the overflow line to the lower reservoir. This reservoir will also serve to receive the amalgam formed from electrochemical operation.

One cell test was performed. In way of a preview to future progress and, specifically, to illustrate the cell halves, Figure 27 is presented. Analysis of the test results are not complete, but it can be stated that this cell gave satisfactory performance for 38 minutes.

Figure 27 shows in detail the seal region serrations, silicone rubber ceramic ring, and a composite matrix in position. The K metal shown is thought to have deposited in this cavity during the shutdown procedure and is not the cause of failure. More about this work will be reported in subsequent status reports.

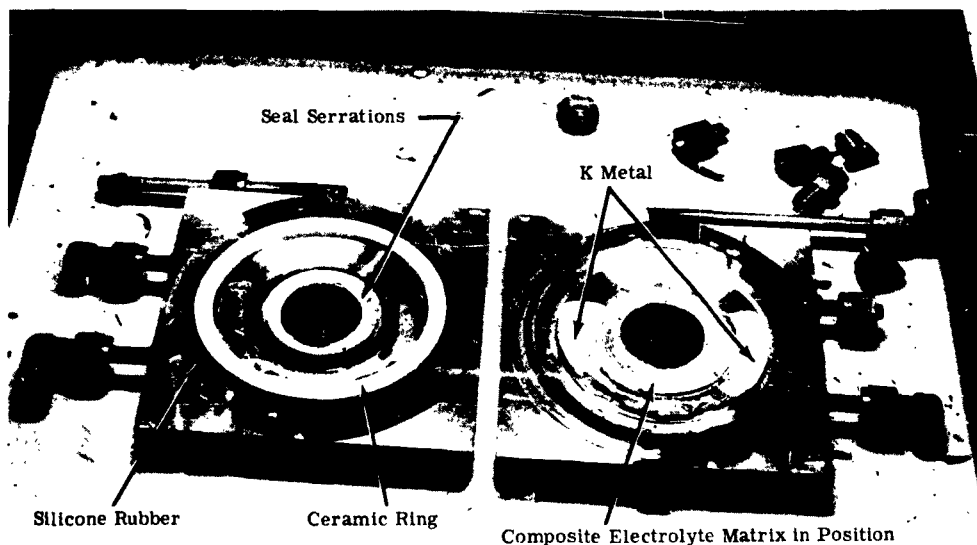


Figure 27. Post Analysis of Small Cell

Allison Division, General Motors Corporation
 FIRST QUARTERLY TECHNICAL PROGRESS REPORT ON
 RESEARCH AND DEVELOPMENT OF AN ADVANCED
 LABORATORY LIQUID METAL REGENERATIVE FUEL
 CELL FOR THE PERIOD 1 MARCH — 18 MAY 1963. 28
 May 1963. 100 p. incl. illus. (Project No. 8173, Task No.
 817303) (Allison EDR 3344) (Contract AF33(657)-11032)
 Unclassified Report

Work is under way to design a laboratory-type cell for
 operation with a matrix. Tests are in progress to deter-
 mine matrix compatibility with electrolyte; optimization of
 mechanical and electrical properties of the matrix are
 progressing. A successful 96-hour seal was produced,
 although insulators were cracked and electrolyte seepage

1. Liquid metal fuel cells
 2. Potassium-mercury fuel
 cells
 I. AFSC Project 8173, Task
 817303
 II. Contract AF33(657)-11032
 H. R. Karas and J. D.
 Mangus

Allison Division, General Motors Corporation
 FIRST QUARTERLY TECHNICAL PROGRESS REPORT ON
 RESEARCH AND DEVELOPMENT OF AN ADVANCED
 LABORATORY LIQUID METAL REGENERATIVE FUEL
 CELL FOR THE PERIOD 1 MARCH — 18 MAY 1963. 28
 May 1963. 100 p. incl. illus. (Project No. 8173, Task No.
 817303) (Allison EDR 3344) (Contract AF33(657)-11032)
 Unclassified Report

Work is under way to design a laboratory-type cell for
 operation with a matrix. Tests are in progress to deter-
 mine matrix compatibility with electrolyte; optimization of
 mechanical and electrical properties of the matrix are
 progressing. A successful 96-hour seal was produced,
 although insulators were cracked and electrolyte seepage

1. Liquid metal fuel cells
 2. Potassium-mercury fuel
 cells
 I. AFSC Project 8173, Task
 817303
 II. Contract AF33(657)-11032
 H. R. Karas and J. D.
 Mangus

Allison Division, General Motors Corporation
 FIRST QUARTERLY TECHNICAL PROGRESS REPORT ON
 RESEARCH AND DEVELOPMENT OF AN ADVANCED
 LABORATORY LIQUID METAL REGENERATIVE FUEL
 CELL FOR THE PERIOD 1 MARCH — 18 MAY 1963. 28
 May 1963. 100 p. incl. illus. (Project No. 8173, Task No.
 817303) (Allison EDR 3344) (Contract AF33(657)-11032)
 Unclassified Report

Work is under way to design a laboratory-type cell for
 operation with a matrix. Tests are in progress to deter-
 mine matrix compatibility with electrolyte; optimization of
 mechanical and electrical properties of the matrix are
 progressing. A successful 96-hour seal was produced,
 although insulators were cracked and electrolyte seepage

1. Liquid metal fuel cells
 2. Potassium-mercury fuel
 cells
 I. AFSC Project 8173, Task
 817303
 II. Contract AF33(657)-11032
 H. R. Karas and J. D.
 Mangus

Allison Division, General Motors Corporation
 FIRST QUARTERLY TECHNICAL PROGRESS REPORT ON
 RESEARCH AND DEVELOPMENT OF AN ADVANCED
 LABORATORY LIQUID METAL REGENERATIVE FUEL
 CELL FOR THE PERIOD 1 MARCH — 18 MAY 1963. 28
 May 1963. 100 p. incl. illus. (Project No. 8173, Task No.
 817303) (Allison EDR 3344) (Contract AF33(657)-11032)
 Unclassified Report

Work is under way to design a laboratory-type cell for
 operation with a matrix. Tests are in progress to deter-
 mine matrix compatibility with electrolyte; optimization of
 mechanical and electrical properties of the matrix are
 progressing. A successful 96-hour seal was produced,
 although insulators were cracked and electrolyte seepage

1. Liquid metal fuel cells
 2. Potassium-mercury fuel
 cells
 I. AFSC Project 8173, Task
 817303
 II. Contract AF33(657)-11032
 H. R. Karas and J. D.
 Mangus

occurred. A preliminary check of electrochemical properties yielded encouraging results, predicting performance in the 50- to 100-watt/ft² range.



occurred. A preliminary check of electrochemical properties yielded encouraging results, predicting performance in the 50- to 100-watt/ft² range.



occurred. A preliminary check of electrochemical properties yielded encouraging results, predicting performance in the 50- to 100-watt/ft² range.



occurred. A preliminary check of electrochemical properties yielded encouraging results, predicting performance in the 50- to 100-watt/ft² range.

